Hybrid RANS-LES Turbulence Models for FSI Application

Thesis Report

Manini Mittal

TU Delft

Hybrid RANS-LES Turbulence Models for FSI Application

THESIS REPORT

by

Manini Mittal

to obtain the degree of Master of Science
at the Delft University of Technology
to be defended publicly on August 15, 2024 at 10:30

Thesis committee:

Chair:	Dr. Ir. M.I. Gerritsma
Supervisors:	Dr. Alexander van Zuijlen
	Dr. E.M.A Frederix
	Kevin Zwijsen
External examiner:	Dr Jurij Sodja
Place:	Faculty of Aerospace Engineering, Delft
Project Duration:	December, 2023 - August, 2024
Student number:	5724031

An electronic version of this thesis is available at `http://repository.tudelft.nl/`.

Faculty of Aerospace Engineering · Delft University of Technology

Abstract

This thesis investigates the application of hybrid turbulence models for fluid-structure interaction (FSI) to evaluate phenomena such as vortex-induced vibration (VIV) in tube rods within nuclear reactors. The study aimed to identify and validate the most effective hybrid modeling approaches to improve the accuracy and efficiency of FSI simulations in this critical application. Hybrid RANS-LES models aim to use RANS modeling in regions where the flow is relatively steady and well-predicted by the RANS approach, while switching to LES in regions where turbulence is more dynamic and complex. This switch can either be very explicit and segregate the domain into RANS and LES zones or it can be a subtle modification in the transport equations using either RANS or LES as baseline.

The research began with a detailed literature review, leading to the selection of four promising hybrid turbulence models: Improved Delayed Detached Eddy Simulation (IDDES), Scale Adaptive Simulation (SAS), Partially Averaged Navier–Stokes (PANS), and Struct Epsilon (SE). These models were implemented and tested through numerical case setups to validate their performance against established reference data for crossflow over a circular cylinder at a Reynolds number (Re) of 3900.

A comparative analysis was conducted to assess the performance of the selected models. Based on this analysis, two models were shortlisted for further testing. These models were subjected to additional validation on a rigid body motion case to ensure their reliability and accuracy in FSI applications.

In this validation, the models were used to simulate flow over an elastically mounted rigid cylinder in crossflow to evaluate the frequency and displacement of its oscillation. They were tested at different velocities to determine the amplitude and frequency response. The SE model was observed to be more robust and efficient than IDDES.

In conclusion, the research provides validation, selection and comparison of different hybrid turbulence models for FSI applications. Recommendations for future research are also provided to further refine these modeling approaches.

Acknowledgement

I want to express my sincere gratitude to several individuals who have supported and guided me throughout this endeavor.

First and foremost, I extend my heartfelt thanks to Professor Alexander van Zuijlen for this opportunity and his invaluable guidance and support. His expertise and encouragement have been instrumental in the completion of this project.

I deeply appreciate my supervisors, Edo Fredrix and Kevin Zwijsen, whose insights and advice were crucial in navigating the challenges I encountered. Their mentorship has been indispensable.

I am profoundly grateful to my family, my parents, and grandparents for their unconditional love and encouragement. Your unwavering support has been my foundation.

I also acknowledge my friends Amish, Avani, Dnyandevi, Gandharv, Riya and Jagdishwaran for their companionship and support throughout this journey, especially when things got difficult to manage.

Thank you all for your encouragement and support.

Contents

Nomenclature

List of Abbreviations

CFD Computational Fluid Dynamics

DDES Delayed Detached Eddy Simulation

DES Detached Eddy Simulation

DOF Degree of freedom

EVM Eddy Viscosity Models

FEM Finite Element Method

FIV Flow Induced Vibration

FSI Fluid Structure Interaction

FSM Flow Simulation Methodology

IDDES Improved Delayed Detached Eddy Simulation

IPCC Intergovermental Panel On Climate Change

LES Large Eddy Simulation

LLM Long Layer Mismatch

NLEVM Non Linear Eddy Viscosity Model

PANS Partial Averaged Navier Stroke

PISO Pressure Implicit with Splitting Of Operators

PWR Pressurized Water Reactor

RANS Reynolds Averaged Navier Strokes

RMSE Root Mean Square Error

RSM Reynolds Stress Models

SAS Scale Adaptive Simulation

SE Struct Epsilon

SGS Sub Grid Scale

TIV Turbulence Induced Vibration

URANS Unsteady Reynolds Averaged Navier Strokes

List of Symbols

δ First layer thickness

ω specific dissipation rate

ρ Fluid density

τ Reynolds Stress Tensor

θ Angle correspondingCircumferential position on cylinder

ε rate of dissipation of turbulent kinetic energy

A^* Non Dimensionalised Displacement

f_ϵ Dissipation rate ratio

f_ω Kinetic energy ratio

f_ω specific dissipation rate ratio

f_k Kinetic energy ratio

k Turbulent kinetic energy

t	Time-step	u'	Velocity Fluctuation
u	Forward velocity component	U^*	Non Dimensionalised Velocity

List of Figures

List of Tables

1

Introduction

As the global population continues to increase, so does the demand for energy. Conventional energy sources are being utilized in large amounts, making humans completely dependent on them and, the recent energy crisis became a key example of the consequences of this dependency. The global energy crisis of 2022 was not specifically a clean energy crisis, but it highlighted the critical need for rapid, people-centered, and orderly transitions. In the time of crisis, governments incurred emergency support costs of USD 900 billion to shield consumers from fluctuating fuel prices. To reduce such expenditures in the future, it is essential to deploy cost-effective, clean technologies at scale, particularly in poorer households, communities, and countries that face challenges in financing the necessary upfront investments [1].

From an environmental point of view, the Intergovernmental Panel on Climate Change (IPCC) has issued a warning about the global temperature rise of 1.5^{o}C and has recommended research for alternative energy sources. The IPCC predicts that the share of primary energy from renewable increases while coal usage decreases across pathways, limiting warming to 1.5^{o}C with no or limited overshoot [2].

It is to be noted that an average egg-sized uranium fuel is equivalent to 88 tonnes of coal in terms of energy production [1]. In addition to emitting CO2, a coal-burning plant discharges substantial amounts of other pollutants, including radioactive substances. In contrast, nuclear energy does not generate greenhouse gases and, if operated safely, does not pollute the environment.Additionally, while the waste from fossil fuel is generally large in volume and directly dumped into the environment, nuclear waste is much easier to contain and smaller in volume. These benefits are particularly compelling in a world where the threat of global warming is imminent and alarming [3].

Nuclear Energy is, therefore one of the promising alternatives for this transition to a cleaner energy-based world and there are many initiatives being led towards the same.[4] For example, France implemented a program to rapidly get 80% of its energy from nuclear power in about 25 years. However, this project is currently stunted and lags by 10 years on its original timeline mainly because of public perception [5].

Contrary to public perception, studies present that the actual probability of fatality due to nuclear energy is much lower compared to conventional fuels like coal or oil. It's even far less than the

[1] https://www.iaea.org/newscenter/news/infographics-nuclear-energy-compared

possibility of fatality due to other green sources like wind or hydro-energy [6, 7]. However, the statistics also show that the damages due to nuclear incidents are far more expensive than those from other sources. Considering the situation, safety measures are critically followed around a nuclear reactor with a lot of consideration being given to safety at every step of development and operation.

One of the main safety concerns is the fatigue caused by turbulence-induced vibrations. Flow-induced vibration (FIV) is the major cause of fatigue problems in reactor internals. Low-cycle fatigue is caused by large-amplitude vibrations which is preventable by detaining the system's natural frequency from the dominant flow-generated excitation frequency. This phenomenon is particularly relevant for Pressurized water reactors (PWR) as they incorporate fuel tubes that are sensitive to the FIV [8].

The Section Section 1.1 provides a brief background on nuclear reactors followed by Section 1.2 providing an overview of FIV associated with nuclear reactors.

1.1. Pressurised Water Reactors

Pressurised Water Reactors (PWR) are the most prominent and popular reactor type among the many reactors designed during the past century [9]. There are approximately 300 PWR installed in the world and more are under the installation process accounting for about 67 % of all reactors (Fernandez-Arias ´ et al., 2020). A PWR operates with water as coolant at a pressure of about 150 Bar and a temperature going upto $320°C$ [10]. The heat generated by the nuclear fuel in the reactor is transferred through heat exchanger first to the primary circuit followed by to the coolant unit in the secondary circuit [11]. A simple PWR layout is shown in Figure 1.1.

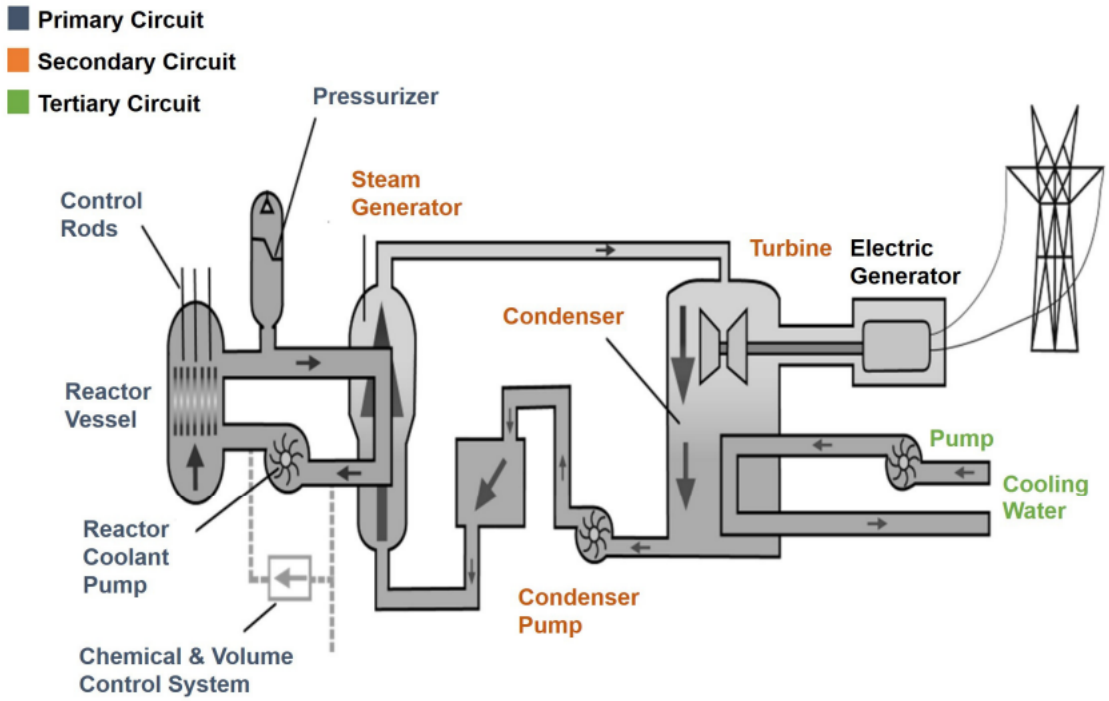

Figure 1.1: PWR Layout and main circuit

Conventionally, fuel rods contain uranium dioxide (UO_2) fuel pellets arranged in a regular pattern in the reactor core, for which Zircaloy-4 is used as the fuel cladding material [12]. A particularly important topic in the field of nuclear safety is the behaviour of these fuel rods. These fuel rods are submerged in a coolant which flows axially along the fuel rods. While the axial flow accelerates the cooling process of the rods, it also leads to Flow Induced Vibrations (FIV) in the fuel rods. These vibrations are caused due to the pressure fluctuations in the flow. This phenomenon plays a critical role in nuclear safety, as it can cause structural effects such as fatigue problems and fretting wear [13, 14, 15]. The phenomenon has been studied since the early development of nuclear reactors in the 1950s, and is one of the major safety concerns. However, in this study instead of tackling the axial flow issues, a simpler case of tube in crossflow is analysed for evaluation of Vortex Induced Vibration.The phenomenon is further discussed in Section 1.2.

1.2. Flow Induced Vibration

Flow-Induced Vibration (FIV) is a comprehensive term that includes vibrations resulting from the interaction between a structure and the surrounding fluid flow. In contrast, **Turbulence-Induced Vibration (TIV)** specifically pertains to vibrations caused by the turbulent characteristics of the fluid flow. When considering a cylinder in crossflow, turbulence in the fluid can interact with the cylinder, resulting in vibrations. Although both phenomena can be conceptually differentiated, in the context of Fluid-Structure Interaction (FSI) simulations for a cylinder in crossflow, the emphasis is generally on the holistic understanding of the intricate interactions between the fluid and the structure that culminate in vibrations [16].

Flow-induced vibrations of elastic bodies can appear in a variety of ways, with transverse vibrations of a bluff body section in constant incident flow drawing attention in a range of engineering applications.

Vortex-induced vibration , a type of flow induced vibration occurs when alternating vortices are shed from the surface of a bluff body (a body with a non-streamlined shape, such as a cylinder) as fluid flows past it. These vortices create oscillating lift forces perpendicular to the flow direction, which can induce periodic vibrations in the structure. VIV is highly dependent on the flow velocity, the dimensions of the structure, and the fluid properties.

The bluff body section indicates a flow separation with a broad wake within two shear layers; a steady incident flow dictates no organised transient or oscillatory characteristics to be present in the flow. However, vortex shedding can lead to a mutual coupling and flow separation within the particular time window. As vortices shed from either side of the structure, alternating forces are created at certain frequencies in the streamwise and transverse directions. The vibrations created due to this alternating force are referred to as flow-induced vibrations. To theoretically address flow-induced vibrations in tubes, Lever and Weaver [17] pioneered the development of a one-dimensional analytical model based on mass and momentum conservation equations. Schroder and Gelbe [18] subsequently extended this work by creating two- and three-dimensional simulation models for a complete tube row and a tube bundle. These studies have considerably advanced the simulation of flow-induced vibrations in tube bundles.

A schematic representation of the same is as in Figure 1.2.

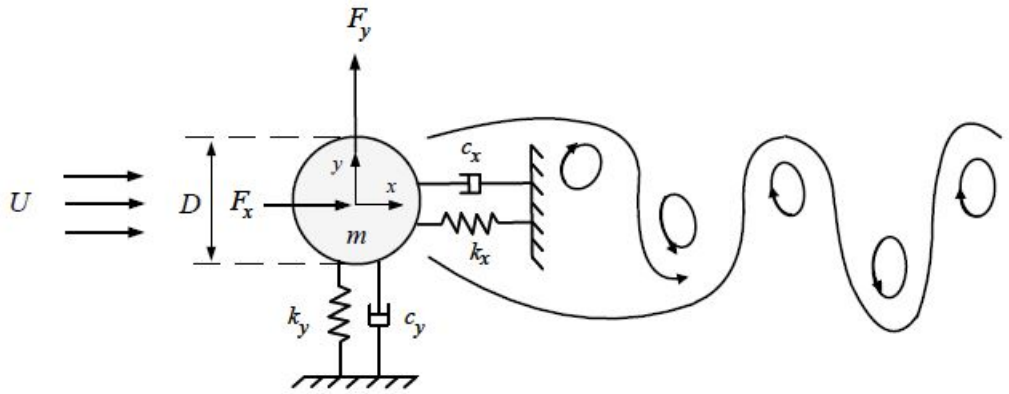

Figure 1.2: 2 DOF model representation of FIV

In systems where fluid interacts with solid structures, continual energy exchange occurs, driving the system toward equilibrium. The fluid loses energy due to viscosity, which is replenished by the continuous flow. This interaction is similar to two connected pendulums, where stability is crucial for maintaining coordinated movements. The fluid and solid systems influence each other, altering their movements in a mutual interaction. Given that the solid component communicates with the fluid efficiently, there occurs a mutual frequency adjustment known as *frequency lock-in.* Under certain conditions, their frequencies align, resulting in coordinated movements. This synchronization manifests as either vibrations or fluttering, both representing diverse forms of the same synchronized motion [19].

1.3. Fluid Structure Interaction

With the current availability of computational resources, the interest in computationally solving these Flow induced vibrations have increased, and is moreover preferred over experimental methods. Basically, the flow induced vibrations are analysed by modelling the Fluid Structure Interaction. Fluid-structure interaction (FSI) occurs when a flexible or flexibly mounted structure (a rigid structure that is supported by springs and dampers) is in contact with a flow, and the flow forces result in displacement or deformation of the structure. This movement of the structure causes changes in flow forces. This change in flow forces, in turn, results in changes in the structure's displacement and so on [20].

In these types of systems, the structural solver (FEM/ CSM) and flow solvers (CFD) are coupled such that the forces are computed over the fluid domain using the flow solver and then these computed forces are utilized in the structural solver to calculate the displacement and/or deformation. The modified structural domain is used to compute the modified fluid domain and the process is iterated until a converged local equilibrium is achieved. . A schematic flowchart of the same is in Figure 1.3

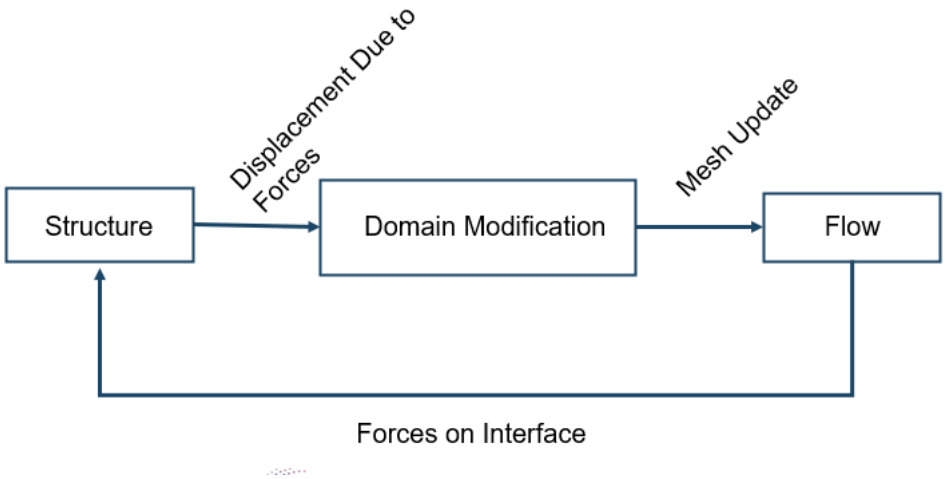

Figure 1.3: FSI mechanism

The thesis is primarily concerned with the fluid side of FSI, and the fluidic forces are computed using CFD techniques.

1.4. Computational Fluid Dynamics (CFD)

Computational Fluid Dynamics (CFD) is a branch of fluid mechanics that uses numerical methods to solve and analyze fluid flows. By utilizing high-performance computers and sophisticated mathematical models involving partial differential equations (PDEs), CFD simulates the behavior of fluids in a variety of conditions, such as airflow over an aircraft wing, the cooling of electronic components, or the mixing of chemicals in a reactor. They provide multiple advantages over wind tunnel methods:

- Less expensive and less complicated setup
- Uncertain boundary conditions
- Prone to plenty of random and systematic errors
- Model size restrictions due to the size of the tunnel and resulting Reynolds number effects
- Quantities can be extracted easily

CFD has evolved over time to improve computational time and at the same time precisely model the important elements of flow, such as turbulent structures. More details on the various turbulence models will be presented in Chapter 2.

1.5. Motivation and Research Objective

As mentioned previously, the flow part of FSI solver uses CFD to compute the pressure and friction forces. To be able to accurately predict these forces, accurate capturing of phenomena such as vortex shedding in turbulent flows is required.

Vortex shedding is a common feature in turbulent flow, for certain Reynolds number regimes

in the range of mainly $40 < \text{Re} < 3 \times 10^6$ particularly when dealing with bluff bodies like cylinders or flat plates in crossflow. In turbulent flows, vortex shedding leads to a regular pattern of alternating vortices being shed from either side of the object, creating a wake with complex flow characteristics. Accurate prediction of vortex shedding in turbulent flow is crucial because it significantly affects the pressure and friction forces on the object and induce vibration. This is called **Vortex Induced Vibration** The focus of this study is on the Vortex Induced Vibration over a cylinder in crossflow and can be extended to a tube bundle in crossflow.

The interaction between turbulent fluid and structure induces phenomena like vibration and resonance. Thus, turbulent flow characteristics need to be precisely computed to minimize numerical error and modelling errors. Numerical errors arise from the discretization of continuous mathematical equations and are inherent in any computational simulation. They primarily result from the approximation methods used in numerical algorithms. On the other hand, modeling errors arise from the simplifications, assumptions, and approximations made in the mathematical models themselves. These errors stem from the fact that the models used to represent physical phenomena may not fully capture all aspects of the phenomena.

Therefore, the solver needs to be able to resolve the turbulence scales with better precision. Numerous turbulence models have been briefed in Chapter 2 and out of them, the URANS (Unsteady Reynolds Averaged Navier-Stokes) model is a widely used option. However, URANS only calculates the forces resulting from the mean flow and models the approximate effect of fluctuations using models like $k - \varepsilon$ and $k - \omega$ [21] which leads to a high modelling error. On the other hand, LES (Large Eddy Simulations) resolves the large-scale turbulent structures (eddies) by applying a spatial filter to the Navier-Stokes equations. The smaller-scale turbulent motions, which are more chaotic and less influential on the large scales, are modeled using a subgrid-scale model. However it is excessively expensive. For instance, it took De Ridder [22] 2200 days in equivalent computational time to simulate 0.1 s of 1/10th the length of a fuel rod. This is not a realistic approach for commercial implementation.

Since both the RANS and the LES based turbulence calculation approach, as discussed in more depth in Chapter 2 have their limitations, the focus of this study is on bridging between the two types of models by using hybrid RANS-LES models. Hybrid RANS-LES algorithms offer a promising solution to this challenge by combining the strengths of both approaches. These hybrid methods, such as Detached Eddy Simulation (DES) and Scale Adaptive Simulation (SAS), aim to use RANS modeling in regions where the flow is relatively steady and well-predicted by the RANS approach, while switching to LES in regions where turbulence is more dynamic and complex. This switch can either be very explicit and segregate the domain into RANS and LES zones or it can be a subtle modification in the transport equations using either RANS or LES as baseline. This helps in reducing the computation expense in comparison to LES and also in resolving fluctuations instead of averaging them out like RANS.

After the review of the literature in Chapter 2, it was determined that hybrid RANS-LES models show a potential for improvement in computing turbulence in a more efficient manner. However, there has not been enough investigation done on the integration of Hybrid Turbulence Models into FSI applications, which can be highly relevant for studying and computing FSI and corresponding phenomena in more detail. Even the comparisons between different hybrid models were not comprehensively available. Moreover, since these hybrid models are comparatively new, incorporating them into open-source solvers is also a distinctive task.

Research Objective

To identify suitable Hybrid RANS-LES models, implement and validate them in open-source software, and compare them to shortlist the FSI-suited models.

The research objective is tackled by answering the following research questions:

Research Question 1

Which Hybrid Turbulence Models provides the most accurate flow solution for a stationary cylinder in crossflow case?

1. What is the grid sensitivity of these different models ?
2. Which of these models are most efficient and has least computation time?
3. What parameters should be considered essential for selection of turbulence model for a FSI case?
4. Which models from the available literature are most viable for FSI implementation?

Research Question 2

Are the selected Hybrid Turbulence models able to solve an FSI system?

1. Which parameters should be considered for the evaluation? How are the Hybrid Turbulence Models performing in calculation of these parameters?
2. What is the effect of Mesh Refinement?
3. How are they performing when compared to RANS models?

1.6. Methodology and Structure of the Report

Keeping the research objective in mind, a methodological and sequential process is established to address the aforementioned questions and achieve the final goals set for the current study. The report is divided into the following chapters:

Chapter 1: Introduction

The background and overview in Chapter 1. This chapter discussed the requirement of FSI in Nuclear reactors, followed by the motivation behind the study's applicability turbulence model and final research objective and research questions that are investigated in this thesis.

Chapter 2: Turbulence Model Selection from Literature

Given that numerous hybrid modelling approach are currently being developed, testing all of them for comparison is practically impossible. Therefore, the first step was to select the four most suitable models for further evaluation. For this a complex convenience selection approach was used. In this approach hybrid models were classified and categorised, removing approach categories unsuitable for the desired implementation and selecting the most viable hybrid model from each category.

Chapter 3: Numerical Case Setup

The next step is to select a validation case and to use that to set up the selected hybrid turbulence model. The OpenFoam inbuilt hybrid model for SA-IDDES is setup as the baseline for validation with respect to reference data available to evaluate parameters like Numerical discretision schemes, the filter parameter and numerical solvers. The k-ω SST-SAS model was also directly implemented from the available OpenFoam library. The PANS model was implemented from an available git repository of the work of Park [23]. The model was further evaluated to select appropriate modeling parameters. The SE library was created by modifying the Non Linear Eddy Viscosity Model (NLEVM) and the transport equations as per available literature.

The selection process of parameters like Discretisation Schemes, numerical solvers, timestep condition and convergence criteria becomes iterative. This situation arises in conditions like when a given discretisation scheme might not be feasible with one of the selected hybrid models and then to maintain consistency all the models are simulated using a standard scheme. The final selected parameters are discussed in the Chapter 3.

Chapter 4: Hybrid Model Comparison:

The comparison factors and variables were selected after careful consideration and then they were compared for all hybrid turbulence models to select the most efficient models in terms of simulation expense and result precision.

Chapter 5: FSI validation:

The shortlisted models are further compared for a Rigid Body Motion case which considers the object to be a rigid body that is free to translate along one axis. This is done to compare the models considering an FSI application.

Chapters 6 and 7: Conclusion and Recommendation:

Based on the outcome of the conducted comparative analysis a summarised conclusion regarding the models is made and represented in Chapter 6. This is followed by recommendation for the turbulence model selection based on the drawn conclusions in Chapter 7.

2

Literature Review

The proposed research scope is the development of FSI simulations using hybrid turbulence models, in the open-source computational fluid dynamics framework OpenFOAM. To this end, first, the available hybrid turbulence models published in open literature will be identified. So the literature review is divided into two components:

- Hybrid Turbulence Modeling
- Vortex-induced vibration and Important Parameters influencing VIV

Before delving in-depth into the hybrid turbulence model, the basics of turbulence modeling were investigated.

2.1. Turbulence Modeling

Turbulence is a continuum phenomenon because the smallest sizes of turbulence are quite significant in relation to molecular dimensions. Consequently, all of the physics of turbulent fluid motion may be found in the Navier-Stokes and mass-conservation equations. Nevertheless, accurate numerical simulations are feasible only at low Reynolds number and are still very expensive.

Turbulence is quite complex, which is the source of the difficulties. It is a three-dimensional, time-dependent phenomenon that is sustained by vortex stretching. The numerical analyst's work is made more difficult by a large range of scales that need to be resolved. The size of the object around which flow is being calculated can be compared to the largest, energy-bearing eddies, or scales.

The constant conversion of mechanical energy into internal energy is achieved by the smallest eddies which are characterized by significant vorticity. These tiny eddies, which exhibit local swirling or rotational motion, play a crucial role in this energy conversion process. With eddies of various sizes situated between the two extremes, the turbulence phenomenon is broadband.

The range of active scales must be included in an appropriate simulation; this range widens as the Reynolds number rises. We employ models to obtain reasonable computation times since accurate solutions for turbulent flow need a large amount of computing power. However, a model approximates the exact equations of motion so there are consequences [24]. Two of the most commonly used turbulence modeling approaches are RANS and LES.

2.1.1. Reynolds Averaged Navier Strokes (RANS)

The time-averaged fluid motion equations are known as the RANS equations. While still providing sufficient information for the majority of industrial and technical applications, the use of these time-averaged equations significantly reduces the amount of calculation time required. The task of a turbulence model is to close the RANS equations by computing the components of the Reynolds stress tensor.

The RANS equations divide velocity and pressure into mean and fluctuation components. This is referred to as Reynolds Decomposition as in (2.1) [25] where $\overline{U}$ represents mean flow velocity and U' is the fluctuation.

$$U = \overline{U} + U' \tag{2.1}$$

These decomposition serve as the input to Navier Strokes Equation to get the RANS equation

$$\rho\frac{\partial\overline{u}}{\partial t} + \rho\overline{u}.\nabla\overline{u} = \nabla\overline{p} + \nabla(2\mu S - \rho\overline{u'_j u'_i}) \tag{2.2}$$

where $\rho\overline{u'_j u'_i}$ is Reynolds Stress tensor, S is strain rate tensor,$\overline{u}$ is the mean velocity, ρ is density,μ is viscosity and $\overline{p}$ is mean pressure. From the Navier-Stokes equations, a set of transport equations can be derived to determine the components of the unknown Reynolds stress tensor. However, these equations contain high order terms that introduce complexity. Specifically, the Reynolds stress equations depend on higher order moments of the velocity field, which in turn, rely on even higher-order moments. This cascading dependence creates a closure problem, making it challenging to solve the equations directly.

A well known extension of the RANS model is the Unsteady-RANS model. As the name suggests, additional terms are utilized in order to account for the slow unsteady effects of a flow [26]. A URANS model is used especially when there exists a long-term periodical oscillation in turbulent flow, as it robust and efficient in terms of the utilized computational power. The URANS model is built from the RANS model by addition of the turbulent stress tensor term and is given by:

$$\frac{\partial\langle u_i\rangle}{\partial t} + \frac{(\langle u_i\rangle\langle u_j\rangle)}{\partial x_j} = -\frac{1}{\rho}\frac{\partial\langle p\rangle}{\partial x_i}\frac{\partial\langle\tau_{ij}\rangle}{\partial x_j} + \nu\frac{\partial^2\langle u_i\rangle}{\partial x_k^2} \tag{2.3}$$

where $\tau_{ij} = \langle u_i\rangle\langle u_j\rangle - \langle u_i u_j\rangle$ is the turbulent stress tensor. τ_{ij} is provided by a suitable turbulent model and will be briefed upon later.

Currently, directly solving these equation using Direct Numerical Simulation (DNS) technique is not suited for the simulation of turbulent engineering flows. This is due to the high computational cost and challenging numerical handling necessary to solve the transport equations system. The conventional method involves using a turbulence model to connect the unknown Reynolds stresses to the known mean flow values.

Therefore, different models are used to estimate this stress tensor. Two of the most popular methods for determining the unknowns in the Reynolds stress tensor are eddy viscosity models (EVM) and Reynolds stress models (RSM) [27].

Linear eddy viscosity models are the most widely employed closure models in engineering and industry applications. The Reynolds stresses are represented using the Boussinesq hypothesis, as in (2.4) , in the fundamental notion of linear EVMs.

$$\tau_{ij} = 2\mu_t S_{ij} - \frac{2}{3}\rho k \delta_{ij} \tag{2.4}$$

where μ_t is the eddy viscosity, k is the mean turbulent kinetic energy, and S_{ij} is the mean strain rate.

However, the accuracy of the two-equation models like $k-\varepsilon$ and $k-\omega$ model [24] is limited by the use of the Boussinesq eddy viscosity, which simplifies the complex fluid stress-strain relationship to a non-physical linear relationship. The use of linear eddy viscosity models and the Boussinesq hypothesis oversimplifies the turbulent stress-strain relationship, leading to inaccuracies in complex flows. This leads to a high **modeling error**. The Boussinesq assumption is invalid in flows with complex features due to poor prediction of turbulent viscosity from the use of this linear relationship. These URANS models don't actually resolve turbulence but rather try to model it effects using the models like EVM. Therefore, due to high modeling error it cannot be applied for Turbulence induced vibrations due to modelling error. Along with this, URANS models, due to their time-averaged nature, often fail to capture the instantaneous feedback between fluid forces and structural deformation.

2.1.2. Large Eddy Simulation (LES)

The Navier Stokes equations are used in LES to explicitly solve large, energetic, and geometry-dependent eddies, whereas smaller, sufficiently isotropic eddies are modeled implicitly. A resolved component, $\overline{u_i}$, plus a sub-grid component, u_i' , make up the velocity field in LES as in (2.5).

$$u_i = \overline{u_i} + u_i' \tag{2.5}$$

In order to account for the momentum exchange between resolved and modeled structures, sub-grid-scale (SGS) models are implemented. Although there are many different SGS closures, the Boussinesq hypothesis is used in the majority of SGS procedures to determine the SGS stresses [25].

The SGS stress is often computed using formulations similar to the Boussinesq hypothesis but tailored to the smaller scales as in (2.6). For example, the SGS stress tensor can be related to the resolved strain rate and modeled using the eddy viscosity approach. By modeling only the smaller scales and directly resolving the larger ones, the accuracy of the turbulence representation is improved compared to methods that model all turbulence effects, like RANS.

$$\tau_{ij} - \frac{1}{3}\tau_{kk}\delta_{ij} = -2\mu_t \overline{S}_{ij} \tag{2.6}$$

where μ_t is the subgrid scale turbulent viscosity, τ_{ij} is the SGS Stress tensor, δ_{ij} is Kronecker delta and $\overline{S}_{ij}$ is the rate of strain tensor for resolved scale and defined as follow:

$$\overline{S}_{ij} = \frac{1}{2}\left(\frac{\partial \overline{u_i}}{\partial x_j} + \frac{\partial \overline{u_j}}{\partial x_i}\right) \tag{2.7}$$

However, LES is computationally expensive and thus cannot be considered an efficient option. Big flow structures are deterministically predicted, and large eddy simulations are highly sensitive

to boundary and initial parameters. Therefore, accurate use of LES methods remains problematic. Boundary conditions that are not accurately resolved have the ability to bring significant inaccuracy into computed solutions. As a result, LES necessitate very tiny grids along the wall in order to accurately resolve the generated boundary layer. This leads to a high computational cost.

Furthermore, the spatial threshold used for turbulent structure filtering has a significant impact on simulation accuracy. The user defines the cutoff between “small” and “large” eddies; nevertheless, incorrect selection of this threshold might introduce inaccuracy into the solution. The flow-defining turbulent formations cannot be correctly portrayed if the spatial mesh size is too large. The high computational cost of simulating turbulence on a fine mesh is a major limitation of Large Eddy Simulation (LES). However, using a larger scale introduces significant numerical errors. These difficulties render LES ineffective for accurately computing turbulence-induced vibrations.

2.2. Hybrid Turbulence Modelling

RANS models are efficient for simulating turbulence over large scales by averaging out the effects of turbulence, which simplifies the computational requirements. However, RANS models often lack the ability to accurately capture the complex, high-frequency fluctuations and detailed turbulence structures necessary for accurate simulation of turbulence-induced vibrations. This limitation of high modeling error is particularly evident in wall-bounded flows, where the interaction between the fluid and solid structures can involve intricate and dynamic turbulent behaviors.

Conversely, LES provides a more detailed depiction of turbulence by resolving large-scale structures and modeling only the smaller, subgrid scales. While LES offers improved accuracy for turbulence representation, it demands significantly more computational resources due to the fine resolution required for the large-scale turbulence structures.

Since RANS and LES cannot be used for turbulence modeling for simulating turbulence induced vibration, therefore, it is necessary to strike a balance between the precision of physical modeling and the associated computing cost, particularly for wall-bounded flows. Creating hybrid RANS-LES algorithms is a viable solution to this challenge.

Hybrid RANS-LES algorithms offer a promising solution to this challenge by combining the strengths of both approaches. These hybrid methods, such as Detached Eddy Simulation (DES) and Scale Adaptive Simulation (SAS), aim to use RANS modeling in regions where the flow is relatively steady and well-predicted by the RANS approach, while switching to LES in regions where turbulence is more dynamic and complex. This switch can either be very explicit and segregate the domain into RANS and LES zones or it can be a subtle modification in the transport equations using either RANS or LES as baseline.

Despite the apparent similarity between RANS (Reynolds-Averaged Navier-Stokes) and LES (Large Eddy Simulation) in how they handle turbulent length or time scales, constructing effective hybrid RANS-LES systems remains challenging. The core issue arises from the different ways these models approach turbulence: LES is designed to resolve and simulate large-scale turbulent fluctuations directly, including those at boundaries, while RANS aims to average out these fluctuations to model the mean flow behavior. This fundamental difference creates difficulties in integrating the two approaches effectively. [28]. Various hybrid RANS-LES models have been proposed to address these challenges by combining the strengths of both methods, as discussed in

the following sections.

2.3. Classification of Hybrid Modelling

There are two basic guiding concepts that have mostly served to distinguish most proposed hybrid RANS LES techniques.

Zonal Method:

The first is the notion that the distinct techniques of RANS and LES are mature and well understood; hence, combining these technologies in the most efficient way is the best path forward. Such approaches are commonly referred to as **zonal or segregated approaches** [29].

The goal of zonal techniques is to integrate LES regions or other scale-resolving methods like DNS within a RANS solution with an explicit, time-fixed interface defined. Each subdomain is then solved independently using a different set of transport equations.

- **Bulk Zonal Approach**
  In bulk zonal techniques, the RANS domain provides boundary conditions for the LES region. Typically, the interfaces between these domains are oriented normal to the mean-flow direction. These interfaces can either be one-way, where information is conveyed solely in the direction of the mean flow, or two-way, allowing continuous interaction between the RANS and LES zones. A smaller LES region can significantly reduce computational costs, while capturing specific turbulence characteristics or physical phenomena that RANS models might not handle as effectively. However, the *grey area*—the transitional region between RANS and LES—can present challenges, especially for Fluid-Structure Interaction (FSI) applications [30].
- **Embedded LES**
  The Embedded LES (ELES) model integrates an inner LES domain within an outer RANS domain, facilitating seamless data transfer between them. Unlike other zonal hybrid LES/RANS methods like Detached Eddy Simulation (DES), the ELES model distinctly separates LES and RANS zones with predefined boundaries before the simulation starts. Each zone operates independently, solving its respective equations. The ”LES Boundary” and ”RANS Boundary” patches overlap to ensure smooth information exchange, enabling accurate simulations by mitigating fluctuating pressures at the interfaces. The primary challenge in the ELES model lies in effectively connecting these separate zones, requiring seamless exchange of field information across domain interfaces throughout the simulation. While zonal methods have their zones defined during simulations based on local parameters like grid size, viscosity etc, ELES zones are predefined.

Global Method:

The second finding is that both frameworks have similarities in their derivation and functional form (especially for unsteady RANS equations). This has prompted the creation of **seamless (or ’global’) frameworks** that try to modify the function of a single baseline model, whether RANS or LES, to include the capabilities of the other.

The algorithm can automatically switch between URANS and LES operation. The continuous treatment of flow variables, whether they function in URANS (typically in wall-adjacent areas) or

LES mode, is the foundation of seamless techniques. In the latter case, the RANS solver serves as an SGS model. As a result, the identical equations are solved in time-dependent mode throughout the entire domain (i.e., they include both regions) using the same numerical solution algorithm [29].

- **Blended Methods:**
  Blended approaches are designed to adaptively transition between different turbulence modeling strategies depending on the mesh resolution. In coarse-mesh simulations, these methods effectively revert to a robust Reynolds-Stress Model (RSM) scheme, which provides detailed modeling of turbulent stresses. In contrast, as the mesh resolution becomes finer, these approaches automatically transition to a Direct Numerical Simulation (DNS) or LArge Eddy Simulation (LES) mode, which resolves turbulence without the need for additional modeling. This adaptive strategy ensures that the simulation remains accurate across various levels of mesh refinement. The Flow Simulation Methodology (FSM) uses a function to combine RANS and DNS by adjusting the stress tensor based on the local grid size. In practice, this is accomplished through an explicit averaging process, which requires a uniform spatial orientation, meaning that it assumes a consistent directional alignment across the grid. This limits the overall applicability of this formulation because there will be no homogeneous direction in more complex situations.

- **Unified Methods**
  A group of methods known as *unified, bridging RANS-LES, sensitized RANS, or even second-generation*. Essentially, the URANS models are made more sensitive to internal instabilities by lowering the effective eddy viscosity. This is commonly accomplished by increasing the dissipation rate of the simulated turbulent kinetic energy in a continuous and thus seamless way, either across the entire flow or in places prone to instabilities [30].

  According to Spalart et al. (2021)[30], in zonal hybrid models, in the transition zone that is outside the boundary layer (RANS region) but has mesh not refined enough for LES leads to inaccurate capturing of flow dynamics. Embedded LES has zones that need to be predetermined which means isn't adaptive or robust and therefore is removed from the scope of this study. According to Hanjalic et al. (2021) [31], Blended models can switch between RANS and LES at unfavorable locations and there is less control of over this transition, as there can be in zonal and hence is removed from the scope of this study.

  The hybrid models from the remaining subcategories are selected from literature for each case.The SA- IDDES model is selected from Bulk Zonal methods due to its availability as an inbuilt model in OpenFoam and better definition in transition zone in comparison to other inbuilt DES models. Similarly SAS was also selected due to its availability. For Grid Dependent Unified methods PANS was selected because of its robustness and available literature while Struct Epsilon (SE) was selected because of its novelty and robustness.

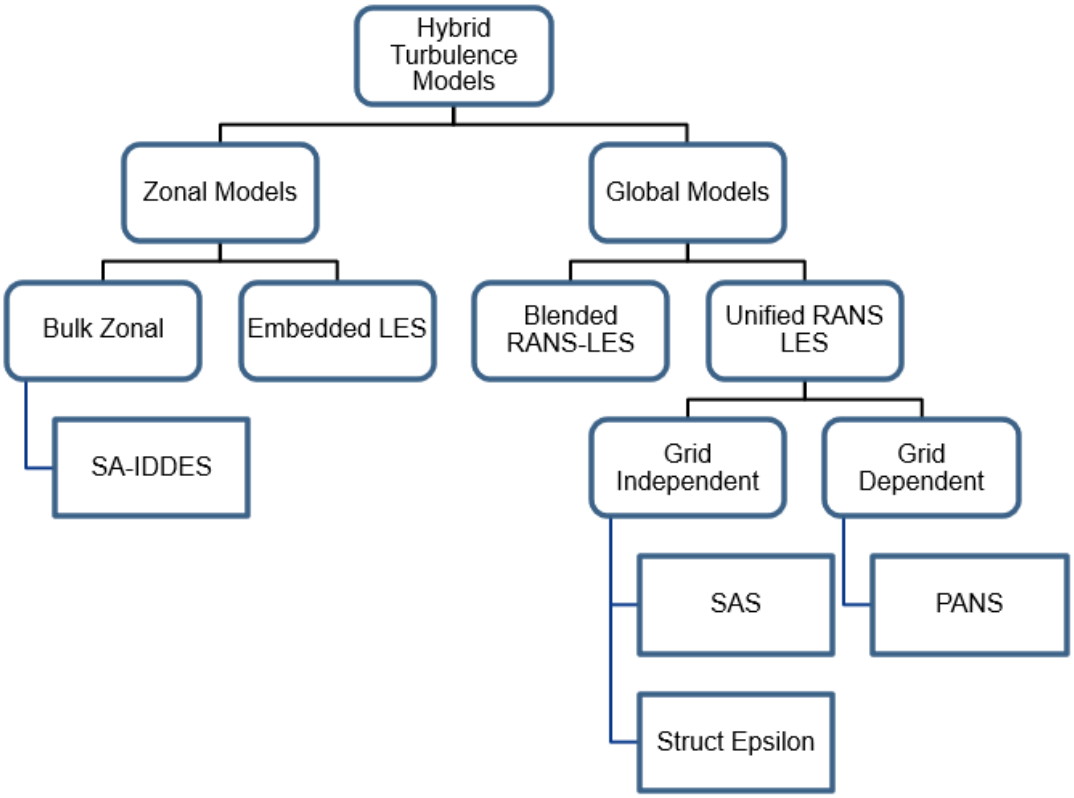

Figure 2.1: Classification of Hybrid RANS-LES models

2.4. Shortlisted Models based on literature

2.4.1. SA-IDDES

The IDDES model is designed by integrating wall-modeled LES (WMLES) with Delayed Detached Eddy Simulation (DDES) to address the log layer mismatch (LLM) problem while preserving the general compatibility of the DES model. Log layer mismatch is basically the mismatch of velocities that occur in between the RANS and LES models. Logrithmic layer of turbulence occurs in the transition zone between near wall flow and free flow. In all the variants of DES, the near wall boundary layer is computed using RANS and the far field using LES. This leads to formation of a transition region where a transition of characteristics from RANS to LES occurs.

When this transition is not smooth, it can cause discontinuity and inaccuracies in the flow field. The primary enhancement of the IDDES model is evident in the near-wall adjustment of the LES filter, which allows for a more seamless transition between RANS and LES regions compared to the original DES model.

Detached eddy simulation is a grid dependent seamless model that was first constructed on one-equation SA model with an SGS filter. Depending on the grid resolution, the filter can switch between RANS and LES mode.

Afterwards, a similar formulation is applied to two-equation SST model, which is based on a criterion between maximum local grid scale $\Delta = max(\Delta x, \Delta y, \Delta z)$ and turbulence length scale

$L_{DES} = min\{d_w, C_{DES}\Delta\}$ [32] where, L_{DES} is the length scale,d_w is the distance to the wall involved in the destructive term of the S-A model, C_{DES} is a derived constant = 0.65.

The S-A model transport equation for turbulent viscosity is shown below

$$\frac{d\tilde{\nu}}{dt} + U_j\frac{d\tilde{\nu}}{dx_j} = c_{b1}\tilde{S}\tilde{\nu} + \frac{1}{c_\sigma}[\frac{\partial}{\partial x_j}(\nu + \tilde{\nu}))\frac{d\tilde{\nu}}{dx_j}] - c_{\omega 1}f_\omega(\frac{\tilde{\nu}}{d_w})^2 \tag{2.8}$$

where $\tilde{\nu}$ is turbulent viscosity,$U_j\frac{d\tilde{\nu}}{dx_j}$ is convection term, $c_{b1}\tilde{S}\tilde{\nu}$ is production term followed by 2 diffusion and dissipation terms.

For DES application, the distance to wall d_w is replaced by L_{DES} [33].

Physically this means that if the distance from the wall $d_w < C_{DES}\Delta$ the code operates in RANS mode else LES mode gets activated. As can be noticed from this definition, the transition in the DES model is rather abrupt. Therefore the SA-IDDES model variant of DES is considered.

The SA-IDDES model works on a similar modeling machanism as SA-DES but the length scale in SA transport equation is modified to L_{IDDES} as shown in (2.9).

$$\frac{d\tilde{\nu}}{dt} + U_j\frac{d\tilde{\nu}}{dx_j} = c_{b1}\tilde{S}\tilde{\nu} + \frac{1}{c_\sigma}[\frac{\partial}{\partial x_j}(\nu + \tilde{\nu}))\frac{d\tilde{\nu}}{dx_j}] - c_{\omega 1}f_\omega(\frac{\tilde{\nu}}{L_{IDDES}})^2 \tag{2.9}$$

The length scale L_{IDDES} is a blended function of WMLES and DDES length scales and thus provide a smooth transitioning. It considers WMLES for near wall region in case the flow is not attached. In other scenarios it acts as DDES. The lngth scale is calculated as follow:

$$L_{IDDES} = \tilde{f}_d(1 + f_e)L_{RANS} + (1 - \tilde{f}_d)L_{LES} \tag{2.10}$$

where the length scale L_{LES} is defined as $C_{DES}\Delta$. The grid scale $\Delta = min[\max C_w(\Delta_{max}; d); \Delta_{max}]$ with C_w being a constant, *d* the distance to the nearest wall and $\Delta_{max}$is equal to max($\Delta x, \Delta y, \Delta z$)

The function $\tilde{f}_d$ is defined as max $[1 - f_d, f_B]$ which is determined by both the geometry part f_B and the flow part $(1 - f_d)$. Here, f_d is delayed function and defined as $f_d = 1 - tanh[8(r_d)^3]$ where r_d is as defined in the original SA transport equation. Similarly f_e is a blending coefficient defined for WMLES part of the blending function [34]. The length scale defining the switch from RANS to LES in DES model is just a function of grid size but for IDDES this switching length scale is a function of eddy viscosity along with the grid which makes it more robust than DES model.

For k-ω SST model of IDDES, IDDES formulation is done by modifying isotropic dissipation ε. The dissipation term in the *k* equation, D_k, is modified in order to reduce the eddy-viscosity in LES regions and is written as [35]:

$$D_k = \frac{\rho\sqrt{k^3}}{L_{IDDES}} \tag{2.11}$$

2.4.2. SST-SAS

The SAS technique is essentially an improved URANS formulation that can employ any of the existing Reynolds-averaged turbulence models while allowing turbulence structures to be

(partially) resolved for highly separated and unsteady flows employing the von Karman length scale (L_{vK}) into the scale-determining equation of RANS turbulence models [36]. The key idea is to introduce a term that senses the turbulent length scales in the flow and adapts the model's behavior accordingly. L_{vK} is defined as the ratio of the first velocity derivative divided by the second derivative (times the von Karman constant $\kappa = 0.41$, U_i being the velocity vector) :

$$L_{vK} = \kappa \left| \frac{U}{U''} \right|; \qquad U'' = \sqrt{\frac{\partial^2 U_i}{\partial x_k^2} \frac{\partial^2 U_i}{\partial x_j^2}}; \qquad U' = \sqrt{2 S_{ij} S_{ij}} \tag{2.12}$$

where $S_{ij} = \frac{1}{2}\left(\frac{\partial U_i}{\partial x_j} + \frac{\partial U_i}{\partial x_i}\right)$.

L_{vK} enables the turbulence model to identify resolved scales in unstable flows and modify the eddy-viscosity to a level that allows the generation of a turbulent spectrum. This scale indicates the maximum size of eddies that can be sustained by the flow. In areas with large gradients or unsteadiness, the von Kármán scale becomes smaller, indicating that finer scales of turbulence need to be resolved or modeled. It does this by introducing unsteady characteristic into the model. For example additional max function term Q_{SAS} is added to the ω equation of SST model which is zero for RANS simulation but activates the SAS otherwise [37].

$$\frac{\partial pk}{\partial t} + \nabla \cdot (\rho U k) = P_k - \rho C_\mu k\omega + \nabla \cdot [(\mu + \sigma_k \mu_t)\nabla k] \tag{2.13}$$

$$\frac{\partial p\omega}{\partial t} + \nabla \cdot (\rho U \omega) = \alpha \frac{P_k}{\nu_t} - \beta \rho \omega^2 + \mathbf{Q_{SAS}} + \nabla \cdot [(\mu + \sigma_\omega \mu_t)\nabla \omega] + (1 - F_1)\, \frac{2\rho\sigma_\omega^2 \omega}{\omega} \nabla k \cdot \nabla \omega \tag{2.14}$$

where Q_{SAS} is defined by:

$$Q_{SAS} = \max \left[\rho \xi \kappa S^2 \left(\frac{L}{L_{vk}}\right)^2 - C \cdot \frac{2pk}{\sigma_\varphi} \max \left(\frac{|\nabla \omega|^2}{\omega^2}, \frac{|\nabla k|^2}{k^2} \right), 0 \right] \tag{2.15}$$

where S is the invariant measure of the strain rate tensor, defined as $S = \sqrt{2 S_{ij} S_{ij}}$, with $S_{ij} = \frac{1}{2}\left(\frac{\partial u_i}{\partial x_j} + \frac{\partial u_j}{\partial x_i}\right)$. The constants in the equation are: $C = 2.0$, $\xi = 3.51$, $\kappa = 0.41$, $\sigma_\varphi = \frac{2}{3}$, and $C_\mu = 0.09$. The turbulence scale L is defined as $L = \sqrt{\frac{k}{(C_\mu)^{1/4}\omega}}$.

The von Karman length scale filter is used to reduce the explicit influence of grid spacing on the changeover between RANS and LES, which is present in the most popular hybrid RANS/LES technique, DES.

The SAS source term Q_{SAS} becomes significant in regions where the turbulence scales are large and unsteady behavior is present. When this term is active, it reduces the modeled eddy viscosity,

allowing the flow solver to resolve more of the turbulent structures directly. The eddy viscosity is a function of ω and the Q_{SAS} term modifies the ω.

Opting for SAS is a more conservative choice, as it does not switch from RANS to LES when the simulation's spatial or temporal resolution is insufficient for LES. This conservative nature of SAS makes it better suited for complex applications where the computational grid may not adhere to LES specifications. [38].

2.4.3. PANS

The PANS model, developed by Girimaji, Srinivasan, and Jeong [39] is a general hybridization approach that is a recent addition to hybrid method of modeling turbulence. It is a suite of turbulence closure models of various filter widths ranging from Reynolds averaged Navier-Stokes (RANS) to direct numerical simulation (DNS) [25].

The basic principle behind PANS model is the turbulence is split into resolved and modeled components by adjusting the amount of turbulent kinetic energy and the dissipation rate that are directly solved (resolved) versus those that are modeled. The starting point for PANS is from the incompressible Navier Strokes and Continuity Equation in (2.16) where V and p represent the velocity and pressure fields.

$$\frac{\partial V_i}{\partial x_i} = 0 \tag{2.16}$$

$$\frac{V_i}{\partial t} + V_j \frac{\partial V_i}{\partial x_j} = -\frac{\partial p}{\partial x_i} + \nu \frac{\partial^2 V}{\partial x_i \partial x_j} \tag{2.17}$$

Assuming that the scale resolution remains fixed, $\langle\rangle$ represents the generalized homogeneous filter which is fixed in space and time. Considering U be the filtered velocity and u' is the sub-filtered component

$$V_i = U_i + u_i', \quad U_i =< V_i >, \quad < u' > \neq 0 \tag{2.18}$$

$$p = P + p', \quad P =< p >, \quad < p' > \neq 0 \tag{2.19}$$

Then, the resolved field can be represented by the following equation:

$$\frac{U_i}{\partial t} + U_j \frac{\partial U_i}{\partial x_j} = -\frac{\partial \tau(U_i, U_j)}{\partial x_j} - \frac{\partial P}{\partial x_i} + \nu \frac{\partial^2 U_i}{\partial x_i \partial x_j} \tag{2.20}$$

$$\partial \tau(U_i, U_j) =< U_i U_j > - < U_i >< U_j > \tag{2.21}$$

wherein τ_{ij} is the sub-filter stress as a physical expression or generalized central second moment as a mathematical expression. (2.20) is *unclosed* due to the presence of the sub-filter stress term $\partial \tau(U_i, U_j)$.

To provide the closure it is assumed that Boussinesq Equation is applicable to PANS model

$$\tau_{ij} = \tau(U_i, U_j) = \frac{2}{3} k_u \delta_{ij} - \nu_u \left(\frac{\partial U_i}{\partial x_j} + \frac{\partial U_j}{\partial x_i} \right) \tag{2.22}$$

$$\nu_u = \frac{k_u}{\omega_u} \tag{2.23}$$

Here, k_u, ω_u and ν_u are the unresolved kinetic energy, turbulence frequency, and viscosity, respectively. Besides, the closure of k_u and ε_u is accomplished with a PANS k_u-ω_u model that is derived from a parent RANS $k-\omega$ model

$$\frac{\partial k_u}{\partial t} = U_j \frac{\partial k_u}{\partial x_j} = P_u - \beta^* k_u \omega_u + \frac{\partial}{\partial x_j}\left[\left(\frac{\nu_u}{\sigma_{k_u}}\right)\frac{\partial k_u}{\partial x_j}\right] \tag{2.24}$$

$$\frac{\partial \omega_u}{\partial t} = U_j \frac{\partial \omega_u}{\partial x_j} = \alpha \frac{\omega_u}{k_u} P_u - \beta' \omega_u^2 + \frac{\partial}{\partial x_j}\left[\left(\frac{\nu_u}{\sigma_{\omega_u}}\right)\frac{\partial \omega_u}{\partial x_j}\right] \tag{2.25}$$

where P_u is unresolved production turbulent kinetic energy term and can be expressed as a function of filter control parameters: f_k, the ratio of unresolved-to-total kinetic energy f_ω, the ratio of unresolved-to-total specific dissipation rate.

$$P_u = \nu_u \left(\frac{\partial U_i}{\partial x_j} + \frac{\partial U_j}{\partial x_i}\right) = f_k \left(P - \beta * \frac{k_u \omega_u}{f_\omega f_k}\right) + \beta^* k_u \omega_u \tag{2.26}$$

where $\beta^*, \alpha, \beta, \sigma_k, \sigma_\omega$ are modeling parameters explained in detail by Chakraborty [40].

In PANS, k-ε model, the filter width is controlled by two filter parameters which are f_k andf_ω, Also, $f_\omega = f_k/f_\varepsilon$, where f_ω is the ratio between modeled and resolved turbulent dissipation rate. Each f_k corresponds to a different cut-off filter in the energy spectrum. By specifying these parameters, the model can be tailored for any degree of physical resolution between RANS and DNS. The grid resolution must be adequate to capture the fluctuations liberated by the model.

$$f_k = \frac{k_m}{k} \qquad\qquad f_\varepsilon = \frac{\varepsilon_m}{\varepsilon} \tag{2.27}$$

When f_k = 1 and f_ε=1, the model acts like URANS since the smallest scales in PANS are also the smallest scales in URANS. Model hybridization happens for values of $0 < f_k < 1$, and the turbulence dissipation rate is changed using this ratio. Because PANS allows for the use of a coarser grid than required for LES, the computational cost of completing a CFD simulation is reduced. The fundamental issue in implementing the model, however, is that the determination of the PANS control parameters which is dependent on user-defined physical resolution, the grid size .

2.4.4. Struct-Epsilon (SE)

The approach is based on Lenci and Baglietto's original STRUCTure-based turbulence resolution concept (STRUCT). The model uses a $k-\varepsilon$ anisotropic nonlinear eddy viscosity model (NLEVM) with a cubic stress-strain relation as its baseline URANS, while allowing controllable scale resolution inside flow zones where the URANS scale separation assumption is not satisfied. Their NVLEM is further explained in Section 3.4.

The issue with baseline URANS is that it assumes that averaging time span T is larger than the turbulent time scale but is much lower than the period of slow variation in the flow. This implies a scale separation between turbulence and slow varying phenomena which doesn't hold true for flow phenomena such as vortices and flow separation.

The struct approach locally resolves a major portion of turbulent fluctuations by identifying the zones that require higher resolution by comparing the resolved and modeled time scales.This resolution change is done by modifying the resolution control parameters. The resolved time scale t_r is defined as function of Q- criteria as in (2.28)

$$t_r = |Q|^{-1/2} \tag{2.28}$$

The Q-criterion, which defines the local balance between shear strain rate and vorticity magnitude, is a helpful value for defining a turbulent structure, and is defined as (2.29) where S is strain rate tensor and Ω is vorticity tensor.

$$Q = -\frac{1}{2}\frac{\partial \overline{u_i}}{\partial x_j}\frac{\partial \overline{u_j}}{\partial x_i} = \frac{1}{2}\left(\overline{\Omega}_{ij}\overline{\Omega}_{ij} - \overline{S}_{ij}\overline{S}_{ij}\right) \tag{2.29}$$

The modeled time scale t_m is defined as the average of modeled scaled parameter $t_{m,0}$ where 0 denotes initial condition , to remove the smallest local turbulence variations to deliver a smooth t_m field, which is defined as follow:

$$t_m = < t_{m,0} > \tag{2.30}$$

$$t_{m,0} = \frac{k}{\varepsilon} \tag{2.31}$$

The basic STRUCT model introduces a resolution control parameter, r, which is the ratio between the TKE modeled by the hybrid turbulence closure and the TKE modeled by URANS, to regulate the content of the resolved field which multiplies the definition of eddy viscosity.

$$\nu_t = C_\mu \frac{k^2}{\varepsilon} r \tag{2.32}$$

$$r = \begin{cases} 1 & h \leq 1 \\ \phi & h > 1 \end{cases} \tag{2.33}$$

$$h = \frac{t_m}{t_r} \tag{2.34}$$

where h is activation parameter described as ratio of modelled time scale t_m and resolved time scale t_r and ϕ is a reduction coefficient. The reduction coefficient and averaging operation are the two closure condition of this model which has been tried to closed using variations of struct models such as Controlled Struct, Struct-T and Struct-L [41].

However, like with many hybrid turbulence models, the formulation fails when improper boundary conditions are used. STRUCT has showed undesirable hybrid activation in external flow applications when improper inlet conditions are given as the hybridisation region is defined based on user-defined inlet conditions. This is because the values of k and ϵ can transport through the entire domain in open flows and as modeled time scale, t_m and thus the resolution control parameter depends mainly on these values thereby improper hybrid activation can occur through the geometry. For instance if the k and ε defined by user equates to a large t_m, the entire domain has an active hybridization. Further details can be found in the work of Lenci et al. [42].

The STRUCT-ε model is developed to overcome the limitations of the original STRUCT technique. Instead of explicitly comparing the resolved and modeled time scales and introducing a reduction parameter on the eddy viscosity to enable hybridization, this model implicitly reduces the eddy viscosity by including a source term (in bold in (2.35)) in the ε transport equation of the standard k-ε model that is dependent on the second invariant of the resolved velocity gradient tensor (Q-criteria) [41].

$$\frac{\partial \varepsilon}{\partial t} + \frac{\partial \overline{u_j}\varepsilon}{\partial x_j} = \frac{\partial}{\partial x_j}\left[\left(\nu + \frac{\nu_t}{\sigma_\varepsilon}\right)\frac{\partial \varepsilon}{\partial x_j}\right] + C_{\varepsilon 1}\frac{\varepsilon}{k}P_k - C_{\varepsilon 2}\frac{\varepsilon^2}{k} + \mathbf{C_{\varepsilon 3}kQ} \tag{2.35}$$

The effect of this new term is comparable to that of the reduction parameter in the original STRUCT-T model [43]. Both models define hybridization zones as areas where the Q-criterion is greater than $\frac{\varepsilon}{k}$. Instead of adjusting eddy viscosity in certain places, it alters the ε equation everywhere. As a result, the hybridization region is no longer dependent on inlet turbulence conditions in the new model [25].

2.5. Vortex Induced Vibrations

The physics behind vortex induced vibration and the tool used to solve it, FSI, has been discussed in Chapter 1. This Section focuses on the the non-dimensional parameters that influence the flow behavior around objects prone to VIV. The most important ones are the Reynolds Number (Re) and the Strouhal Number (St).

2.5.1. Reynolds Number

Vortex shedding is primarily governed by the Reynolds number, Re, which is defined by

$$Re = \frac{UD}{\nu} \tag{2.36}$$

where U is the freestream velocity, D is the characteristic length (diameter of a cylinder for example) and ν is the kinematic viscosity.

The Reynolds number is used to separate flow into different regimes based on their physical properties. These regimes are explained as follow:

Laminar Flow (Re< 2000): Laminar flow occurs at low Reynolds numbers, typically below 2,000. In this regime, the fluid flows in smooth, parallel layers without any disruption between them. Each particle of fluid moves along a well-defined path, creating a highly ordered flow. This type of flow is often observed in small-diameter wires or thin rods in a fluid with low velocity, such as the flow in microfluidic devices or slow-moving fluids in small channels where precise control is required.

Transitional Flow (2000<Re< 4000): As the Reynolds number increases beyond 2,000, the flow begins to transition from laminar to turbulent. In this transitional regime, the flow over a cylinder starts to exhibit signs of increasing instability and unsteadiness. While vortex shedding can occur in laminar flows at lower Reynolds numbers, in this transitional regime, the process

becomes more pronounced and organized. Specifically, vortices shed alternately from each side of the cylinder, creating a periodic pattern known as the von Kármán vortex street. This transition is characterized by the onset of flow separation and more regular vortex shedding, leading to an intermediate state where both laminar and turbulent characteristics coexist. The flow becomes increasingly complex, with fluctuations in velocity fields and pressure distributions.

Turbulent Flow (Re> 4000): When the Reynolds number exceeds 4,000, the flow becomes fully turbulent. In this regime, the fluid motion is highly chaotic, with rapid and irregular fluctuations in velocity and pressure. For flow over a cylinder, the boundary layer transitions to a turbulent state before separating from the surface, resulting in a turbulent wake that is broad and filled with eddies and vortices.

For flow over a cylinder, the Reynolds number regimes can be further detailed into subcritical, critical, and supercritical regimes. In the subcritical regime (Re<200), the flow remains laminar and attached to the cylinder's surface, with a high drag coefficient due to early separation of the laminar boundary layer. The wake is symmetric and attached, as seen in slow-moving fluid over thin wires. As the Reynolds number increases into the critical regime (200<Re<3×10^5), the boundary layer transitions from laminar to turbulent, and vortex shedding becomes prominent. This results in a decrease in the drag coefficient as the turbulent boundary layer delays flow separation. In the supercritical regime (Re>3×10^5), the boundary layer is fully turbulent before separating, leading to a narrower and more chaotic wake with further reduced drag. This behavior is typical in high-speed flows over large-diameter pipes or cylindrical structures, such as those found in bridge piers or offshore platforms.

2.5.2. Strouhal Number

The Strouhal number, St, serves as a dimensionless constant that correlates the primary frequency of vortex shedding,f_s, with the free stream velocity,U, and the cylinder width,D. This relationship is captured by the equation:

$$f_s = \frac{StU}{D} \tag{2.37}$$

For a stationary circular cylinder in subsonic flow, the Strouhal number is influenced by the Reynolds number, with additional effects stemming from surface roughness and free stream turbulence as shown in Fig. 2.2. Notably, the impact of surface roughness is significant in the transitional flow regime. Cylinders with very smooth surfaces exhibit chaotic, disorganized wakes with high-frequency oscillations and Strouhal numbers reaching up to 0.5. In contrast, rough-surfaced cylinders display more organized, periodic wakes characterized by a Strouhal number of St=0.25. Generally, a Strouhal number of St=0.21 is assumed for single cylinders in cross flow conditions.

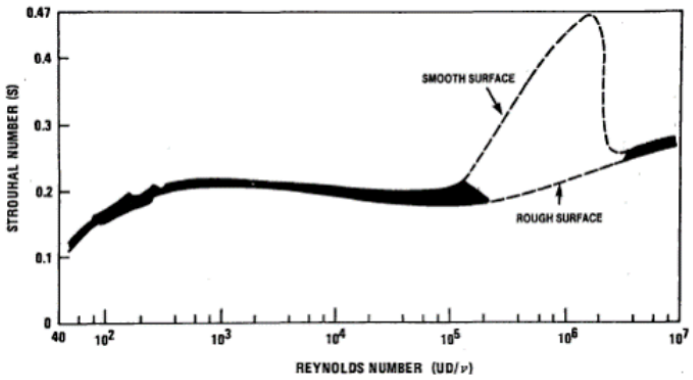

Figure 2.2: Strouhal Number variation with Reynolds Number

3

Numerical and Turbulence Model Setup

After shortlisting the hybrid models in Chapter 2, the next step is the implementation and validation of the models. This chapter focuses on the implementation of the different turbulence models and selection ad setup of the validation case. The IDDES and SAS models are available in the OpenFoam library and were directly implemented. The PANS and SE models were also incorporated, as will be discussed in this chapter.

3.1. Validation Case

The simple case of flow over a static straight circular cylinder at a low Reynolds number of 3900 is used first for the validation of the model and then for comparison purposes. The experiment conducted by Parnaudeau et al. [44] is used as an experimental reference. Parnaudeau evaluated the crossflow over a circular cylinder at Re 3900 using Particle Image Velocimetry (PIV) methodology and collected the results for the flow statistics at different locations in the wake region. In this validation, only flow statistics observed just behind the cylinder at x/D=1.06 were used.

D'Alessandro et al. [45] implemented SA-IDDES for a similar case with different length scales. It solves crossflow over a circular cylinder at Re 3900 using the pisoFoam solver in OpenFOAM, which handles pressure-velocity decoupling. Similar to other standard solvers, it employs a collocated FVM approach, incorporating the Rhie–Chow correction to eliminate solution oscillations. The diffusive terms and pressure gradients were approximated with second-order accuracy, and time integration was performed using the second-order implicit Euler method (BDF-2). A limited central difference scheme, based on Sweby's limiter, was applied to the turbulence equation, while a second-order central scheme was used for the momentum equation.

These two literature are used as references for the validation of the models as well as numerical and solver schemes.

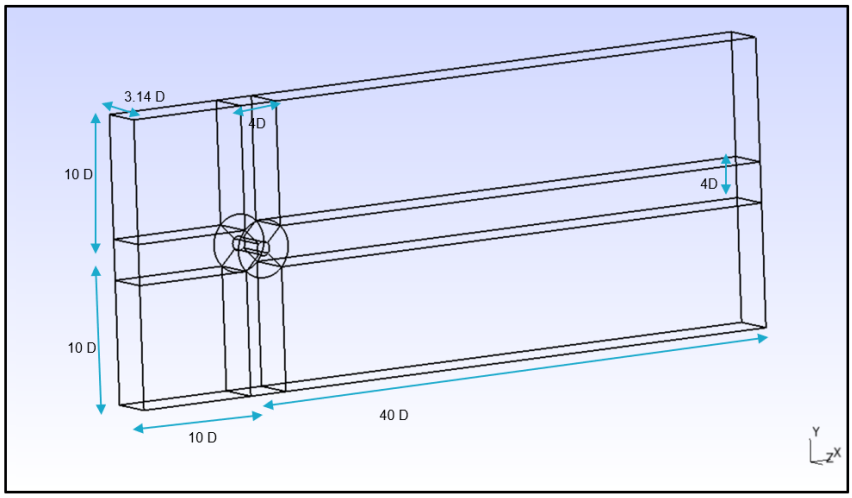

Figure 3.1: Computational Domain

The domain as shown in Figure 3.1 is defined as a three-dimensional domain with origin at the center of the cylinder, having a distance of 10 D between the cylinder center and the inlet where the inflow boundary condition is used. The wake region domain extends to $40D$ behind the cylinder. The distance between the upper and lower limits of the computational domain is 20 D with the cylinder length being πD. The computational domain is also equipped with a refined near wall region of radius 2D to minimize numerical error.

Four different structured computational grids have been generated, the mean parameters of which are listed in Table 3.1. The finest grid A8 has approximately 6.5M cells with span-wise length L_z of πD discretized into 48 cells. This estimation was adopted from Kravchenko an Moin [46] that assesses the sizes of stream-wise vortex structures.

The mesh is divided into 2 sections. The near wall region of a radius of 2D where more scales need to be resolved and the far field beyond it. The near wall field is defined such that the last layer thickness is equal to the circumferential size of the cells to make those cell with a projected square area. The circumference of cylinder at radius 2D is divided into 44*A cells and span-wise is divided into 6*A cells. Where A is the mesh size defining parameter as in Table 3.1. In the far field the mesh has a constant growth rate proportional to edge length.

Table 3.1: Mesh Levels considered for the domain

Mesh level	n_θ (44*A)	n_z (6*A)	n_{cells}
A2	88	12	110 K
A4	176	24	950 K
A6	264	36	2.9M
A8*	352	48	6.5M

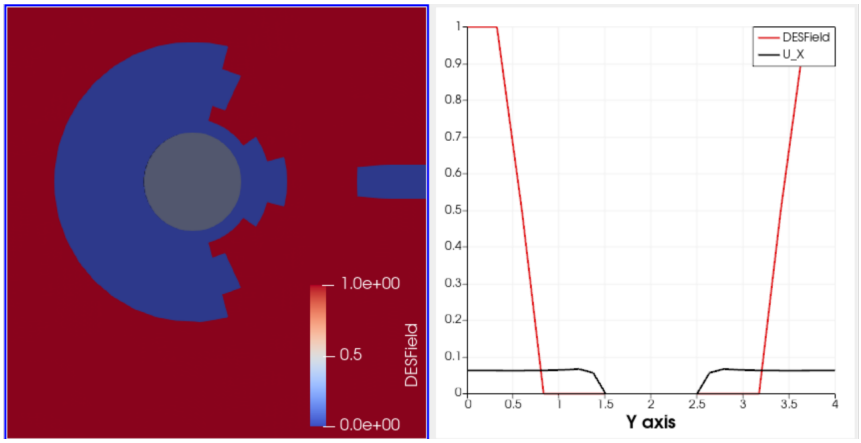

(a) $\delta = D/10$

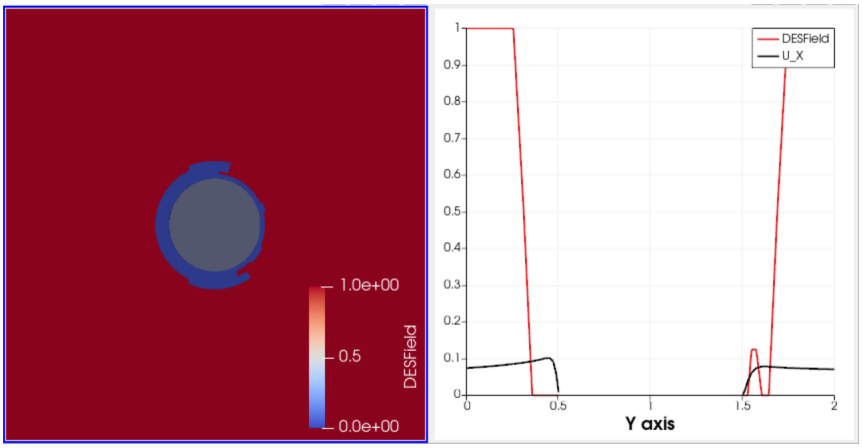

(b) $\delta = D/100$

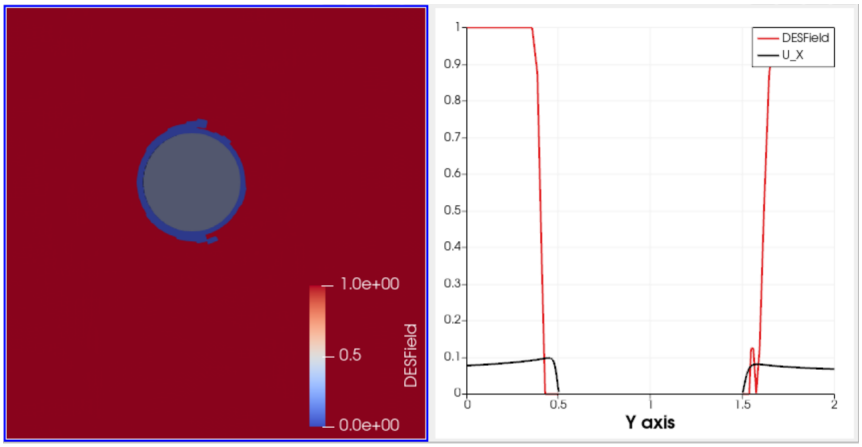

(c) $\delta = D/1000$

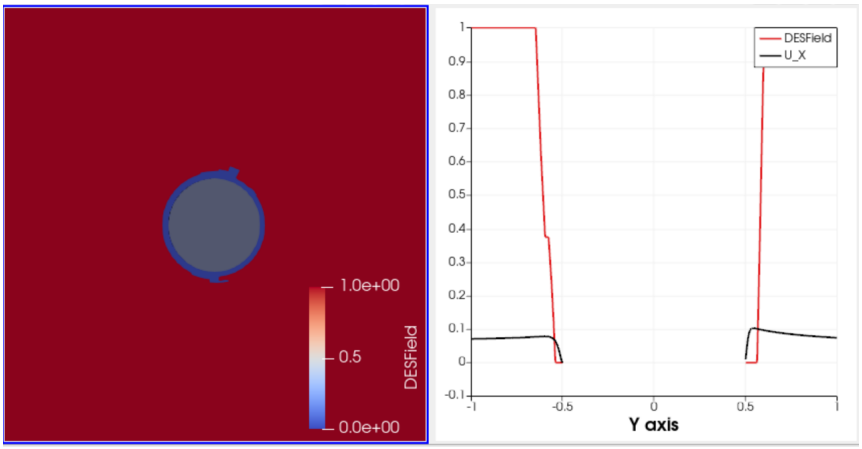

(d) $\delta = D/5000$

Figure 3.2: DES field regions for different first layer thickness δ

The first layer thickness according to Schroder et al [18] should be such that y^+ <1 to get better accuracy. However,for IDDES, it is ideal to have the RANS part of IDDES activated in the near wall boundary layer region and LES to solve flow equation beyond that. Therefore, a comparative study was conducted with different first layer thicknesses on the Mesh A6 for efficiency to evaluate the most appropriate first layer thickness with respect to the switch between RANS and LES along the boundary layer. The results of the streamwise velocity U_x along the y-axis (y/D) of the domain, representing the boundary layer, are shown in Figure 3.2. Additionally, the DESField variable, which indicates the mode of simulation, is also depicted. In this context, the DESField is a binary variable, where a value of corresponds to regions where the LES model is active, and a value of 0 corresponds to regions where the RANS model is applied.

As can be easily concluded from the results shown, the decrease in the thickness of the first layer provides a clear distinction between RANS and LES at the boundary layer. Therefore the first layer thickness was selected to be D/5000. This selection was extended to all mesh sizes. The first layer thickness is kept constant across models to maintain consistency.

The final Mesh A8 based on the selected parameters is as in Figure 3.3.

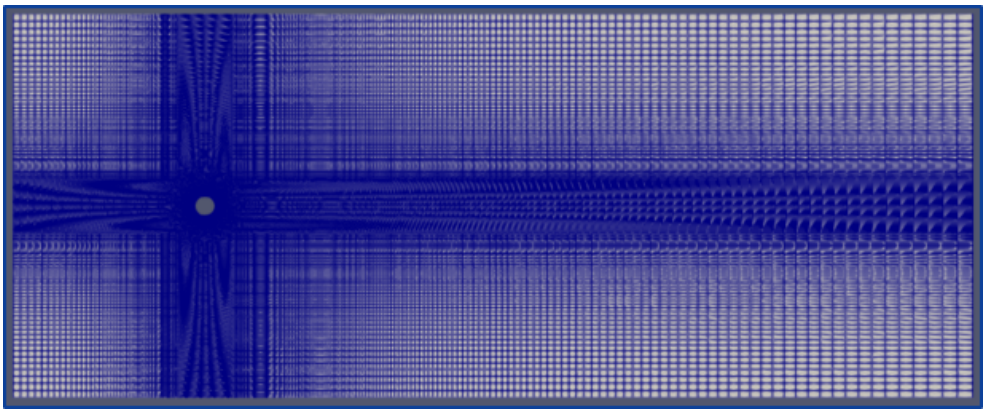

(a) Mesh A8

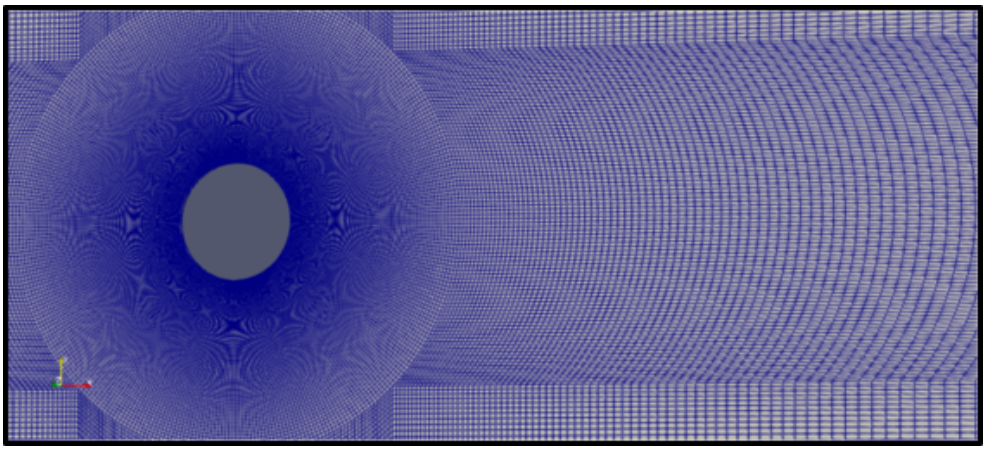

(b) Near wake Region

Figure 3.3: Mesh Figures

3.2. Numerical Scheme Selection

OpenFoam v2212 is used to perform all computations using pimpleFoam, a transient solver for incompressible flow. pimpleFoam is a combination of PISO (Pressure Implicit with Splitting of Operators) and SIMPLE (Semi-Implicit Method of Pressure Linked Equation) algorithms adapted for complex flows where pressure-velocity coupling is important.

All the diffusive terms and pressure were approximated with second order accuracy whereas the backward scheme for time marching. For the convective terms for DES derived models, DeAlessandro et al. [45] recommend using the Gauss-Sweby limiter as in Appendix A.2 but it became unstable for SAS. Therefore, to maintain consistency, different schemes were compared, and the Gauss LimitedLinear scheme was selected. Additionally, Gauss linearUpwind linear scheme was chosen for the momentum equation to balance accuracy and numerical stability.

The velocity and turbulence equations were solved using a preconditioned bi-conjugate gradient method (PBiCG) with a diagonal incomplete-LU preconditioner, while the pressure equation was solved using a preconditioned conjugate gradient method (PCG) with a diagonal incomplete Cholesky preconditioner. The pressure system was solved with a local accuracy of 10^{-6}, and the other systems were considered converged at residuals of 10^{-9}.

The timestep is defined using a Courant-Friedrichs-Lewy (CFL) condition, also known as Courant Number (Co), as in (3.1) set to 0.5. Here u is the velocity of fluid, Δt is timestep size and Δx is the grid size. This choice ensures that the numerical stability and accuracy of the simulation are maintained by limiting the maximum allowable timestep, such that the physical time taken for a fluid particle to traverse a computational cell is no more than half of the timestep. This conservative CFL value helps prevent numerical instabilities and improves the reliability of the simulation results.

$$CFL = \frac{u\Delta t}{\Delta x} \tag{3.1}$$

3.3. PANS Filter Parameter Analysis

PANS was implemented taking the work of Park [23] as a baseline. Their version of PANS was adapted and incorporated into OpenFoam v2212. However as discussed in Chapter 2, filtering parameters are essential for filtering the resolved and modeled scales. Therefore, selection of f_k and f_ε is a crucial part of implementing PANS, as it directly influences the accuracy of the simulation. It is crucial to understand that large scales contain most of the kinetic energy, and viscous dissipation occurs at smaller scales. This means that filtering parameters must satisfy the condition $0 \leq f_k \leq f_\varepsilon \leq 1$, ensuring that the energy distribution and dissipation are represented accurately.

The smaller the filter f_k, the finer the filtering, with $f_k = 1$ representing RANS and $f_k = 0$ representing DNS. The $f_k = 0.15$ provides the most accurate pressure forces calculation in a near wall region [47] and therefore was selected as the filter parameter.

According to Girimaji [39], for high Reynolds number flows in which dissipative scales are not resolved f_ε is specified as unity. Whereas for low Reynolds number flow in which there no

discernible separation of scales, using $f_k = f_\varepsilon$ provides better results. However, later it is claimed that this relationship may not hold for the near wall region and a separate analysis is required to confirm that.

Therefore to finalize the choice for f_ε a comparative analysis is done between $f_\varepsilon = 1$ and $f_\varepsilon = 0.15$ to select the more viable option. This is done by comparing the flow variables on the finest mesh of the validation case of a circular cylinder in crossflow. After the flow reached a statistically steady state, the flow variables were time-averaged over 10 periods of vortex shedding. The resulting flow variables are shown in Fig. 3.4.

The wake variables are compared at the distance of $x = 1.06D$ as shown in Figure 3.4. It is observed that for the model with $f_\varepsilon = 1$ is able to predict the streamwise velocity as function of distance from cylinder with greater accuracy than compared to $f_\varepsilon = 0.15$ where the error in the re circulation length calculation with respect to experimental value is larger. Moreover, other flow variables along the normal direction in the wake region of the cylinder along the center line experience large number of fluctuation even after extensive time-averaging. This inaccurate prediction of flow variables along the center line makes the model inaccurate.

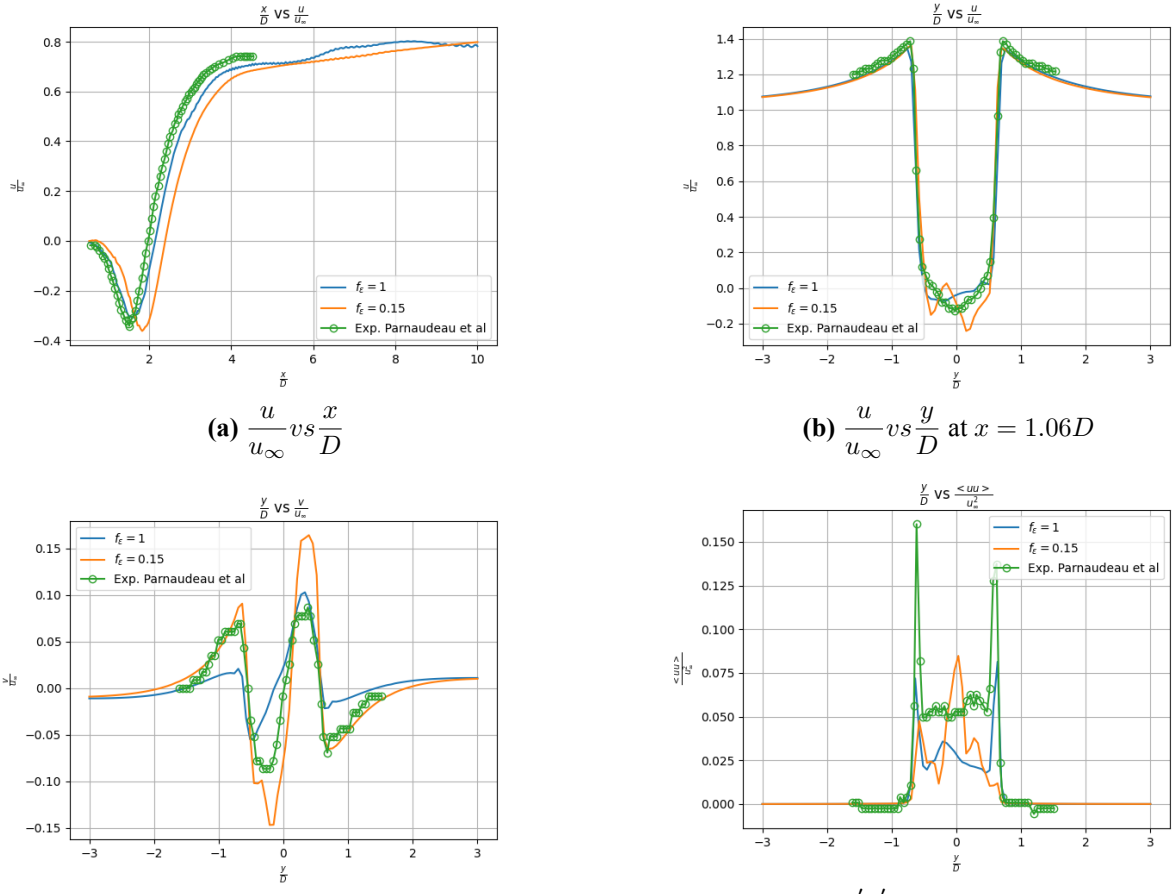

(a) $\frac{u}{u_\infty} vs \frac{x}{D}$ **(b)** $\frac{u}{u_\infty} vs \frac{y}{D}$ at $x = 1.06D$

(c) $\frac{v}{u_\infty} vs \frac{y}{D}$ at $x = 1.06D$ **(d)** $\frac{< u'u' >}{u_\infty^2} vs \frac{y}{D}$ at $x = 1.06D$

Figure 3.4: PANS filtering parameter Comparison

Based on these results, a conclusion can be drawn that $f_\varepsilon = 1$ provides better results in the

near-wall region. This might be due to the boundary layer effects in the near-wall region which requires a finer mesh for the dissipation rate filter to have such a small value.

3.4. Struct Epsilon (SE) Implementation

The Struct Epsilon (SE) model is a relatively new Struct model based on the non linear eddy viscosity model. So to implement that in OpenFOAM, LienCubicKE model is used as a base model. The LienCubicKE model is a cubic k-epsilon turbulence model that provides a foundation for capturing the effects of nonlinearity in turbulent flows. The Eddy Viscosity Equation is modified by updating the coefficients used in the stress strain relationship as derived by Baglietto, E. and Ninokata, H [48]. In this way, we can enhance the accuracy of the turbulence predictions in the context of the Struct Epsilon model. This approach enables us to leverage the established framework of the LienCubicKE model while incorporating the unique features of the Struct Epsilon model

The stress strain relationship in a Cubic $k-\varepsilon$ model is as in Equation 3.2 along with values of all the coefficients of the equation as derived by Baglietto, E. and Ninokata, H.

$$\begin{aligned}\rho\overline{u_i'u_j'} = &\frac{2}{3}\rho k\delta_{ij} - 2\mu_t S_{ij} + 4C_1\mu_t\frac{k}{\varepsilon}\left[S_{ik}S_{kj} - \frac{1}{3}\delta_{ij}S_{kl}S_{kl}\right] \\ &+ 4C_2\mu_t\frac{k}{\varepsilon}\left[\Omega_{ik}S_{kj} + \Omega_{jk}S_{ki}\right] + 4C_3\mu_t\frac{k}{\varepsilon}\left[\Omega_{ik}\Omega_{kj} - \frac{1}{3}\delta_{ij}\Omega_{lk}\Omega_{kl}\right] \\ &+ 8C_4\mu_t\frac{k^2}{\varepsilon^2}\left[S_{kl}\Omega_{lj} + S_{kj}\Omega_{li}\right]S_{kl} + 8C_5\mu_t\frac{k^2}{\varepsilon^2}\left[S_{kl}S_{kl} + \Omega_{kl}\Omega_{kl}\right]S_{ij}\end{aligned} \tag{3.2}$$

where

$$C_\mu = \frac{C_{a0}}{(C_{a1} + C_{a2}\bar{S} + C_{a3}\Omega)}$$

$$C_1 = \frac{C_{NL1}}{(C_{NL6} + C_{NL7}\bar{S})C_\mu} \tag{3.3}$$

$$C_2 = \frac{C_{NL2}}{(C_{NL6} + C_{NL7}\bar{S})C_\mu} \tag{3.4}$$

$$C_3 = \frac{C_{NL3}}{(C_{NL6} + C_{NL7}\bar{S})C_\mu} \tag{3.5}$$

$$C_4 = C_{NL4}C_\mu^2$$

and

$$C_5 = C_{NL5}C_\mu^2$$

The coefficients used for the Struct Model's version of stress strain equation are in Table 3.2.

Table 3.2: Stress- Strain Equation Coefficient

C_{a0}	C_{a1}	C_{a2}	C_{a3}	C_{NL1}	C_{NL2}	C_{NL3}	C_{NL4}	C_{NL5}	C_{NL6}	C_{NL7}
0.667	3.9	1	0	0.8	11.0	4.5	-5.0	-4.5	1000.0	1.0

Following this, the complete implementation requires the addition of the turbulent dissipation source term from (2.35) which has been done in Appendix A.1. The four models are run for the validation case in Section 3.1. The results from these cases are compared in Chapter 4.

4

Comparative Analysis

This chapter focuses on the numerical solution of the flow field over a circular cylinder for Re 3900 and comparison between the shortlisted hybrid models on the validation case in Section 3.1. The comparison between these turbulence models is conducted for different solution variables, comparing them for better precision and computational cost. The parameter selection is performed as in Section 4.1 followed by the comparison and selection of the most viable options for FSI in Chapter 5.

4.1. Comparison Parameters

As the flow is a low Reynolds number flow, it is laminar only in the boundary layer even near the wall. It becomes turbulent after separation in the wake of the cylinder. Moreover, for the FSI application the flow solution over the cylinder and the near-wall region is of concern. Therefore, the turbulence statistics were compared to literature just behind the cylinder at a distance of $\frac{x}{D} = 1.06$ after being sampled over 150 shedding periods after it reaches the statistically steady state at time t=2000. These statistics include the mean streamwise ($\frac{u}{u_\infty} vs \frac{y}{D}$ at x/D=1.06) and transverse flow velocity at different transverse locations of wake ($\frac{v}{u_\infty} vs \frac{y}{D}$ at x/D=1.06)and the mean resolved streamwise Reynolds stresses in different wake locations($\frac{< u\prime u\prime >}{u_\infty^2} vs \frac{y}{D}$).

The cylinder obstacle will force the mean streamwise velocity of the flow drop to 0 at the stagnation point on the cylinder's transverse face due to the cylinder's no slip boundary condition and in the turbulent wake beyond cylinder, the flow will also experience a region of reverse flow. These phenomena are assessed by comparing the mean flow in streamwise direction ($\frac{u}{u_\infty} vs \frac{x}{D}$ at y=0) with the available literature.

The final application for these hybrid models is to solve pressure forces in a FSI problem. Therefore, the lift and drag coefficients, the pressure distribution over the cylinder wall and the Strouhal number are considered as solution variables extremely relevant to this comparative analysis.

Finally, the objective is to determine the most efficient hybrid model so the precision of the results obtained and the computation cost to simulate it need to be optimized and all the results are compared for these 2 parameters.

4.2. Grid Study

This Section concerns the effect of grid size for different hybrid turbulence models. For this study, each model (SA-IDDES, SAS, PANS ad SE) is simulated for the mesh described in Table 3.1. These are then compared with the PIV experiments conducted by Parnaudeau et al. [49].

The different parameters selected in Section 4.1 are compared for the mesh sizes defined in Section 3.1 for all the models, as shown in Fig. 4.1-Fig. 4.4. As expected, the grid size has a relevant affect on all the models.

It must be noted that for SE, the finest mesh level has not been considered. This is because it is based on a cubic eddy viscosity model and convergence needs more iterations, especially for the pressure equation, as was observed during simulation. Additionally, the higher-order terms also attribute to the higher sensitivity of the model to smaller scales while working with the refined mesh. Different solvers and convergence settings were tested to overcome this issue. All these issues lead to a large increase in simulation time.

Considering the computational expense and timeline of the thesis, along with the research objective to find the most efficient hybrid option, the simulation of SE on finest A8 mesh was removed from the scope of this study.

It can be observed from Fig. 4.1a - Fig. 4.4a, the mean flow is zero at the base due to the no-slip boundary condition over the cylinder and then it becomes negative due to the turbulent wake region after separation, followed by an asymptotic increase to free-stream velocity. The streamwise re-circulation length (L_r) is defined as the distance from the base of the cylinder where the mean flow velocity is zero to the distance where the flow becomes positive again.

For all the models it is evident that mesh refinement plays a crucial role in calculating this re-circulation length. However, the sensitivity reduces with refinement in mesh size with minimal difference in approximation for A6 and A8. This trend is consistent for all the turbulence models considered here,with the exception of SE as the finest mesh encountered a stability issue for it.

The other mean flow parameters also show similar grid sensitivity for all the models as can be observed in Figs. 4.1b to 4.1d - Figs. 4.4b to 4.4d. It was also observed that these models tend to over-predict the Reynolds stress on coarser grids and SE has the least sensitivity when the wake region flow variables are considered.

Next, the mesh sensitivity of the models in calculation of forces by comparing the time averaged pressure distribution with respect to angle (θ),in Figs. 4.1e, 4.2e, 4.3e and 4.4e, which represents the circumferential position of a point on the surface of the cylinder, measured from the front stagnation point in the direction of the flow. It is the angle between the line extending from the center of the cylinder to the point in question and the line extending from the center to the front stagnation point, measured in the direction of the flow. The spectral analysis of the forces in streamwise and transverse direction is shown in Figs. 4.1f, 4.2f, 4.3f and 4.4f respectively.

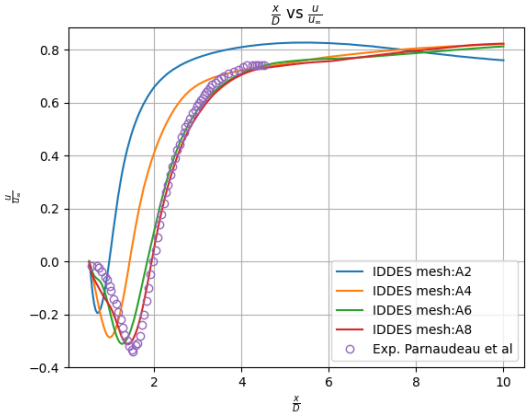

(a) Mean flow in Streamwise direction ($\frac{u}{u_\infty}$ vs $\frac{x}{D}$)

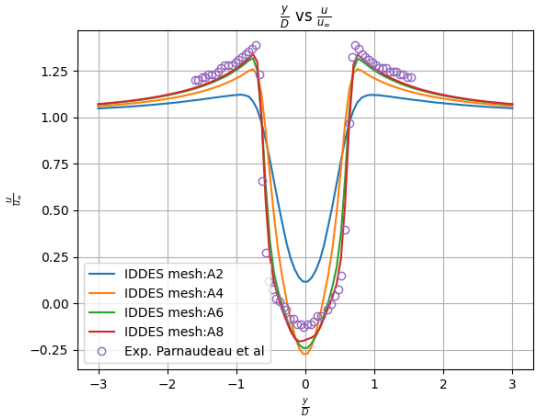

(b) Mean flow in Streamwise direction in different wake regions ($\frac{u}{u_\infty}$ vs $\frac{y}{D}$)

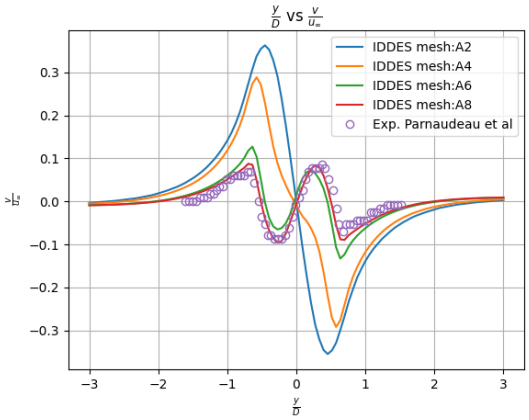

(c) Mean flow in transverse direction at x/D=1.06 ($\frac{v}{u_\infty}$ vs $\frac{y}{D}$)

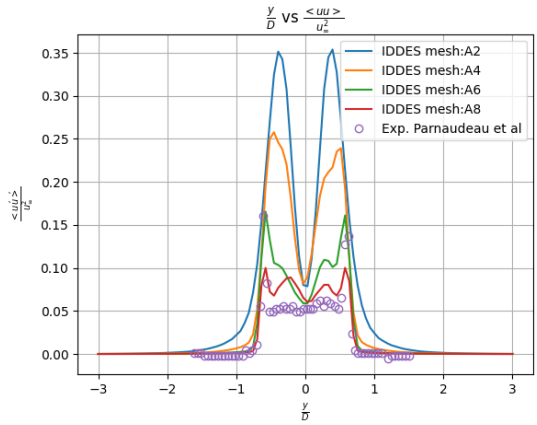

(d) Mean resolved streamwise Reynolds stresses at x/D=1.06 ($\frac{< u'u' >}{u_\infty^2}$ vs $\frac{y}{D}$)

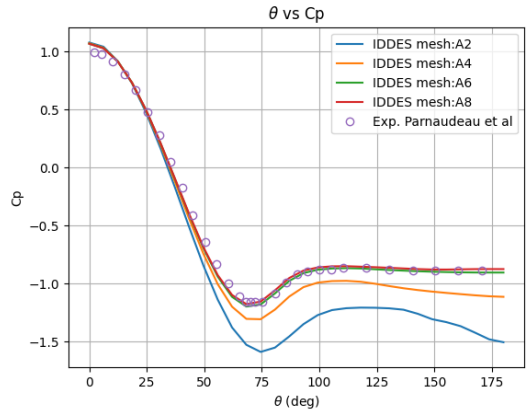

(e) Pressure Coefficient over cylinder ($C_p vs \theta$)

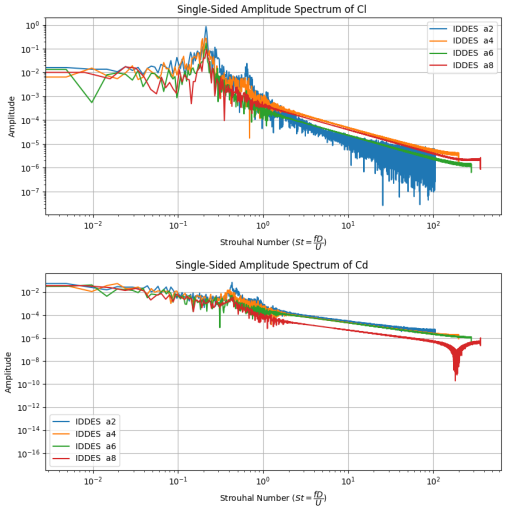

(f) Spectral Analysis for C_L and C_D

Figure 4.1: Comparison Variables for IDDES over different Mesh Size

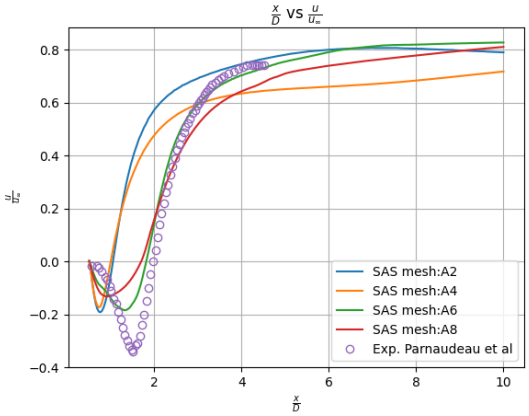

(a) Mean flow in Streamwise direction ($\frac{u}{u_\infty}$ vs $\frac{x}{D}$)

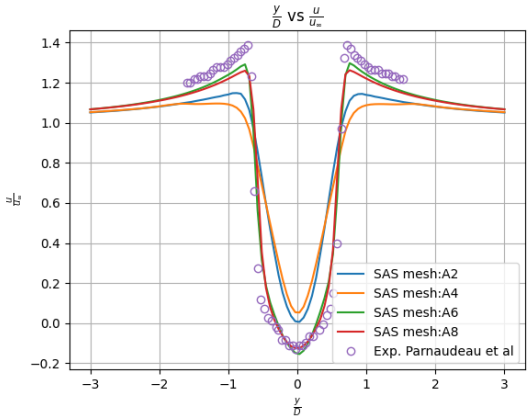

(b) Mean flow in Streamwise direction in different wake regions ($\frac{u}{u_\infty}$ vs $\frac{y}{D}$)

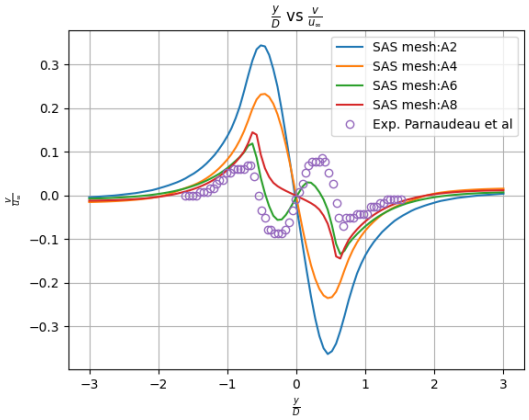

(c) Mean flow in transverse direction at x/D=1.06 ($\frac{v}{u_\infty}$ vs $\frac{y}{D}$)

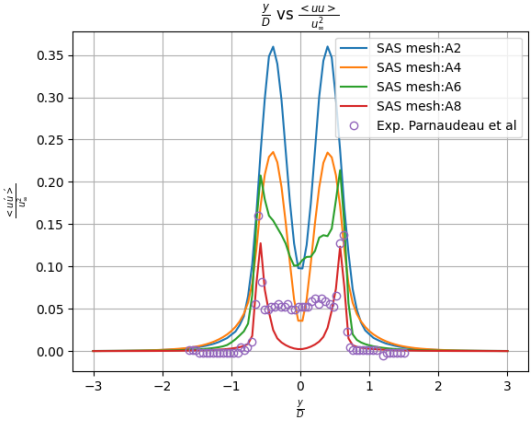

(d) Mean resolved streamwise Reynolds stresses at x/D=1.06 ($\frac{< u'u' >}{u_\infty^2}$ vs $\frac{y}{D}$)

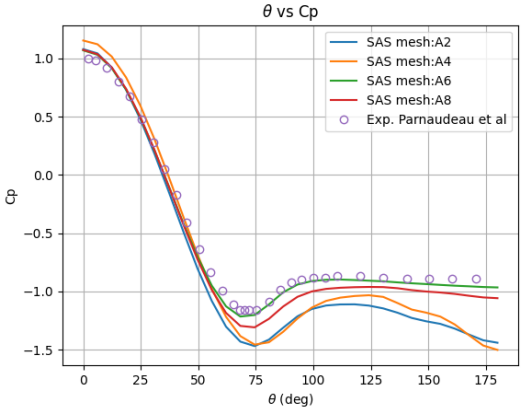

(e) Pressure Coefficient over cylinder ($C_p vs \theta$)

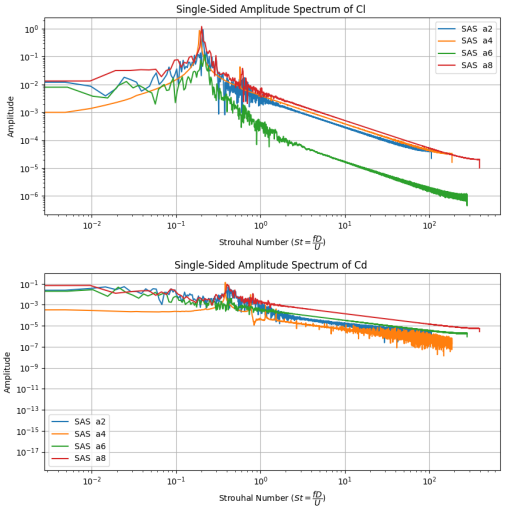

(f) Spectral Analysis for C_L and C_D

Figure 4.2: Comparison Variables for SAS over different Mesh Size

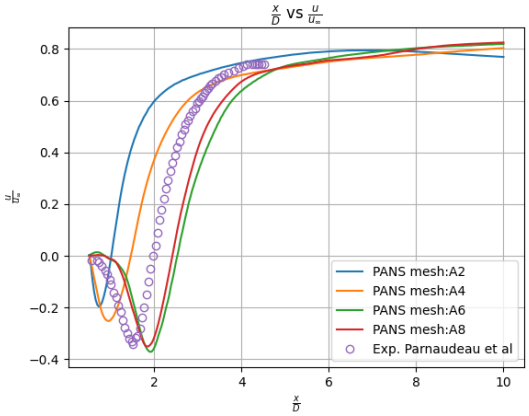

(a) Mean flow in Streamwise direction ($\frac{u}{u_\infty}$ vs $\frac{x}{D}$)

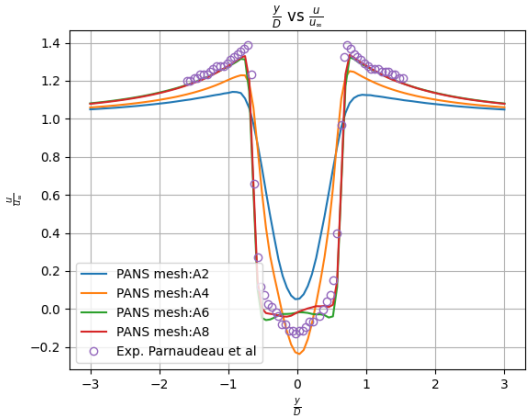

(b) Mean flow in Streamwise direction in different wake regions ($\frac{u}{u_\infty}$ vs $\frac{y}{D}$)

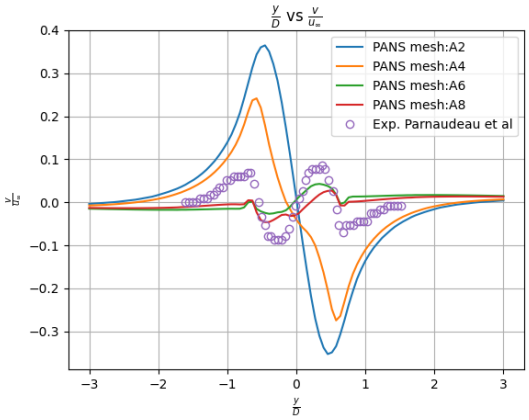

(c) Mean flow in transverse direction at x/D=1.06 ($\frac{v}{u_\infty}$ vs $\frac{y}{D}$)

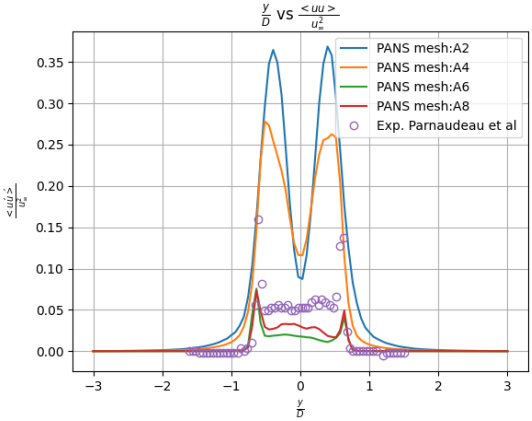

(d) Mean resolved streamwise Reynolds stresses at x/D=1.06 ($\frac{< u'u' >}{u_\infty^2}$ vs $\frac{y}{D}$)

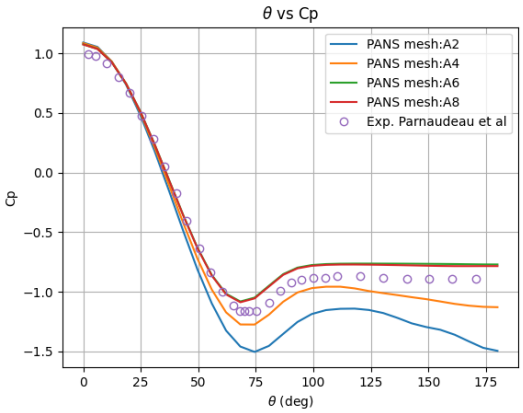

(e) Pressure Coefficient over cylinder ($C_p vs \theta$)

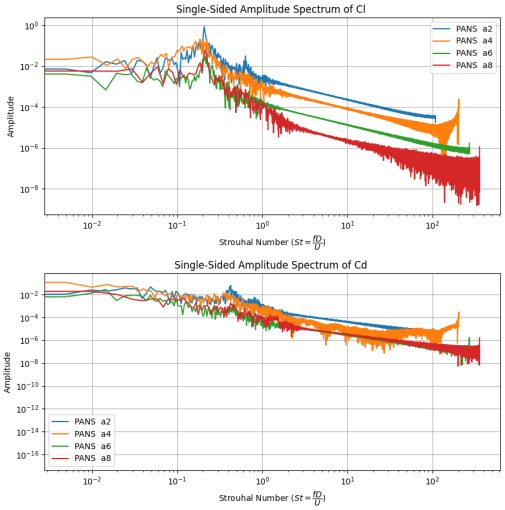

(f) Spectral Analysis for C_L and C_D

Figure 4.3: Comparison Variables for PANS over different Mesh Size

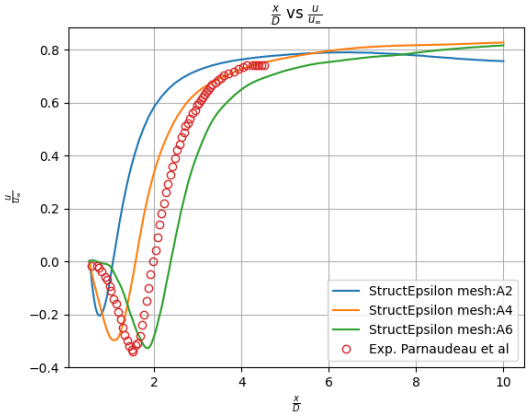

(a) Mean flow in Streamwise direction ($\frac{u}{u_\infty}$ vs $\frac{x}{D}$)

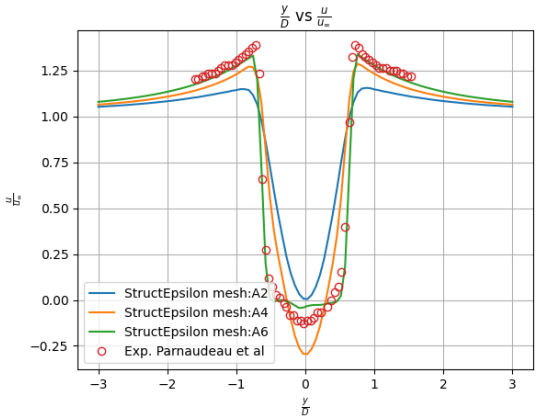

(b) Mean flow in Streamwise direction in different wake regions ($\frac{u}{u_\infty}$ vs $\frac{y}{D}$)

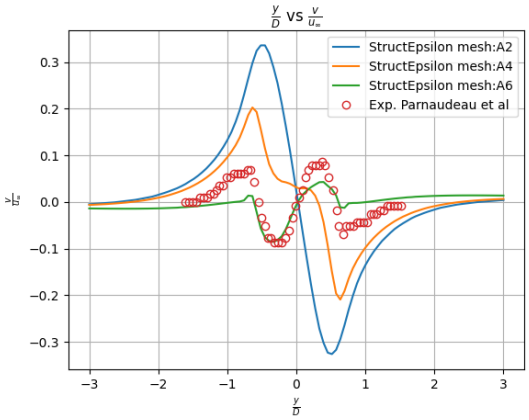

(c) Mean flow in transverse direction at x/D=1.06 ($\frac{v}{u_\infty}$ vs $\frac{y}{D}$)

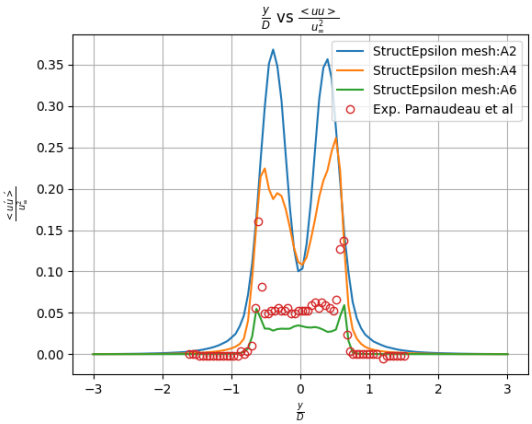

(d) Mean resolved streamwise Reynoldss stresses in different wake locations ($\frac{<u'u'>}{u_\infty^2}$ vs $\frac{y}{D}$)

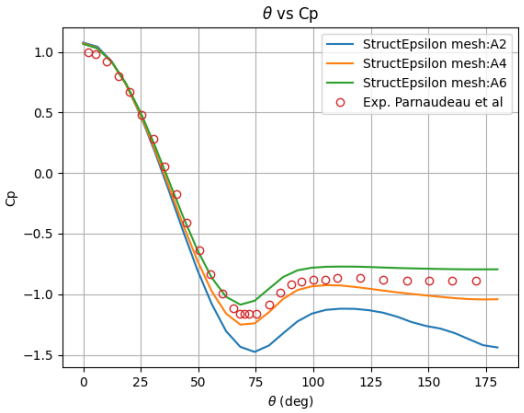

(e) Pressure Coefficient over cylinder ($C_p vs \theta$)

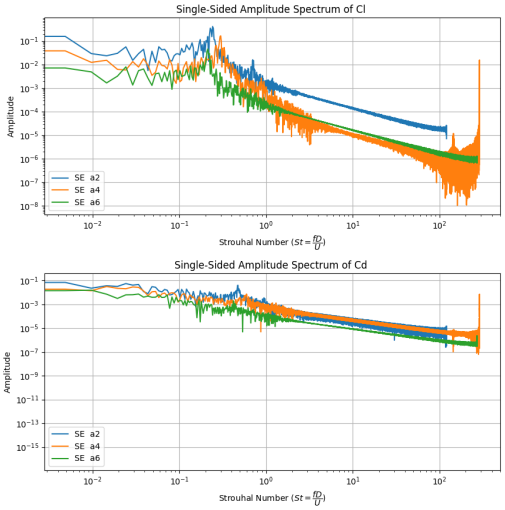

(f) Spectral Analysis for C_L and C_D

Figure 4.4: Comparison Variables for SE over different Mesh Size

While the general trend remains mostly consistent with the error and the sensitivity decreasing with the refinement of the mesh, an anomaly is observed with the pressure distribution for the SAS model in Fig. 4.2e. Here it is observed that for a refined mesh, the force calculations become inaccurate after the separation point. Further discussion on this is done in Section 4.3.

The refinement of mesh contributes to better results for almost all models with exception to SAS. Even though the trend is consistent the reason behind it is explained differently for each model. For IDDES, as the mesh is refined the zone segregation between RANS and LES occurs more precisely after the boundary layer. Moreover, refinement means that the LES model is able to resolve smaller scales.

In the PANS model the grid resolution needs to be adequate to capture the fluctuations liberated by the model. Since the filter parameters selected in this implementation of PANS is kept constant, therefore the more refined the mesh is, more suitable for the selected filter parameters it becomes. The result of this fact is directly visible in Fig. 4.3.

The SE model is not directly dependent on grid size but reducing the grid size means decrease in error in calculation of Q criteria and thus provide a better evaluation of the source term proving more precise eddy viscosity value in the transport equation. This ultimately results in better modeling of the turbulence.

The SAS anomaly has been difficult to explain. Its poor performance in solving flow statistics in comparison to other models specially on the finest mesh can be rooted to its conservative nature that avoids switching from RANS to LES. This leads to insufficient resolving of scales and thus the inaccuracy. The model calculates the circulation length but isn't able to correctly measure the wake velocity. However the model experiences a divergence while solving the pressure equations. Further flow visualization of flow on this divergence and the increasing error on finest mesh size is conducted in Appendix B.

Finally, the spectral analysis of Cl and Cd for different grid sizes gives a clear picture of each model's ability to resolve small scales. While a general trend of improvement in resolution is seen in each model with mesh refinement, it is also observed that SE has a larger frequency range in the spectral analysis suggests that the model can resolve finer (smaller) scales of turbulence. This means it is capable of capturing more detailed fluctuations and smaller eddies within the turbulent flow. This proves the higher fidelity of SE on a coarser mesh as compared to other hybrid models.

Based on the grid study, it can be observed that although the number of cells increases by a factor of approximately 3 between the A6 and A8 mesh levels, there is not a significant difference in the flow solution for both the IDDES and PANS models. However for SAS the difference increases on A8. This means that the grid independence can be considered to be achieved beyond A6 for IDDES and PANS, but not for SAS. In the next Section a comparison between different turbulence models on their respective finest scale , that is A8 for IDDES, SAS and PANS and A6 for SE, is done to compare the precision at solving the flow and the corresponding computational time to find most efficient and precise options to proceed further with.

4.3. Hybrid Model Comparison

This Section compares the different models for comparison parameters defined in Section 4.1 along with Strouhal number and computation time. The RMSE of these variables with respect to mesh sizes is also evaluated to check convergence of the models. Based on these observation, models are selected as most feasible options to implement FSI.

4.3.1. Comparison Variables in wake region

The mean flow variables are compared in the near wall wake region to the available experimental data as the accuracy of flow variable calculation in this region is an extremely important parameter for model selection. This is because the mesh motion occurs in this region when the moving cylinder case for FSI implementation is considered in Chapter 5 so the turbulence model should be able to solve the transport equations precisely in this region to minimize error propagation in a dynamic mesh case. Additionally, the root mean square error convergence graph for the models were compared to assess the accuracy and stability of each model in capturing the flow dynamics.

The streamwise velocity plots in Fig. 4.5 shows that almost all the models are able to predict the streamwise velocity profile for their respective finest mesh with an exception of SAS, which is able to predict the L_r but not the recirculation velocity magnitude. PANS even on the finest mesh tend to overshoot the wake region. SE also displays a similar overshoot in the A6 mesh simulation as can be seen in the plot.

All the models show a error convergence with grid refinement, that is the Root Mean Square Error (RMSE) of calculating the profile with respect to the average flow reduces with a higher resolution grid. The RMSE is defined in (4.1) ,where u_{ex} is the exact value of a variable u, usually taken from experimental data and u_{sim} is the numerically solved value,.

$$RMSE = \sqrt{(u_{ex} - u_{sim})^2} \tag{4.1}$$

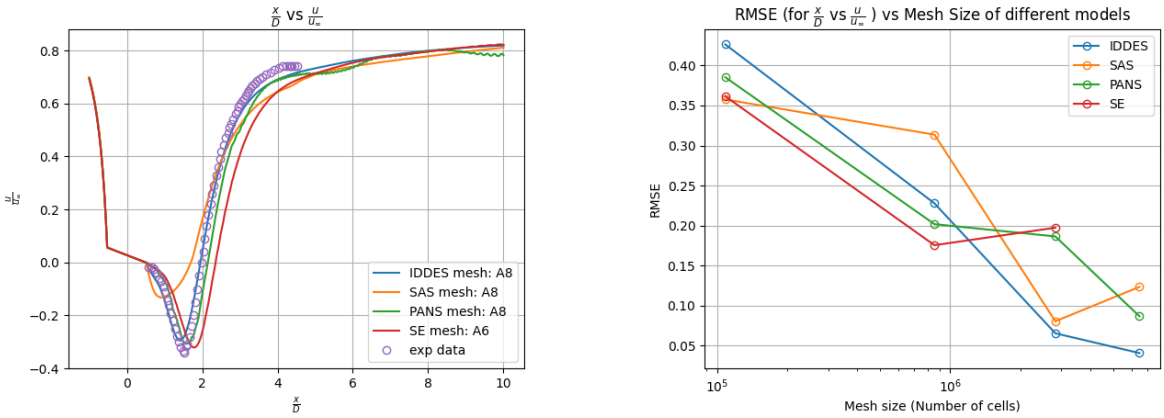

(a) Mean velocity in Streamwise direction

(b) RMSE with respect to Mesh Size

Figure 4.5: Mean velocity in Streamwise direction,
(o exp data - Parnaudeau et al.)[49]

The streamwise flow in transverse direction plots Fig. 4.6 reveal a limitation of the PANS and SE

model as they are not able to solve for the streamwise flow near the centerline. This can be due to the model filter parameters as has been discussed in Section 3.3 and possibly more fine tuning of the parameters are required to capture the exact distribution of streamwise velocity near centerline. The RMSE plot in Fig. 4.6b shows that SE is proving comparable results to IDDES even on a level coarser grid with a difference in error percentage by 2 %. For SAS the error increases for the finest grid.

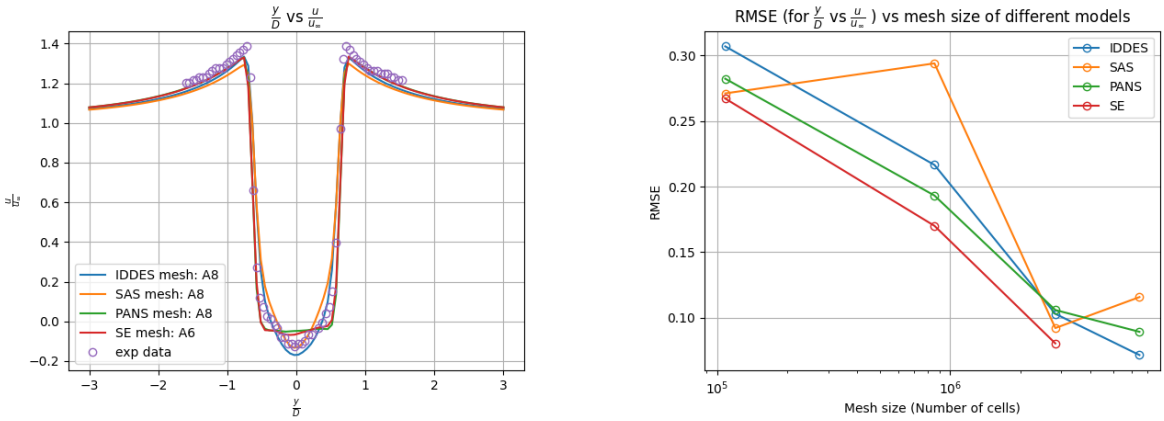

(a) Mean flow in Transverse Direction

(b) RMSE with respect to Mesh Size

Figure 4.6: Mean Streamwise velocity in Transverse direction, (o exp data - Parnaudeau et al.)[49]

The mean transverse velocity in transverse direction at x= 1.06D, shown in Fig. 4.7 is a crucial parameter in turbulence model selection. As discussed before, in FSI case, the turbulence model must be able to accurately resolve velocity components in region where mesh deformation occurs. In the case of a dynamic body, domain deformation can occur along the transverse direction due to the structure movement and/or deformation. The RMSE plot indicates that the IDDES model has the least error percentage with respect to the experimental data and provides most accurate transverse velocity calculation.

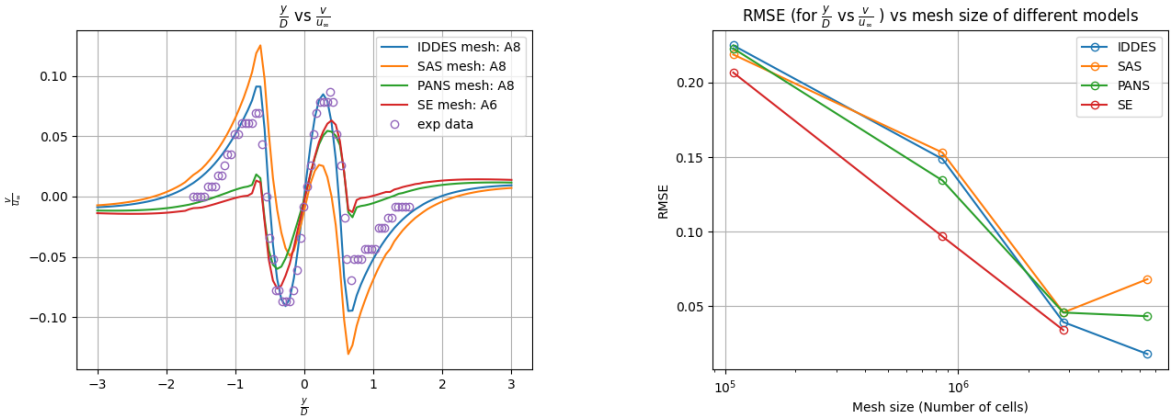

(a) Mean transverse flow in transverse direction

(b) RMSE with respect to Mesh Size

Figure 4.7: Mean transverse velocity in transverse direction,
(o exp data - Parnaudeau et al.)[49]

The mean resolved reynolds stress in transverse direction at x=1.06D in Fig. 4.8 show that while SAS provides most accurate calculation of both stress peaks, it over-predicts the stress in the entire near wall region while PANS and SE do not. This provides a proof of viability of PANS and SE over the SAS.

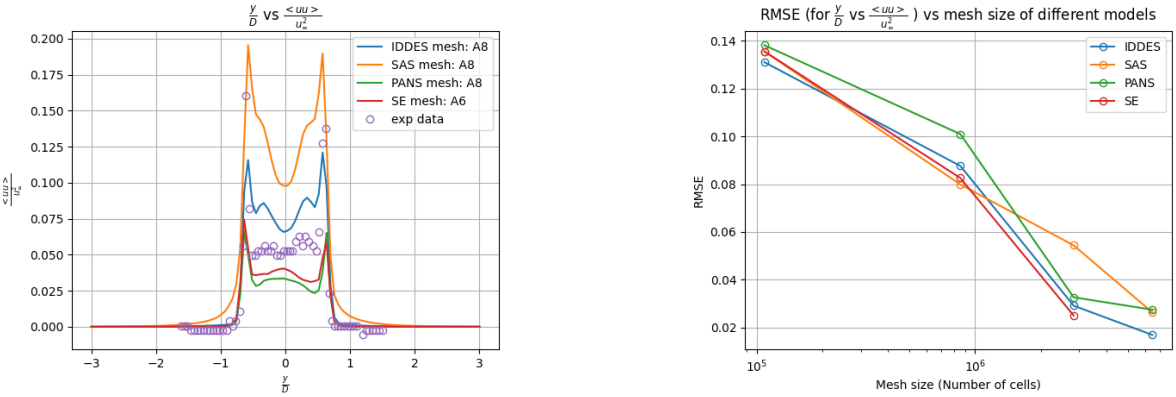

(a) Mean Resolved Reynolds Stress ($\frac{< uu >}{u_\infty^2}$ vs $\frac{y}{D}$)

(b) RMSE with respect to Mesh Size

Figure 4.8: Mean flow in Streamwise direction,
(o exp data - Parnaudeau et al.)[49]

4.3.2. Comparison Parameters calculated over cylinder Surface:

This Section compares compares the accuracy of the boundary layer solution near the cylinder wall, for the four different hybrid turbulence models. For FSI application, the CFD part of the solver is used to provide the pressure forces acting on the interface. Therefore the parameters discussed in this Section will be the primary factors determining the final selection.

The SAS model has been showing anomalous behavior compared to other models but the pressure distribution curve in Fig. 4.9a provides insight into this. It under-predicts the pressure beyond

separation point becoming the most inaccurate among the four options. The Fig. 4.9b shows the anomalous behavior of SAS where error increases with grid refinement.

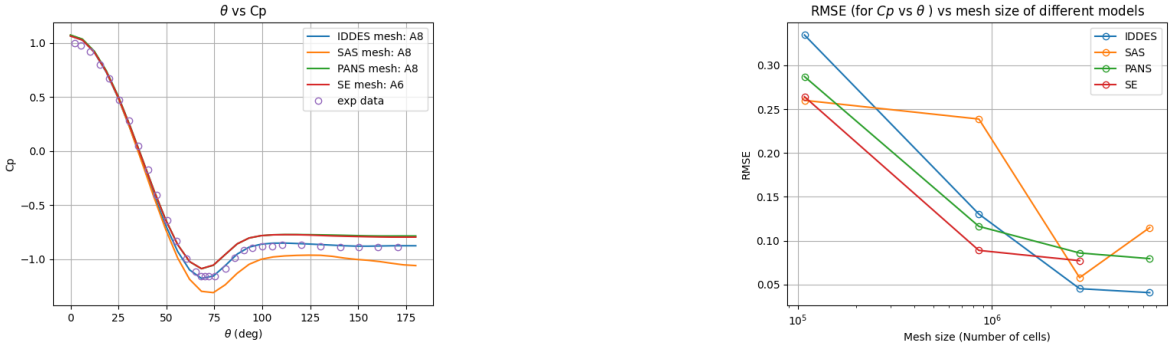

(a) Pressure Distribution over surface

(b) RMSE with respect to Mesh Size

Figure 4.9: Pressure Distribution over cylinder
(o exp data - Lourenco et al.)[50]

The force coefficient as in Fig. 4.10 is also an important parameter from an FSI point of view. The SAS model displays very high amplitude of oscillations for the Cl and Cd time history similar to a RANS model in [50]. This behavior similar to RANS brings the question if at the finest mesh, SAS is functioning in RANS mode with Q_{SAS} =0.

According to Lourenco et al [50], for the flow over a circular cylinder at Reynolds 3900, mean C_L $(\bar{C_L}) = 0$ and mean C_D $(\bar{C_D}) = 0.99$. The SAS model displays very high amplitude of oscillations for the Cl and Cd time history similar to a RANS model. This be It also experiences a divergence after All three remaining models demonstrate similar precision in determining the force coefficients for mesh A6, with improvements observed for both IDDES and PANS as mesh refinement is applied.

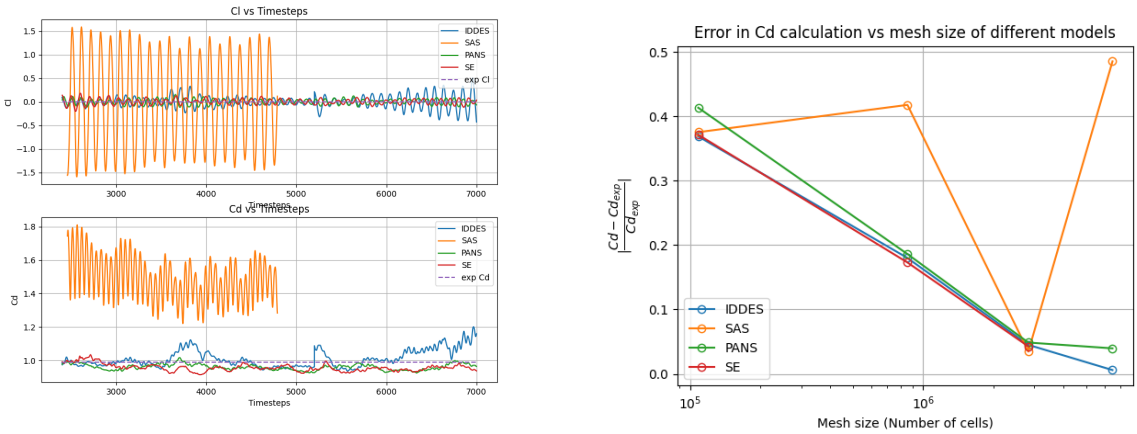

(a) Force Coefficients Time History

(b) RMSE C_D with respect to Mesh Size

Figure 4.10: Force Coefficients

The next important step is determining the Strouhal Number which has been discussed in Chapter 2.

The power spectrum of the vortex shedding frequency is obtained by performing the Fourier transform (FFT) of the lift coefficient history time curve, which is presented in Fig. 4.11a. From this analysis, the vortex shedding frequency f_n and the Strouhal number St can be calculated. The calculated Strouhal number for fines grid of each turbulence model is in Table 4.1.

Table 4.1: Strouhal Number for different turbulence model

MODEL	ST NUMBER
EXP*	0.215
IDDES	0.2135
SAS	0.2008
PANS	0.2158
SE	0.2132

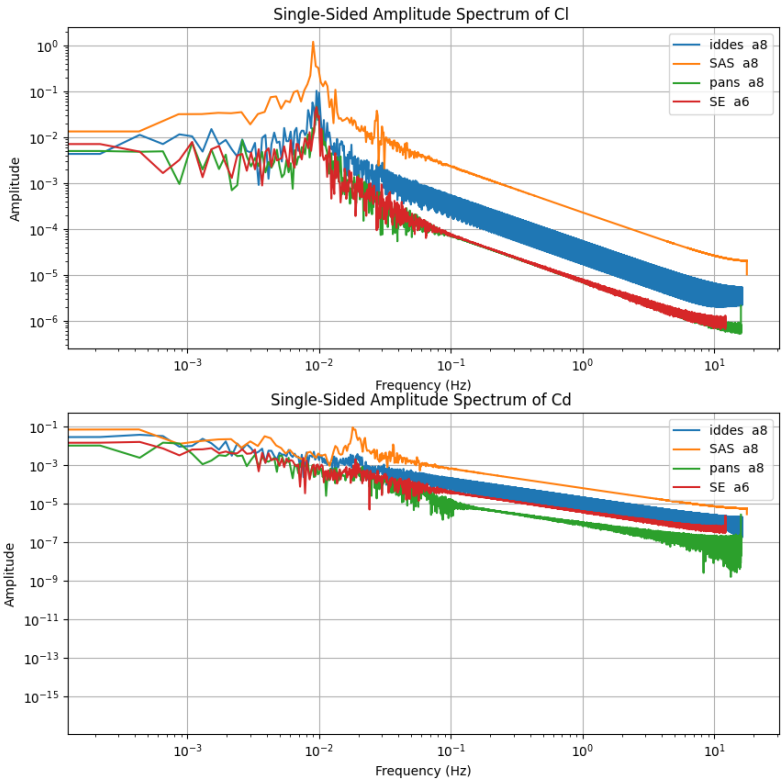

(a) Spectral Analysis

Figure 4.11: Strouhal Number from spectral analysis of Lift Time History

To evaluate the computation cost other parameters like solvers, schemes and number of parallel decomposition regions, which is 64, are kept constant. The computation time as in Fig. 4.12

shows a simple trend in computation cost. The SE is the least expensive followed by PANS and IDDES while SAS is the most computationally expensive turbulence model for all grid scales.

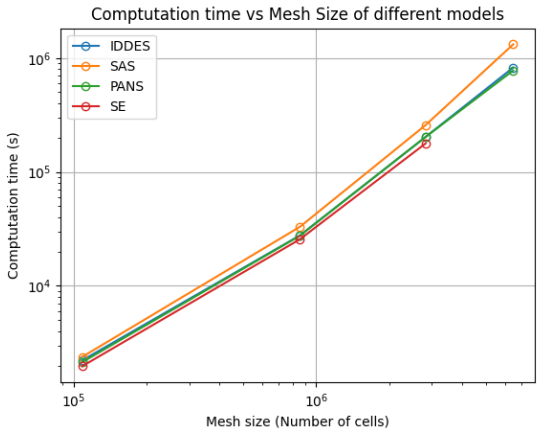

Figure 4.12: Computation Time

The vortex structures resolved by each model are also compared.Fig. 4.13 shows the three dimensional vortex structures in the wake region identified by the Q criterion value $Q = 0.5 \times U_\infty^2/D^2$, with the isosurface colored by the magnitude of the normalized velocity. The comparative analysis reveals that IDDES, SE and PANS are able to effectively capture the vortex structures in the wake region. However, the SAS model struggles to resolve the smaller scales of these vortex structures. Among the four models, SE seems to be better at resolving smaller scales as compared to the other models.

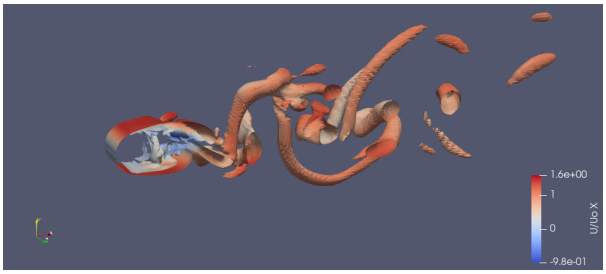

(a) SA-IDDES

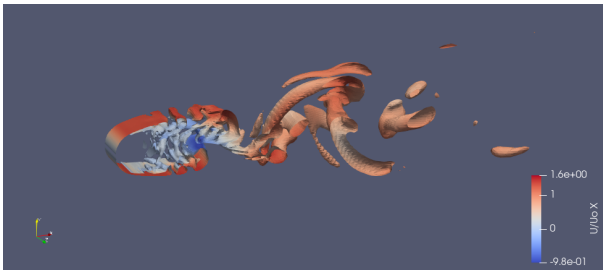

(b) PANS

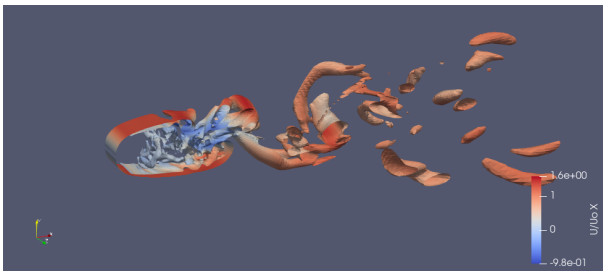

(c) SE

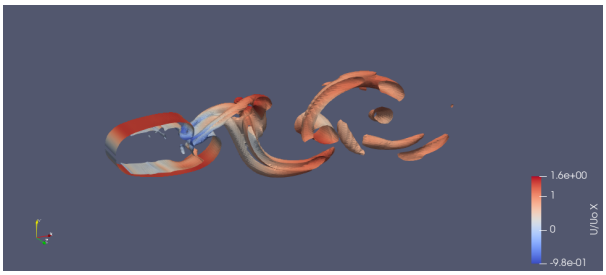

(d) SAS

Figure 4.13: Instantaneous view of coherent vortex structures contoured for Mesh A6

Fig. 4.14 shows the contour of the instantaneous vorticity of the flow past the cylinder in the horizontal plane. The development of the shear layer over the wall is very sensitive to external

influences. Small disturbances can easily cause early separation of the boundary layer thus making the shear layer shorter which effects the calculation in the wake region of the flow field. The comparison is done between IDDES, SAS and PANS cases on mesh A8 with SE on mesh A6. In this comparison the SE model seem to have the longest shear layer. It is also observed that different model are able to resolve different sizes of eddies. The PANS model followed by IDDES and SE are able to resolve smaller eddies as well in comparison to SAS model.

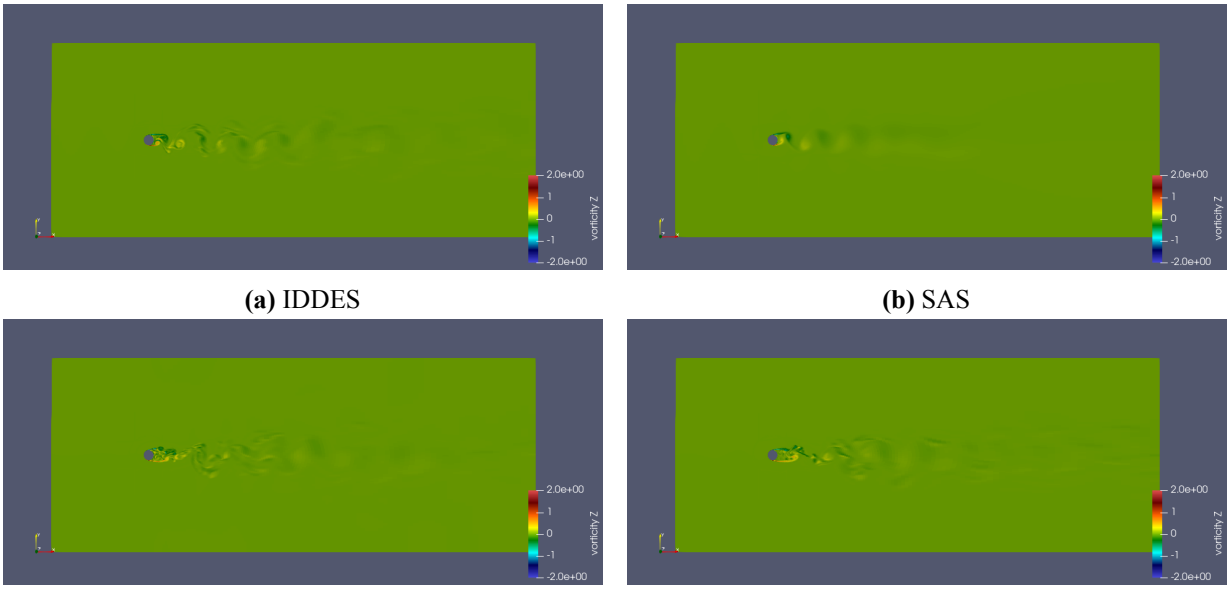

(a) IDDES **(b)** SAS

(c) PANS **(d)** SE

Figure 4.14: Isocontour maps of vorticity for the flow past a cylinder in horizontal plane z/D = 0

4.4. Discussion and Hybrid Model Selection for FSI:

The comparison in Section 4.3 offers an in-depth analysis of model performance across various parameters, providing a detailed illustration of each model's capabilities. The primary goal of this analysis is to determine the most efficient options for turbulence modeling. To this end, the Improved Delayed Detached Eddy Simulation (IDDES) and SE models have been selected for further consideration.

The SE is particularly noted for its computational efficiency. SE delivers results that are comparable to more complex models, yet it operates effectively on a coarser mesh. This characteristic significantly reduces computational time and resources, which is a critical advantage in many practical applications. By maintaining a balance between computational demand and result accuracy, SE emerges as an optimal choice for scenarios where resource constraints are a major concern.

On the other hand, the Partially-Averaged Navier-Stokes (PANS) model presents a competitive performance, making the selection process between PANS and IDDES challenging. PANS is capable of delivering high-quality results, and it shares many attributes with IDDES, especially in terms of resolving turbulent structures. However, the critical distinction lies in IDDES's superior ability to accurately resolve mean-flow variables in the wake region. This precision is particularly

vital for applications requiring detailed wake predictions, thus giving IDDES a slight edge over PANS. Additionally, for PANS there is a need for the user to determine the filter parameter as per the requirement. This reduces the ease to use and thus makes PANS less desirable in comparison to its counters like IDDES.

IDDES stands out due to its exemplary performance with highly resolved meshes. When compared to other models, IDDES demonstrates superior accuracy, especially in finely meshed simulations. The ability of this model to capture detailed turbulent flow characteristics with high fidelity makes it the preferred choice for rigorous turbulence modeling. The precise accuracy of IDDES in predicting both boundary layer and wake flow reinforces its selection as a leading model for detailed simulation work.

The SAS model, in contrast, was readily excluded from further consideration. SAS struggles to accurately resolve forces over surfaces beyond the separation point. It shows a error divergence when run with finest mesh A8 and exhibited RANS like results for force calculation. Consequently, SAS was discarded in favor of models that offer more robust and reliable performance in those areas.

In summary, the comprehensive comparison highlights the strengths of IDDES in achieving high-resolution accuracy and precise wake flow predictions, alongside the computational efficiency of SE for less demanding mesh resolutions. The detailed assessment and subsequent selection of these models are justified by their ability to meet the dual criteria of accuracy and computational efficiency, thereby ensuring robust and effective turbulence modeling for a wide range of applications.

Chapter 5 evaluates the 2 selected models and validate them for a simple FSI test case.

5

Validation on FSI Case

After shortlisting the hybrid turbulence model based on most accurate and fastest model with least computation time, these models are validated and compared on a FSI problem

5.1. Validation Case

A simple oscillation due to the vortex-induced vibration case was considered. Khalak and Williamson [51] a pioneer work from 1996 determined the effect of mass damping parameters for vortex-induced vibration of a 1 degree of freedom elastically mounted rigid cylinder. It is noticed that the vibration amplitude response is divided into two sub-branches of resonant response, the upper and the lower branch. Their work is used as a reference for the results and comparison with experimental data for amplitude response.

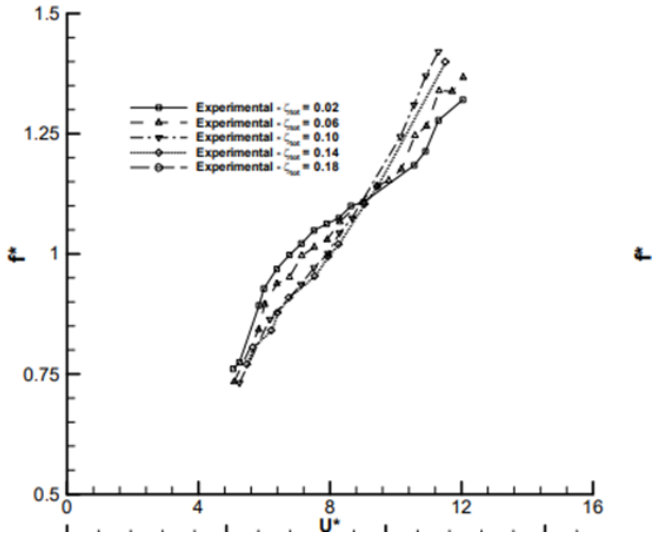

Figure 5.1: Frequency Response from Lee et al. at different damping ratios

For the frequency response curve, experimental data from Lee et al. [52] is used as a reference point. However, Lee's work evaluates the frequency response at a slightly different damping of 0.02 instead of 0.013 as done in the experimental reference of Khalak et al. and in this

simulation. These results are still considered as reference because when the frequency plot at different damping ratios in the reference, as shown in Fig. 5.1, is considered, it is observed that damping ratio has a small impact on the range of frequency response f^* value. This effect is considered to be negligible in this validation and the frequency response is done somewhat qualitatively to compare hybrid models to RANS. The work of Guilmineau et al.[53] that has implemented the $k-\omega SST$ model is also used as a comparison with the URANS-based turbulence models. The work of Muaaz [54] is used for comparison with the RANS model such as cubic $k-\varepsilon$.

5.1.1. Simulation Setup

Experimental results [51] are used as a reference point for the simulation. the mass ratio, damping parameter and other properties of the cylinder are chosen to be the same as in the reference. These are explained in Table 5.1. The case is simulated over a range of Reynold's number by selecting non-dimensionalized velocity ratios (U^*) as in the references. This helps in finding the natural frequency of the cylinder in the air which allows the selection of the cylinder mass spring stiffness and damping.

Table 5.1: Test Case Defining Parameters

Case Setup Parameters	**Value**	**Units**
Cylinder Diameter, (D)	0.0381	m
Mass Ratio (m*)	2.4	
Mass Damping (m*ζ)	0.013	
Cylinder's Natural Frequency in air ($f_{n_{air}}$)	0.532	Hz
Fluid Density (ρ)	997.561	kg/m3
Dynamic Viscosity (μ)	8.89 $\times 10^{-4}$	Pa. s

The hybrid turbulence models IDDES and SE have been shortlisted in Chapter 4. In this Section these two models are used to simulate this FSI case on different mesh sizes as explained in Table 5.2. This simulation is performed on different velocities ratios $U^* = \dfrac{U}{f_{n_{air}} D}$ at values U^* = 5.73 and U^* = 4.5. Finally, additional cases of U^* = 7, 9, 10.75 and 12.5 are tested on a coarser mesh of level A4 to evaluate the frequency and amplitude response curve trends. The SE model is not implemented for most refined level. The reasoning behind this is as discussed in Chapter 4

Table 5.2: Mesh levels for FSI case
* not applicable for SE model

Mesh level	n_θ (44*A)	n_z (6*A)	n_{cells}	n_{xy}
A2	88	12	108456	9038
A4	176	24	856920	35705
A6	264	36	2828268	78563
A8*	352	48	6495120	135315

The domain is defined as a cuboid with the cylinder being placed at a distance of 10D from the inlet. The outlet is described at a distance of 40D from the cylinder. The lateral clearance of 10D is also provided to the cylinder, a no-slip boundary condition is given to the cylinder's wall when this cylinder is in static condition. The fix velocity inlet is used with the velocity corresponding to the selected U^* value. A zero gradient pressure outlet boundary condition is implemented along with a spanwise cyclic boundary condition. The upper and lower wall is given a symmetry plane boundary condition. The final domain is as in Fig. 5.2 which is designed and meshed same as the test case from Chapter 4 but is scaled down to D=0.0381 m.

The simulation is run for the fixed cylinder till the steady state is achieved. Once the steady state is achieved the cylinder is released to have a degree of freedom along y axis. The boundary condition over the cylinder wall is then modified to a moving wall boundary condition.

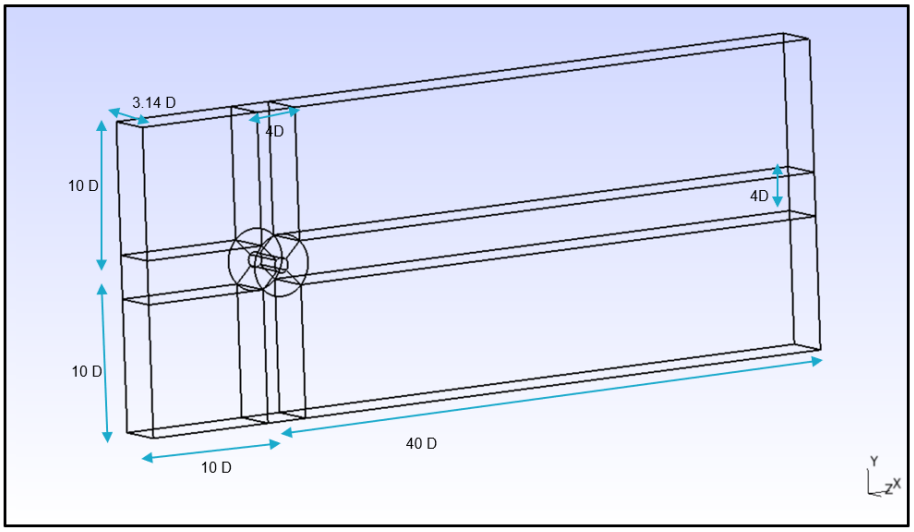

Figure 5.2: FSI case Domain

5.2. OpenFoam Implementation

5.2.1. SiX DOF Rigid Body Solver

The sixdofrigidbodymotion solver of OpenFOAM is implemented for the FSI application over the selected test case. The inverse quadratic mesh morphing methodology is used for the mesh

morphing with a morphing distance of from 0 to up till 2.5D distance from the cylinder wall as can be visualized in Fig. 5.3.

The motion of the moving wall is constrained using the orientation constraint to resist the rotational degree of freedom. Along with that, the translation motion is constrained to the direction normal to the cylindrical span along the y axis using the line constraint.

Restraints are used to define the forces acting on the moving wall. The linear spring restraint is used to define the oscillatory motion in the transverse (Y) direction by defining the damping coefficient and the stiffness based on the natural frequency of the cylinder in air.

Finally, the dynamic mesh solver selection is done between Newmark ,which is a second order implicit solver, and Symplectic which is a second order explicit solver. Even though according to Chennakesava et al. [55], when compared for oscillating cylinder with laminar turbulent model in openFoam and for zero damping, Symplectic solver provides more precise result, for this case the solution diverged.

This divergence is possibly due to the inner iterations done by pimpleFoam due to the correcter implemented within it. The Symplectic solver is incompatible with the implementation of additional corrector that lead to iterations within a timestep. Therefore Newmark solver was selected.

Figure 5.3: Morphing Region

5.3. Results and Discussion

In this Section, the results are analyzed, and the comparison between different hybrid turbulence models is made. The models are compared to each other on the basis of the Cl time history results, the maximum displacement of the cylinder and the frequency of the oscillation. Finally, they are compared on the basis of computational efficiency, which is estimated using the error in calculating the maximum displacement versus the computational time relation on different mesh sizes.

The experimental results for displacement curve from Khalak et al. [51] and frequency response from Lee are used for comparison purposes. Since the results for frequency response for $\zeta = 0.013$ are not available, the closest possible results from Lee et al. at $\zeta = 0.02$ were used.

The simulation is initially run for U^* = 5.73 and U^* = 4.5 which correspond to to the peak point of the amplitude response curve's upper branch and the starting region of the upper branch. The results for them are discussed in Section 5.4 and Section 5.5 respectively.

5.4. U* = 5.73

The cohrent vortex structures at a given time instant t=100s for $U^* = 5.73$ in Fig. 5.4. As it is evident from the figure due to the oscillation of the cylinder in transverse direction, the vortex structures are also showing a sort of oscillatory behavior. For both the cases Mesh A6 is compared. It's observed that the SE model plot has small scales as compared to the IDDES . This means it's able to resolve smaller scales.

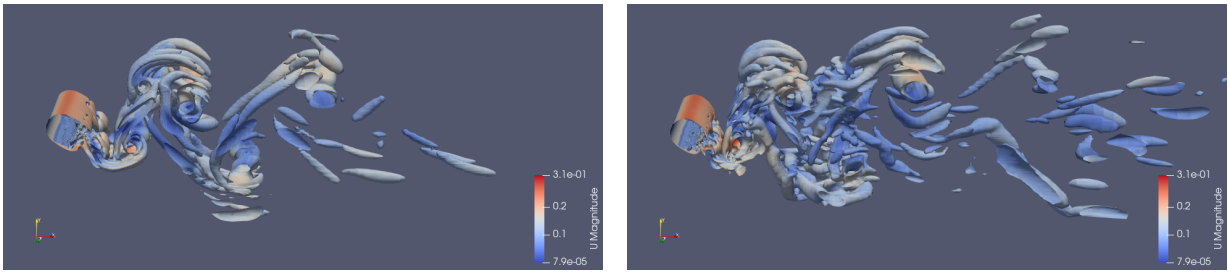

(a) IDDES **(b)** SE

Figure 5.4: Instantaneous view of coherent vortex structures for t=100s and U* =5.73

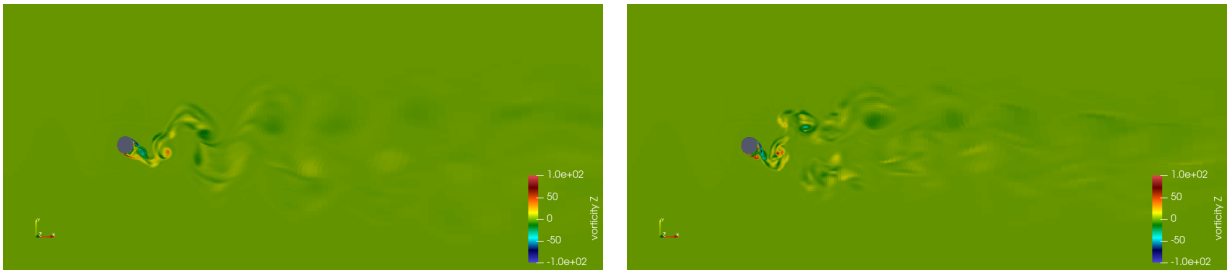

(a) IDDES **(b)** SE

Figure 5.5: Instantaneous Vorticity contour of elastically mounted cylinder at U*=5.73 on z/D=0 for t=130s

The instantaneous vorticity contour for the two models at t=130 and on the plane z/D=0 is as in Fig. 5.5. These two contours can visualize the flow and wake behind the cylinder in terms of vorticity. It is observed that the wake also shows an oscillating behavior for both IDDES and SE. However for SE, the dispersion is less in comparison to IDDES as can be inferred from the cluster of eddies in the lower region of the wake that emerged during the previous oscillation.

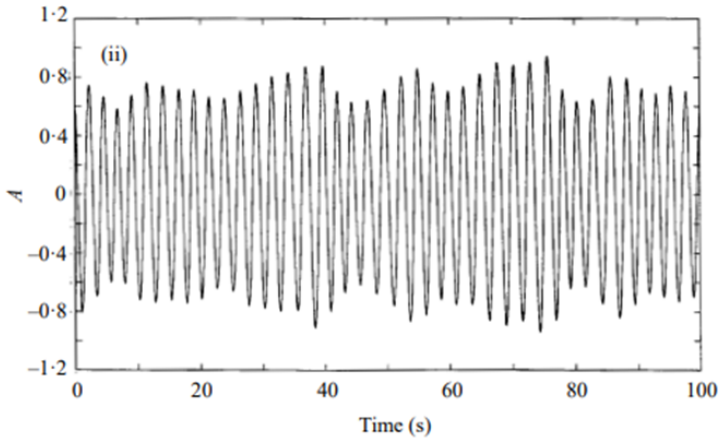

Figure 5.6: Reference For Displacement (Khalak et al.)

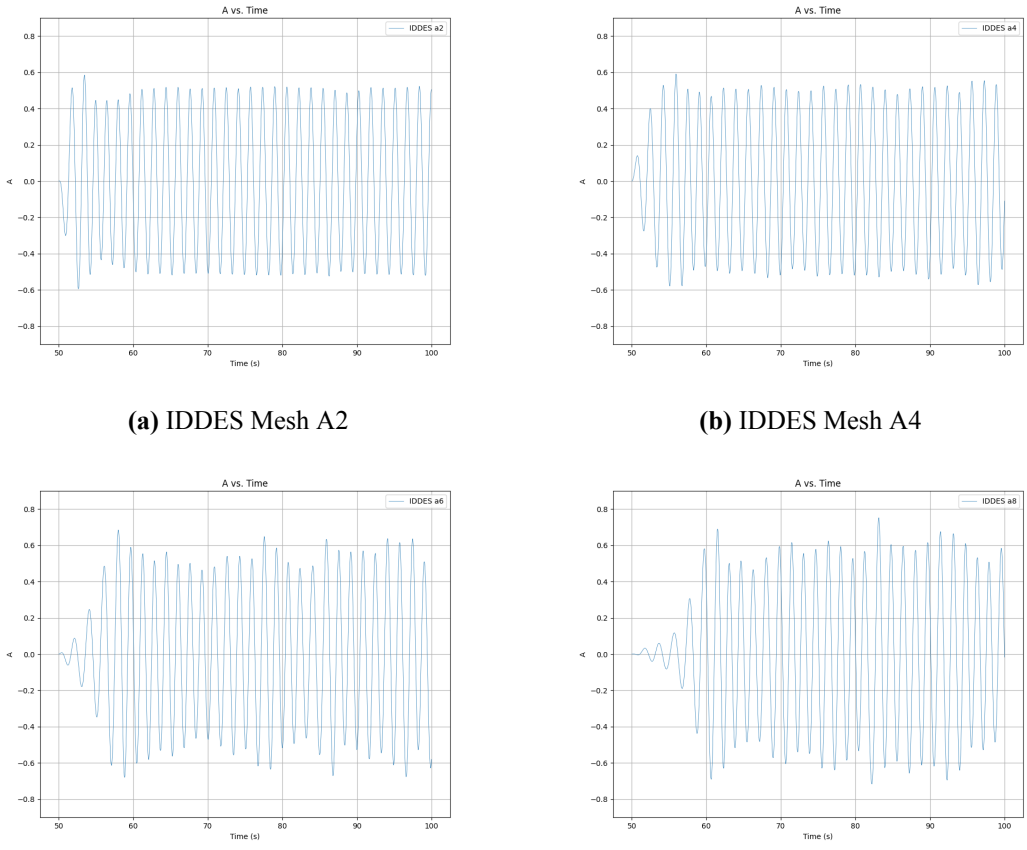

(a) IDDES Mesh A2

(b) IDDES Mesh A4

(c) IDDES Mesh A6

(d) IDDES Mesh A8

Figure 5.7: Displacement Plot for IDDES Turbulence Model

The displacement time history after the flow achieves the steady state and the cylinder is released from rest along with corresponding results from experimental data is as in Fig. 5.6 for IDDES and experimental reference and Fig. 5.8 for SE. It is observed that the amplitude of displacement increases with the mesh refinement for both IDDES and SE. However IDDES shows a less

sensitivity to mesh refinement as compared to SE. The frequency is almost unaffected by the mesh resolution, but both IDDES and SE the results show a frequency of 0.61 Hz approximately while the reference has 0.40 HZ, which means the models over-predict the frequency.

For the lift coefficient, the experimental data was not available. So, the results of the implementation of $k-\omega SST$ model [53] are used as a reference, and it was observed that the average Cl value was approximately 0 similar to that of a static cylinder.However Cd value in both cases is averaging to almost twice to that of a static cylinder which has a Cd=1. The amplitude of the lift coefficient data decreases with mesh refinement. This is because the increase in mesh refinement reduces the error and increase the precision in calculation of the coefficient. This trend is shown by both IDDES and SE model as illustrated in figure Fig. 5.9 and Fig. 5.10 respectively. However, the SE model has a lower amplitude of Cl compared to the IDDES model on the same mesh level.

A8 mesh shows instability this is possible because the convergence criteria of the simulation is 1×10^{-6} for all the variables for all the simulations but at certain points the timestep size reaches to 1×10^{-5} for the finest mesh which makes numerical error significant in those regions.

Spectral Analysis is conducted to evaluate the frequency of the oscillations for both the turbulence models. Hamming filter window is added for averaging so that the peak is captured accurately. The results of the spectral analysis on spectral scale for both Cl and displacement A are illustrated

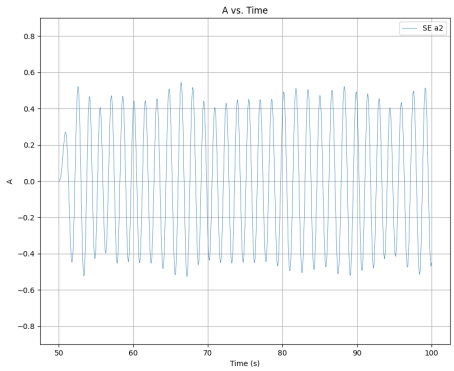

(a) Mesh A2

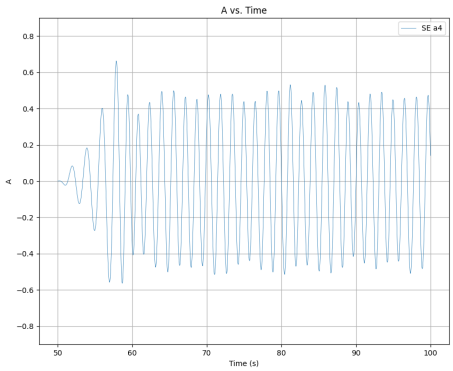

(b) Mesh A4

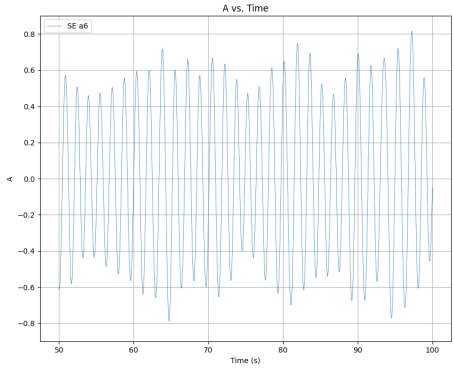

(c) Mesh A6

Figure 5.8: Displacement Plot for SE Turbulence Model

in figures Fig. 5.11 and Fig. 5.12 for IDDES and SE respectively. The spectral analysis of the results from URANS case using cubic $k-\varepsilon$ model is also added for comparison. It is observed that the hybrid models even on coarser mesh are able to resolve much smaller scales when compared to the RANS model. However, the displacement corresponding to peak frequency in spectral analysis is underprediction of experimental value, which could be due to insufficient data points.

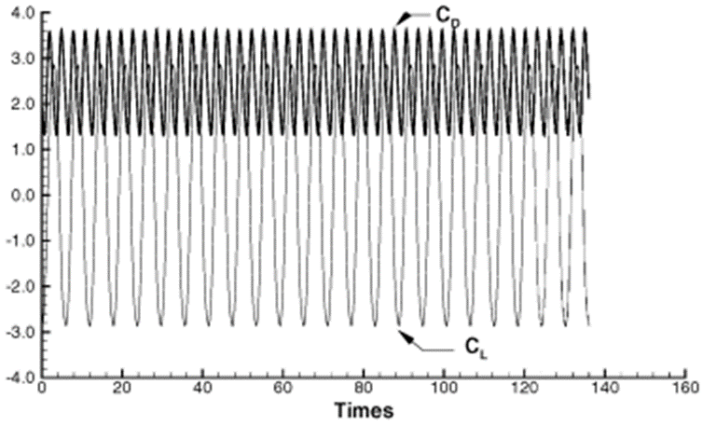

(a) Reference For Lift Coefficient (Guilmineau* et al.)

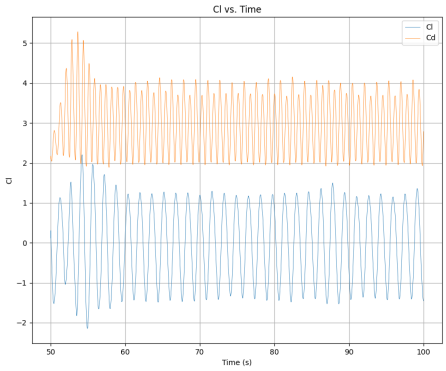

(b) Mesh A2

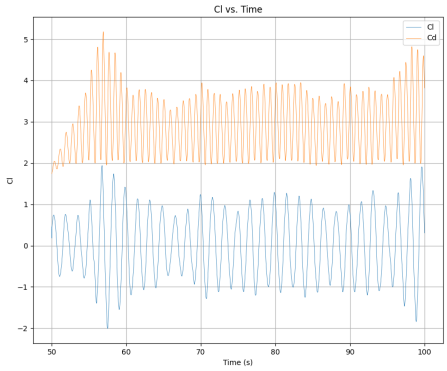

(c) Mesh A4

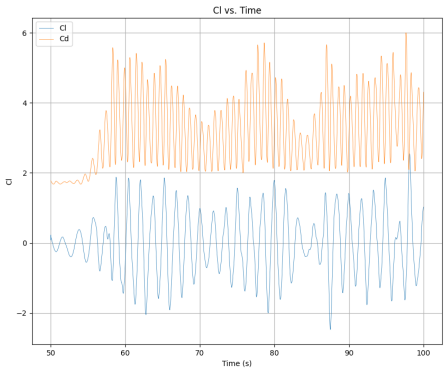

(d) Mesh A6

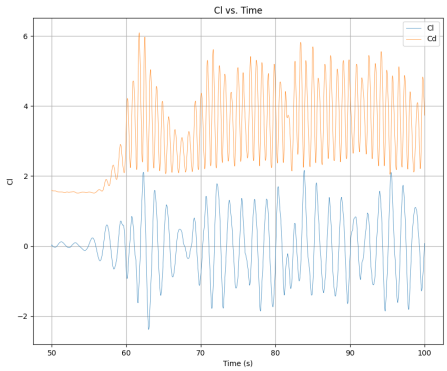

(e) Mesh A8

Figure 5.9: Lift Coefficient Plot for IDDES Turbulence Model

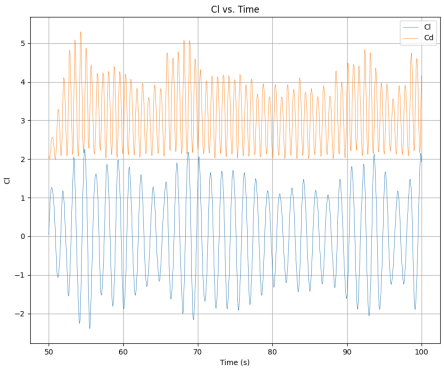

(a) Mesh A2

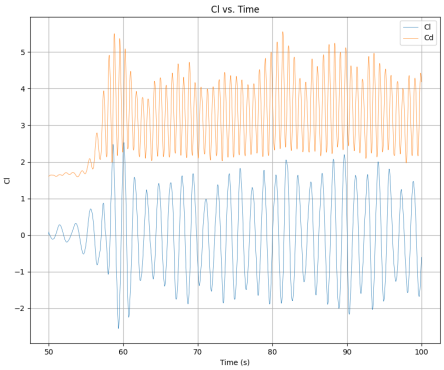

(b) Mesh A4

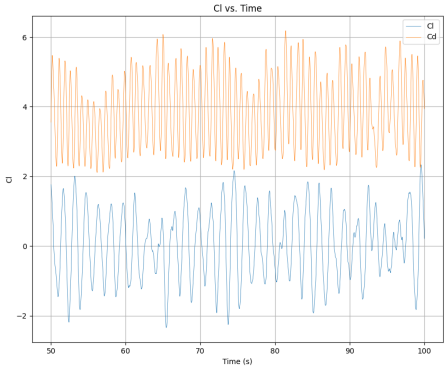

(c) Mesh A6

Figure 5.10: Lift Coefficient Plot for SE Turbulence Model

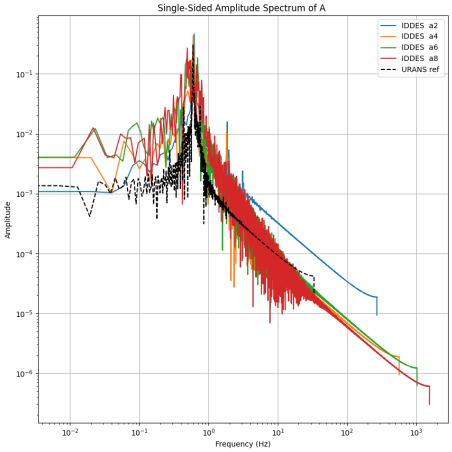

(a) Displacement Spectrum

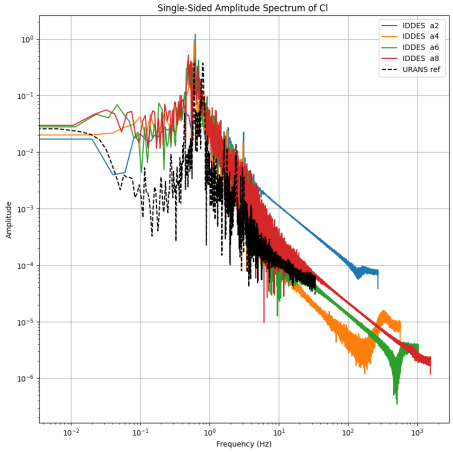

(b) Cl time history Spectrum

Figure 5.11: Spectral Analysis for IDDES

Therefore, due to time constraint a more qualitative analysis for frequency is done by calculating

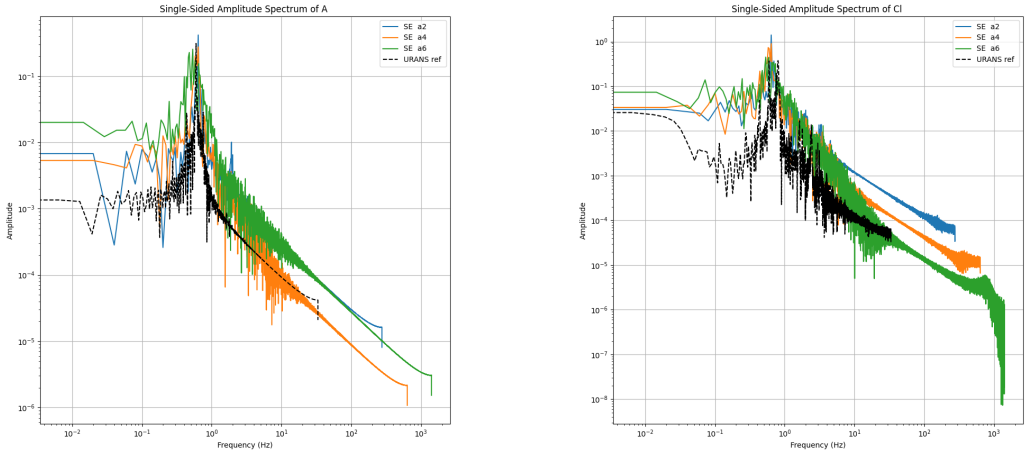

(a) Displacement Spectrum **(b)** Cl history Spectrum

Figure 5.12: Spectral Analysis SE

the average time period between two peak points and finding the average frequency from that value. The maximum displacement amplitude A is also directly extracted from the displacement data. The result for amplitude and frequency response at $U^* = 5.73$ by using both spectral analysis and direct calculation are as in Table 5.3.

Since these results were imprecise due to previously discussed reasons, average frequency are calculated from the datasets along it maximum displacements peak (as done in Williamson et al.). The displacement d and frequency f is normalized by the diameter of cylinder and natural frequency of cylinder in air ($f_{n_{air}} = 0.532Hz$) respectively.

$$A = \frac{d}{D} \tag{5.1}$$

$$f* = \frac{f}{f_{n_{air}}} \tag{5.2}$$

Table 5.3: Displacement and Frequency Response for U^* =5.73

Source	**A [-]**	**% error in A**	**f [Hz]**	**f* [-]**
Analytical for fixed cylinder			0.6916	1.3
Exp data (Lee)			0.48838	0.918 at ζ=0.02
Exp data (K&W)	0.95	0	-	-
(G &Q)-komega SST	0.547	0.424211	0.6118	1.15
Cubic kepsilon (Muaaz)	0.568	0.402105	0.60648	1.14
IDDES A2 (Spectral Analysis)	0.464	0.511579	0.61712	1.16
IDDES A4 (Spectral Analysis)	0.44	0.536842	0.59956	1.127
IDDES A6 (Spectral Analysis)	0.185	0.805263	0.6916	1.3
IDDES A8 (Spectral Analysis)	0.335	0.647368	0.49476	0.93
IDDES A2 (Maximum Peak)	0.584	0.385263	0.62138	1.168
IDDES A4 (Maximum Peak)	0.5909	0.378	0.60595	1.139
IDDES A6 (Maximum Peak)	0.684	0.28	0.60116	1.13
IDDES A8 (Maximum Peak)	0.7518	0.208632	0.58786	1.105
SE A2 (Spectral Analysis)	0.418	0.56	0.64	1.203
SE A4 (Spectral Analysis)	0.275	0.710526	0.64	1.203
SE A6 (Spectral Analysis)	0.255	0.731579	0.53413	1.004
SE A2 (Maximum Peak)	0.6422	0.324	0.64212	1.207
SE A4 (Maximum Peak)	0.6625	0.302632	0.6384	1.2
SE A6 (Maximum Peak)	0.815	0.142105	0.60116	1.13

The results also show that on even coarsest meshes Hybrid Models give comparable results to RANS models. However, RANS models are not able to provide precise results for the velocities where the transition between the upper and lower branches of amplitude curves occurs [53]. Therefore another set of simulations were run on a lower velocity at U^* =4.5 to verify the accuracy of hybrid models and their advantage over RANS in that region.

5.5. U* = 4.5

The same case set up is then simulated for a velocity of 0.09 m/s which correspond to U* 4.5.

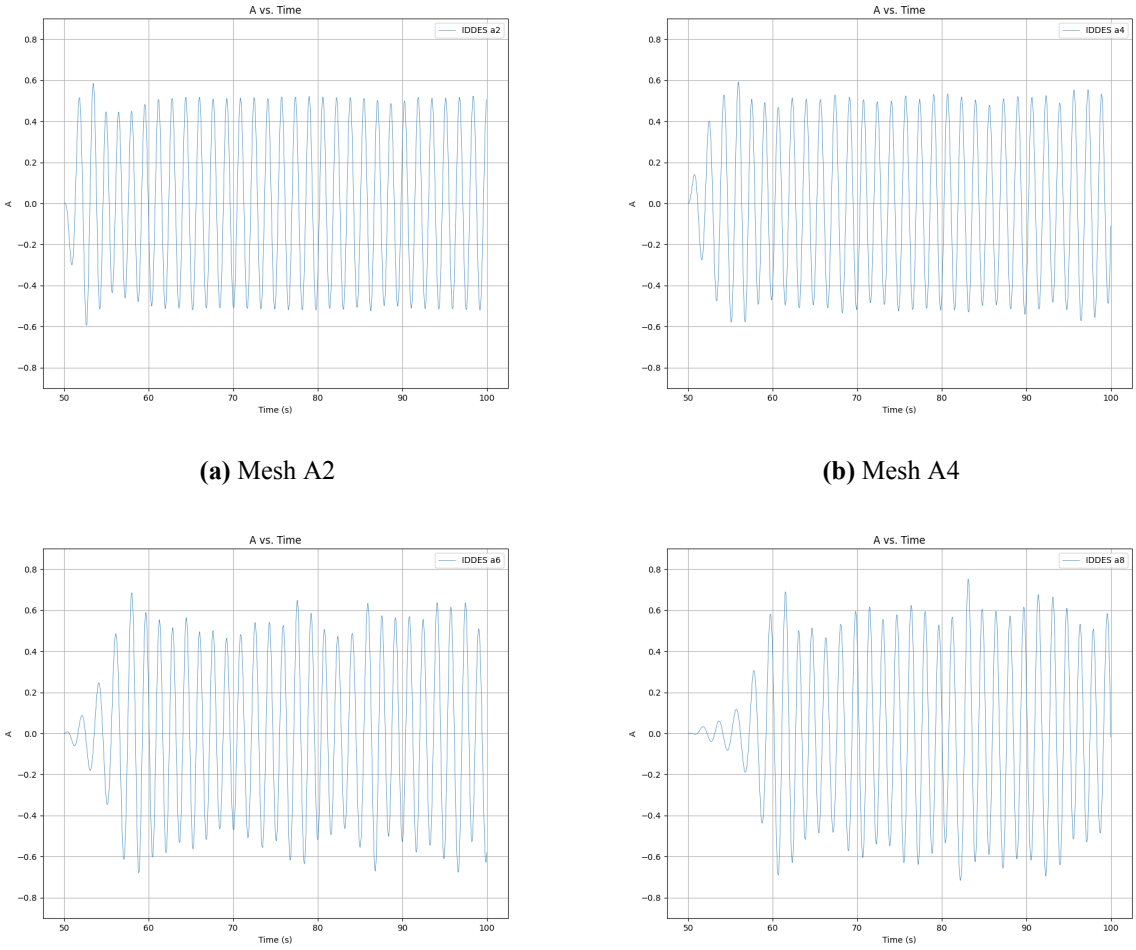

(a) Mesh A2

(b) Mesh A4

(c) Mesh A6

(d) Mesh A8

Figure 5.13: Displacement Plot for IDDES Turbulence Model

The displacement plots for different mesh levels for both IDDES and SE model as in Fig. 5.13 and Fig. 5.14 respectively. As expected the amplitude of displacement increases mesh level.

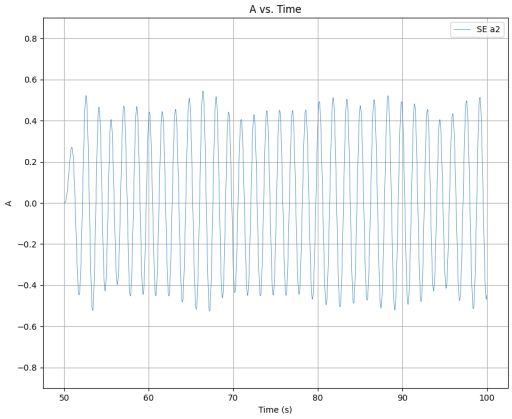

(a) Mesh A2

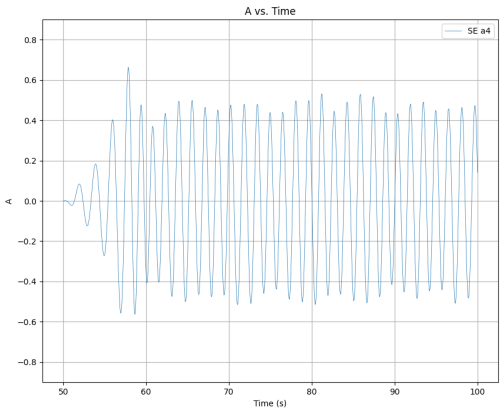

(b) Mesh A4

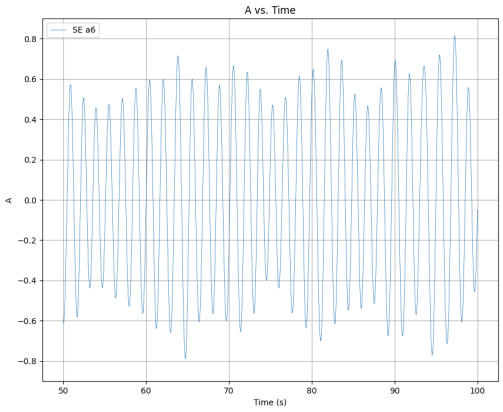

(c) Mesh A6

Figure 5.14: Displacement Plot for SE Turbulence Model

The Cl plots for both IDDES and SE model are as in Fig. 5.15d and Fig. 5.16. The fluctuation in the Cl data oscillations seems to increase with the mesh refinement. The the mean Cl value $\simeq 0$ which can inferred from the fact that the oscillation occurs around Cl = 0.

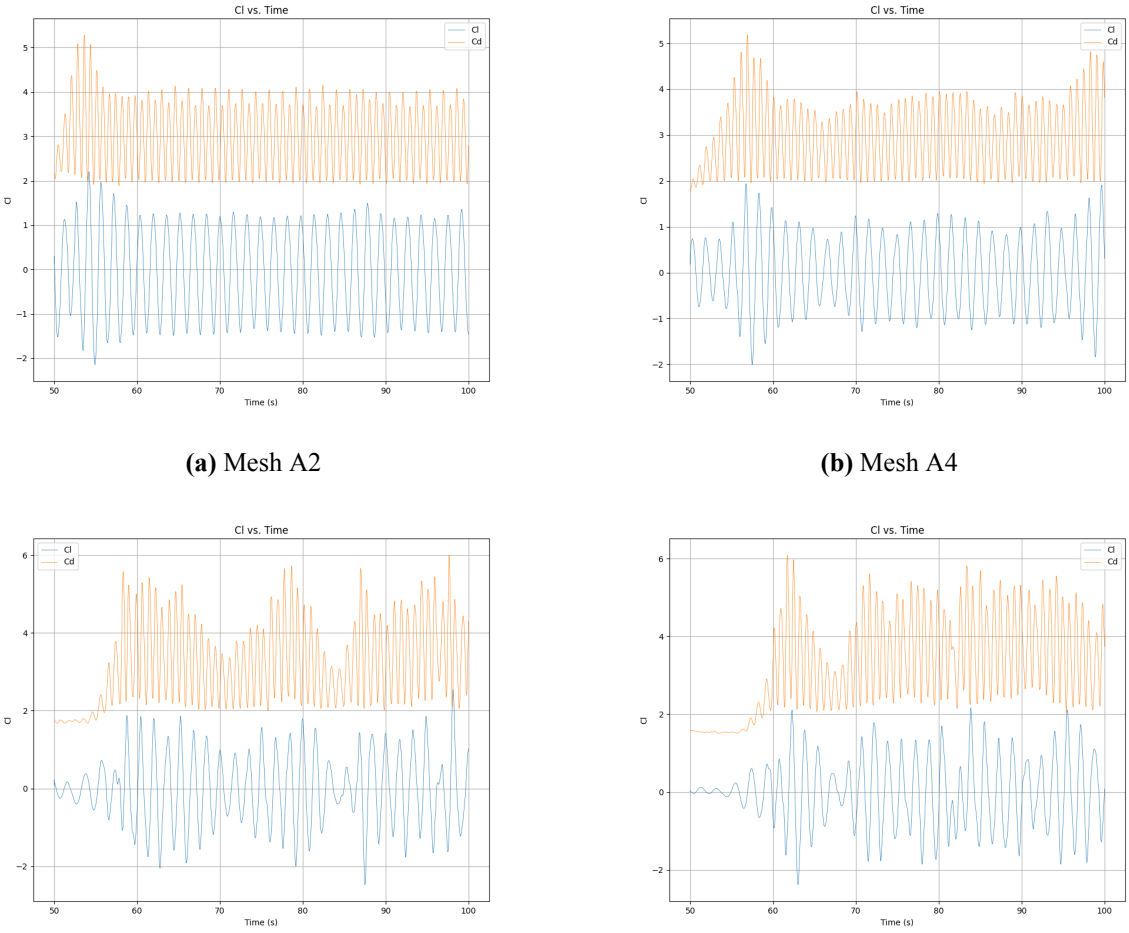

(a) Mesh A2

(b) Mesh A4

(c) Mesh A6

(d) Mesh A8

Figure 5.15: Lift Coefficient Plot for IDDES Turbulence Model

Repeating the procedure of frequency calculation from Section 5.4 it was again observed that the amplitude of displacement achieved using spectral analysis is not equivalent to what can be observed in the displacement time history and therefore the spectral analysis method is unsuitable for evaluating the frequency. This might be because there isn't enough data points due to time constraint. It is also observed that even on smaller velocity value RANS model even though it models lesser range of frequencies is able to provide a defined peak and can be used for spectral analysis.

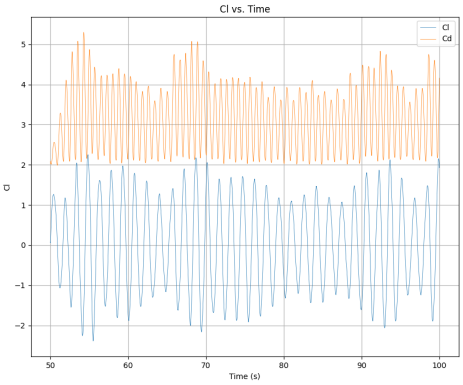

(a) Mesh A2

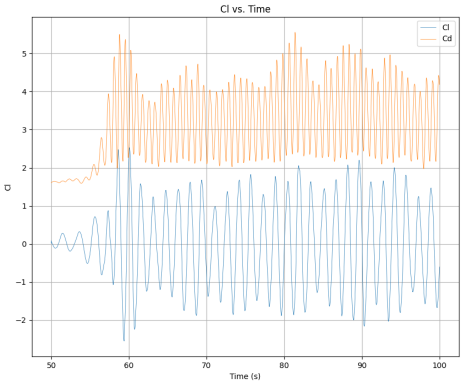

(b) Mesh A4

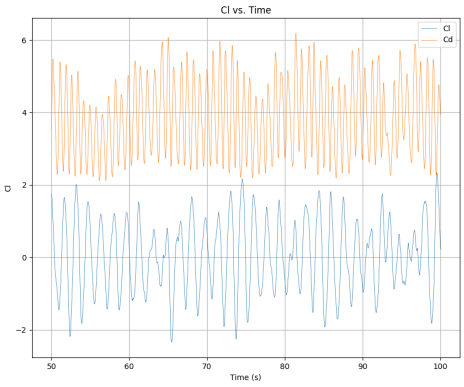

(c) Mesh A6

Figure 5.16: Lift Coefficient Plot for SE Turbulence Model

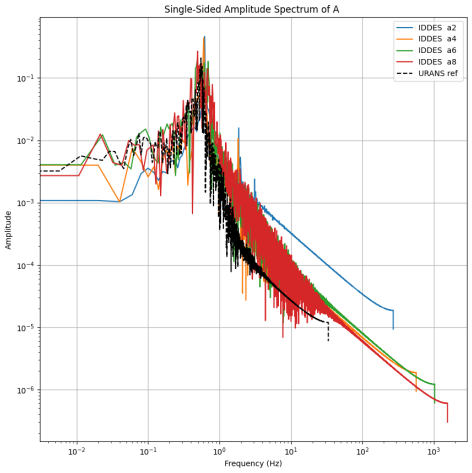

(a) Displacement Spectrum

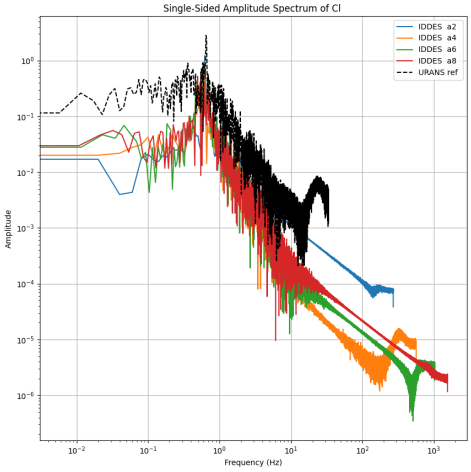

(b) Cl Spectrum

Figure 5.17: Spectral Analysis IDDES

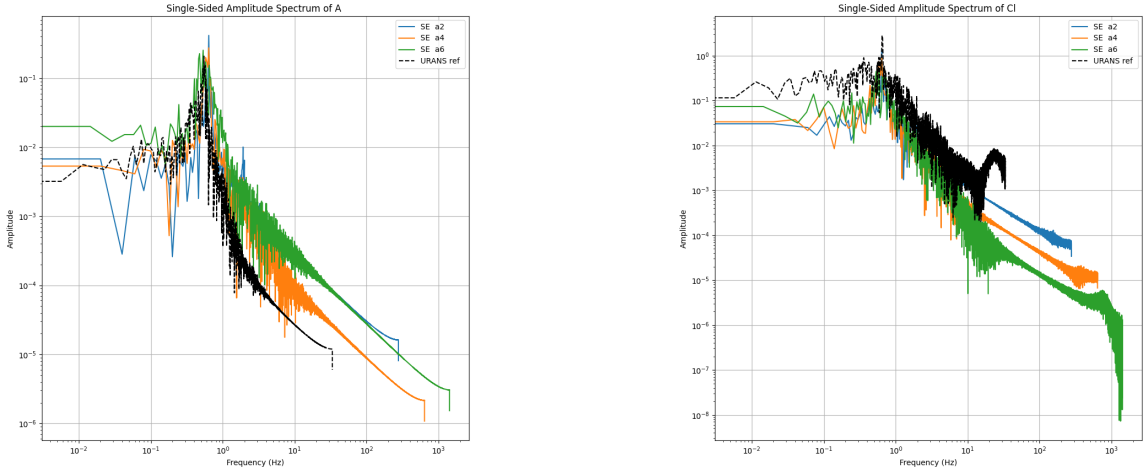

(a) Displacement Spectrum **(b)** Cl Spectrum

Figure 5.18: Spectral Analysis SE

Table 5.4: Displacement and Frequency Response for U^* =4.5

Source	**A [-]**	**% error in A**	**f [Hz]**	**f* [-]**
Analytic for fixed cylinder			0.53892	1.013
Exp data (K&W)	0.84	0	0	
(G &Q) komega SST	0.59	0.297619	0.54264	1.02
Cubic kepsilon (Muaaz)	0.92	0.095238	0.47348	0.89
IDDES A2 (Spectral Analysis)	0.487	0.420238	0.54796	1.03
IDDES A4 (Spectral Analysis)	0.205	0.755952	0.51125	0.961
IDDES A6 (Spectral Analysis)	0.406	0.516667	0.43305	0.814
IDDES A8 (Spectral Analysis)	0.435	0.482143	0.43518	0.818
IDDES A2 (Maximum Peak)	0.647	0.229762	0.55222	1.038
IDDES A4 (Maximum Peak)	0.839	0.00119	0.52189	0.981
IDDES A6 (Maximum Peak)	0.916	0.090476	0.49476	0.93
IDDES A8 (Maximum Peak)	0.885	0.053571	0.48838	0.918
SE A2 (Spectral Analysis)	0.503	0.40119	0.54956	1.033
SE A4 (Spectral Analysis)	0.347	0.586905	0.49524	0.9309
SE A6 (Spectral Analysis)	0.426	0.492857	0.49476	0.93
SE A2 (Maximum Peak)	0.626	0.254762	0.55328	1.04
SE A4 (Maximum Peak)	0.807	0.039286	0.52562	0.988
SE A6 (Maximum Peak)	0.793	0.055952	0.52402	0.985

Since spectral method doesn't provide a precise result for frequency calculation the average frequency is calculated from the data set along with the amplitude of displacement. The result for displacement and frequency being compared for different turbulence models, mesh sizes and calculation methodology a stated in Table 5.4.

The cubic $k - \varepsilon$ model [54] on about 60,000 cells 2D mesh provides better calculation for displacement and frequency than it's hybrid counterparts on similar size mesh of level A4 containing a total of 100K cells devided in 12 spanwise layers and containing around 35,000 cells in a 2D plane at spanwise centerline. Based on this observation it is possible that RANS model provides more accurate results on smaller velocity which is before the transition reason in the amplitude curve's upper branch.

While comparing the SE and IDDES model it was observed that for U^* = 4.5, SE under predicts the displacement on the final mesh while IDDES over-predicts it. it was also observed that the SE provides more accurate result for displacement in comparison to the IDDES model.

5.6. Displacement and Frequency Response

While comparing the SE and IDDES model it was observed that for U^* = 4.5, SE under-predicts the displacement on the final mesh while IDDES over-predicts it. it was also observed that the SE provides more accurate result for displacement and frequency in comparison to the IDDES model.

The primary result for the amplitude response and the Frequency response curve is shown in the Fig. 5.19. The plot also has references from the experimental data as well as the reference data from RANS solvers $k - \omega$ SST and cubic $k - \varepsilon$. For the amplitude response curve the performance of models is quite mixed with different models performing better on different points in the response space. for the upper branch at the velocity of U^* = 4.5 it is observed that the IDDES model is able to give the most accurate amplitude response followed by the SE model. The RANS reference for the turbulence model cubic $k - \varepsilon$ is also able to produce the amplitude response in the same range as the experiment but it still has a significant error. As the velocity increases and the region of high-amplitude peak on the upper branch is approached at U^* = 5.73, on coarse mesh the models are not able to predict the amplitude precisely, but SE provides the most accurate result followed by IDDES.

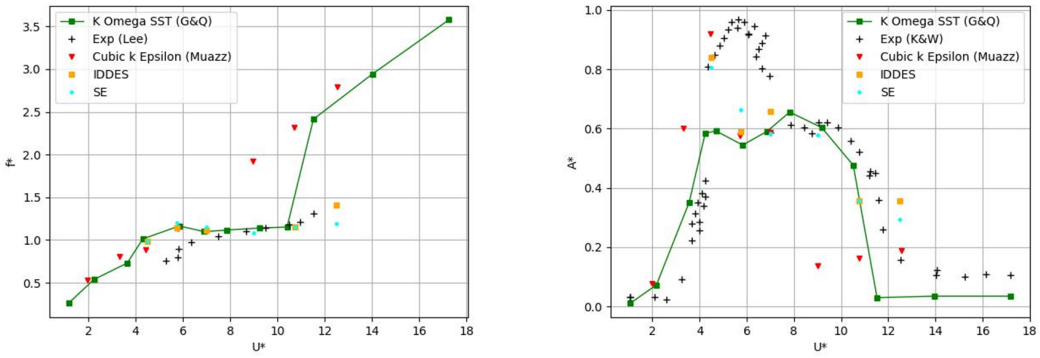

(a) Frequency Response Curve **(b)** Amplitude Response Curves

Figure 5.19: Response Curves

At U^* = 7 where the transition is happening from the upper branch to the lower branch in these regions the hybrid models will give similar level of accuracy as the RANS reference. The amplitude response is under predicted in this region, but IDDES gives a better performance as compared to SE. At U^*= 9 the IDDES mesh kept on failing. This might be due to the fact that in this region the switch from the upper branch to lower branch of response curve takes place, so so it is possible that the solver is having difficulty to approach the locked in frequency in this region.

An attempt was also made to simulate the flow using the 2 models for U^*=9 which is in the vicinity of lockin frequency. The result for SE models are as in the result plot but for IDDES the simulation became unstable and the solution diverged even on reducing the timestep. The maximum CFL was reduced to 0.2 from the default 0.7 value to reduce the timestep. However, the solution still diverged. This indicates the possibility of IDDES model being less robust in comparison to SE. However further research needs to be done with multiple scenarios to make a conclusion regarding this.

On the lower branch it is observed that at low frequency the are able to get much more precise results for the amplitude response at 10.75 but the error percentage increases at U^* = 12.5 this might be because in this region the there is a very sharp slope which makes it difficult to accurately predict the amplitude in this region as small perturbation leads to large amplitude change.

For the frequency response curve, it is observed that the IDDES and SE models are able to predict the frequency with much better precision to experimental data. The analysis here is quite qualitative as the experimental results are not exact. This is because there is a difference in damping ratio for the test case compared with this reference. However it is observed that the RANS references over predict the frequency by a factor of 2 and seem to follow the path of a rigid cylinder for the velocities corresponding to the lower branch of amplitude curve.

5.7. Computational Efficiency

The computational efficiency of the two shortlisted model IDDES and SE is compared. As evident from Fig. 5.20a, contrary to static cylinder case for moving mesh based simulation is slower that is it takes more CPU time to run a simulation over a same time period. This means that for the FSI implementation, SE is computationally more expensive compared to the IDDES turbulence model.

However, the SE model has less error percentage in calculation of amplitude of displacement at mesh sizes. As shown in Table 5.2 the SE model provides a better result by a factor of 5 to 15% calculation of displacement amplitude during the oscillation of the cylinder in y direction. based on these observation from computational efficiency point of view, SE up is more suitable because for a small increase in computation time a difference in error percentage of 10 to 15% can be achieved.

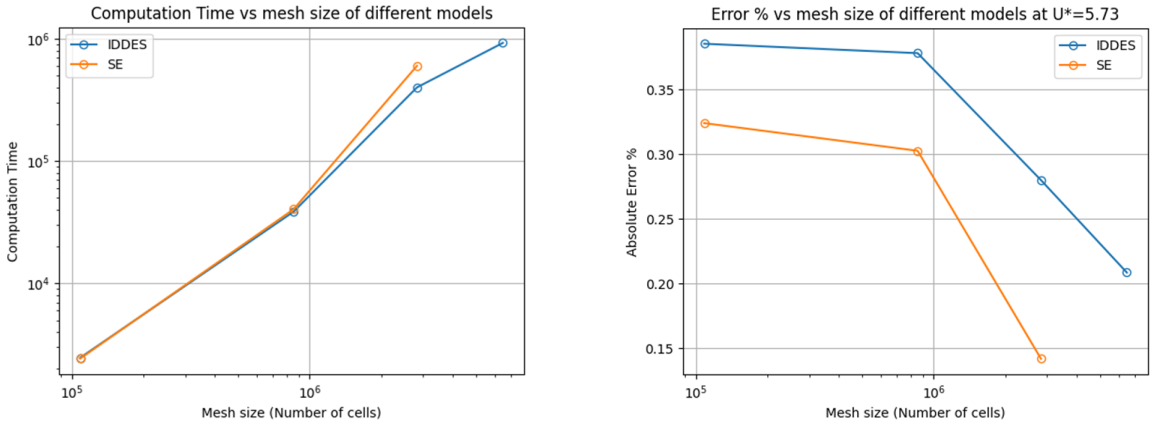

(a) Computation Time Plot **(b)** Absolute Error in Amplitude of Displacement

Figure 5.20: Grid Dependency and Computation Time

Even though SE is computationally expensive that IDDES on finer mesh, the Error Convergence plot in Fig. 5.21 shows that for a given computation time SE provides results with less error than IDDES. So even if we compute the problem on a coarser mesh to match the computation time of IDDES, we will get better solution for displacement. This concludes that SE is more efficient model than IDDES.

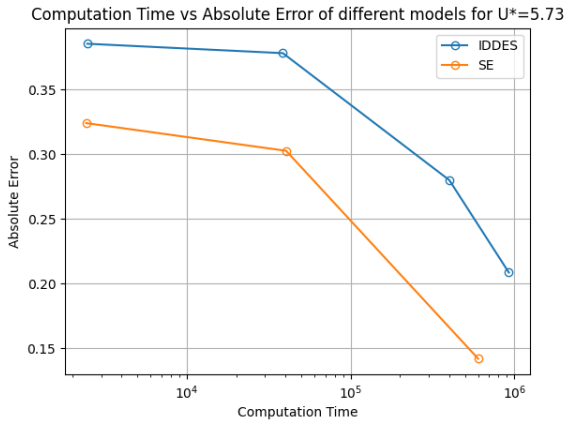

Figure 5.21: Error vs Computation Time

6

Conclusion

This thesis Focuses on implementation of hybrid turbulence models for simulation of fluid structure interaction based problems. To carry out an FSI study one may need to choose a high fidelity method like Large Eddy Simulations for accuracy or have to depend on the results by solving mean flows values using RANS. To create a balance between these two extreme situations, Hybrid RANS-LES models are analyzed in this thesis to evaluate their ability to solve FSI problems with better accuracy and less computation time. In doing so the following research objective has been described for the thesis work:

Research Objective

To identify suitable Hybrid RANS LES Models, implement and validate them on the open-source software and to compare them, shortlisting the FSI suitable models .

This objective is carried out by dividing the whole project into 5 stages. First literature analysis of the available hybrid turbulence models is conducted and the models are classified into different categories so that a single model can be selected from each category and compared against each other. Four models were shortlisted in this section: IDDES, SAS, PANS and SE. The second step was to implement these hybrid models into open source simulation software OpenFOAM. While IDDES and SAS were inbuilt in OpenFOAM, PANS library was added from a customised and publicly shared library project. SE model library was created by modifying the available cubic $k - \varepsilon$ model.

The turbulence models were tested for a fixed cylinder in crossflow and using different mesh refinement. It was observed that IDDES produces the most accurate results for wake flow variables as well as force components on the cylinder surfaces. SE is the most efficient in terms of error percentage and computation time. The SAS model was observed to be highly unstable, specially on the finest mesh A8. PANS produced accurate results and is comparable to IDDES in terms of accuracy of result and computation time. However, due to time constraint, two models, IDDES and SE, were shortlisted further analysis.

The next is implementation of the selected hybrid models for a simple FSI case of elastically mounted 1 DOF cylinder in crossflow. The IDDES and SE models which were selected in the previous stage were implemented to simulate the test case for different non denationalised velocities U*. It was observed that even though the amplitude and frequency response for the

two models show mixed performance where on different velocities different model has a better performance. However the initial assumption trend of these hybrid models that they will be more efficient than RANS, which is proven true.

The next step is to analyse if the research object has been fulfilled. The research questions posed in Chapter 1 are repeated below for convenience to explain precisely the investigated answers to these questions.

Research Question 1

Which hybrid turbulence models provides the most accurate flow solution for a statically steady case of fixed cylinder in crossflow?

1. What is the grid sensitivity of these different models ?
2. Which of these models are most efficient and has least computation time?
3. What parameters should be considered essential for selection of turbulence model for a FSI case?
4. Which models from the available literature are most viable for FSI implementation?

For a cylinder in crossflow case using hybrid models it was observed that the IDDES model converges to the experimental value for both wake region parameters like velocity and Reynolds stress as well as parameters like forces being solved over the surface. SE also provides comparable results and has less grid dependence; computes to solution with less error on coarser mesh. Therefore IDDES and SE were selected for the FSI application after both literature review and comparative analysis on the bases of accuracy and computational efficiency.

Research Question 2

Are the selected Hybrid Turbulence models able to solve an FSI system?

1. Which parameters should be considered for the evaluation? How are the hybrid turbulence models performing in calculation of these parameters?
2. What is the effect of mesh refinement?
3. How are they performing when compared to RANS models?

The selected hybrid models are able to solve a simple FSI case of elastically mounted rigid cylinder experiencing oscillations due to turbulence induced vibrations under crossflow. The frequency and amplitude response of the cylinder are considered to be the appropriate parameters for this comparison. It was observed that for both SE and IDDES, the error in calculation of amplitude of displacement reduces with mesh refinement but error in evaluating frequency response increases. Between the 2 models, SE provided more accurate results for amplitude response but is also more computationally expensive as it takes more CPU time. Finally when compared to RANS, it was observed that hybrid models provide better results for amplitude and frequency response than RANS models like cubic $k-\varepsilon$. Therefore hybrid turbulence models seem to be a viable option to be researched further into for the CFD module of an FSI solver.

7

Recommendations

This chapter provides a brief overview of the primary recommendations for the future continuation of this research project.

Recommendation 1

Check Applicability for Complex Cases: Future work should involve applying the methodology to more complex test cases, such as scenarios involving bundled tube in crossflow. This will help verify the approach's robustness and effectiveness in handling intricate flow dynamics, ensuring its broader applicability in real-world situations.

Recommendation 2

Implementing Explicit Solver Scheme: Given the small timestep requirements, it is recommended to explore the implementation of an explicit solver scheme. This approach could potentially enhance computational efficiency and accuracy, providing deeper insights into the solver's performance under different conditions.

Recommendation 3

Testing with Stronger Coupled Systems: To further validate the turbulence models used, it is essential to test them against more strongly coupled FSI systems. This would help to determine their reliability and accuracy in predicting turbulent behavior in highly interactive flow environments, ultimately contributing to better model development and optimization.

References

[1] CC BY NC SA 4.0 (Annex A). *World Energy Outlook 2023, IEA, Paris*. Tech. rep. Paris: IEA, 2023. URL: https://www.iea.org/reports/world-energy-outlook-2023.

[2] Thomas Gasser et al. "Edgar Hertwich (USA/Austria), Lena Höglund-Isaksson". In: (2018). DOI: 10.1017/9781009157940.004. URL: https://doi.org/10.1017/9781009157940.004..

[3] Anthony W Thomas. "THE ROLE OF NUCLEAR POWER IN A SUSTAINABLE FUTURE". In: (). DOI: 10.1071/RS23008. URL: https://debunkingdenial.com/portfolio/the-future-of-.

[4] Mustafa Babiker et al. "Lead Authors: Contributing Authors: Review Editors: Strengthening and Implementing the Global Response". In: (). DOI: 10.1017/9781009157940.006. URL: https://doi.org/10.1017/9781009157940.006..

[5] Amory B. Lovins et al. "Relative deployment rates of renewable and nuclear power: A cautionary tale of two metrics". In: *Energy Research & Social Science* 38 (Apr. 2018), pp. 188–192. DOI: 10.1016/J.ERSS.2018.01.005.

[6] Anil Markandya et al. "Electricity generation and health". In: *Lancet* 370.9591 (Sept. 2007), pp. 979–990. DOI: 10.1016/S0140-6736(07)61253-7. URL: http://www.thelancet.com/article/S0140673607612537/fulltext%20http://www.thelancet.com/article/S0140673607612537/abstract%20https://www.thelancet.com/journals/lancet/article/PIIS0140-6736(07)61253-7/abstract.

[7] Benjamin K. Sovacool et al. "Balancing safety with sustainability: assessing the risk of accidents for modern low-carbon energy systems". In: *Journal of Cleaner Production* 112 (Jan. 2016), pp. 3952–3965. DOI: 10.1016/J.JCLEPRO.2015.07.059.

[8] K H Luk. "NUREG/CR-5754, "Boiling-Water Reactor Internals Aging-Degradation Study"." In: ().

[9] Pablo Fernández-Arias et al. "A Global Review of PWR Nuclear Power Plants". In: *Appl. Sci* 2020 (), p. 4434. DOI: 10.3390/app10134434. URL: www.mdpi.com/journal/applsciArticle.

[10] Mark Ho et al. "A review on the development of nuclear power reactors". In: *Energy Procedia* 160 (Feb. 2019), pp. 459–466. DOI: 10.1016/J.EGYPRO.2019.02.193.

[11] Abiodun Ayodeji et al. "PWR heat exchanger tube defects: Trends, signatures and diagnostic techniques". In: *Progress in Nuclear Energy* 112 (Apr. 2019), pp. 171–184. DOI: 10.1016/J.PNUCENE.2018.12.017.

[12] Emil Mammadzada et al. "Thorium fuel Performance: A comparative study on thorium's efficiency in PWR reactors". In: *Nuclear Engineering and Design* 424 (Aug. 2024), p. 113306. DOI: 10.1016/J.NUCENGDES.2024.113306.

[13] M. P. Païdoussis. “Real-life experiences with flow-induced vibration”. In: *Journal of Fluids and Structures* 22.6-7 (Aug. 2006), pp. 741–755. DOI: 10.1016/J.JFLUIDSTRUCTS.2006.04.002.

[14] K.H. Luk. “Boiling-Water Reactor internals aging degradation study. Phase 1”. In: (Sept. 1993). DOI: 10.2172/10182155. URL: http://www.osti.gov/servlets/purl/10182155-gw29uV/.

[15] D. S. Weaver et al. “Flow-Induced Vibrations in Power and Process Plant Components—Progress and Prospects”. In: *Journal of Pressure Vessel Technology* 122.3 (Aug. 2000), pp. 339–348. DOI: 10.1115/1.556190. URL: https://dx.doi.org/10.1115/1.556190.

[16] Jia-song Wang et al. “A review on flow-induced vibration of offshore circular cylinders”. In: *Journal of Hydrodynamics* 32.3 (June 2020), pp. 415–440. DOI: 10.1007/s42241-020-0032-2.

[17] J. H. Lever et al. “A Theoretical Model for Fluid-Elastic Instability in Heat Exchanger Tube Bundles”. In: *Journal of Pressure Vessel Technology* 104.3 (Aug. 1982), pp. 147–158. DOI: 10.1115/1.3264196. URL: https://dx.doi.org/10.1115/1.3264196.

[18] K. Schröder et al. “Two- and three-dimensional CFD-simulation of flow-induced vibration excitation in tube bundles”. In: *Chemical Engineering and Processing: Process Intensification* 38.4-6 (Sept. 1999), pp. 621–629. DOI: 10.1016/S0255-2701(99)00063-X.

[19] Rajeev Jaiman et al. *Mechanics of Flow-Induced Vibration*. Singapore: Springer Nature Singapore, 2023. DOI: 10.1007/978-981-19-8578-2.

[20] Yahya Modarres-Sadeghi. *Introduction to Fluid-Structure Interactions*. Cham: Springer International Publishing, 2021. DOI: 10.1007/978-3-030-85884-1.

[21] S. Kottapalli et al. “Numerical investigation of an advanced U-RANS based pressure fluctuation model to simulate non-linear vibrations of nuclear fuel rods due to turbulent parallel-flow”. In: *Annals of Nuclear Energy* 128 (June 2019), pp. 115–126. DOI: 10.1016/J.ANUCENE.2019.01.001.

[22] Jeroen De Ridder et al. “Simulating the fluid forces and fluid-elastic instabilities of a clamped–clamped cylinder in turbulent axial flow”. In: *Journal of Fluids and Structures* 55 (May 2015), pp. 139–154. DOI: 10.1016/J.JFLUIDSTRUCTS.2015.03.001.

[23] *k-corrective frozen PANS: A data-driven stochastic closure turbulence model | TU Delft Repository*. URL: https://repository.tudelft.nl/record/uuid:10994b22-677a-4cf4-ac74-47ce0ee524ca.

[24] David Wilcox. “Turbulence modeling - An overview”. In: *39th Aerospace Sciences Meeting and Exhibit*. Reston, Virigina: American Institute of Aeronautics and Astronautics, Jan. 2001. DOI: 10.2514/6.2001-724.

[25] Ka-Yen K Yau et al. *Application of Hybrid CFD Turbulence Model, STRUCT-ϵ, on Heated Flow Cases*. Tech. rep.

[26] Rüdiger Schwarze et al. “Performance and limitations of the unsteady RANS approach”. In: *PAMM* 6.1 (2006), pp. 543–544. DOI: https://doi.org/10.1002/pamm.200610252.

[27] Pietro Catalano et al. “An evaluation of RANS turbulence modelling for aerodynamic applications”. In: *Aerospace Science and Technology* 7.7 (Oct. 2003), pp. 493–509. DOI: 10.1016/S1270-9638(03)00061-0. URL: https://www.sciencedirect.com/science/article/pii/S1270963803000610.

[28] Stefan Heinz. “A review of hybrid RANS-LES methods for turbulent flows: Concepts and applications”. In: *Progress in Aerospace Sciences* 114 (Apr. 2020), p. 100597. DOI: 10.1016/j.paerosci.2019.100597. URL: https://www.sciencedirect.com/science/article/pii/S0376042119301861.

[29] Florian R. Menter et al. “Global vs. Zonal Approaches in Hybrid RANS-LES Turbulence Modelling”. In: 2012, pp. 15–28. DOI: 10.1007/978-3-642-31818-4{_}2.

[30] Philippe R. Spalart. “Hybrid RANS-LES Methods”. In: *Advanced Approaches in Turbulence*. Elsevier, 2021, pp. 133–159. DOI: 10.1016/B978-0-12-820774-1.00010-0.

[31] Hanjalić K et al. “Hybrid RANS-LES (HRL)”. In: *Modelling Turbulence in Engineering and the Environment: Rational Alternative Routes to Closure*. Ed. by Kemal Hanjalić et al. 2nd ed. Cambridge: Cambridge University Press, 2022, pp. 371–463. DOI: DOI: 10.1017/9781108875400.012. URL: https://www.cambridge.org/core/product/C3939BCFC0CC9B6712A2F70E7B6126AD.

[32] Guangxue Wang et al. “Comparative assessment of SAS, IDDES and hybrid filtering RANS/LES models based on second-moment closure”. In: *Advances in Mechanical Engineering* 13.6 (June 2021), p. 168781402110284. DOI: 10.1177/16878140211028447.

[33] Visrant Choudhury. “A Validation Study of Openfoam for Hybrid Rans-Les Simulation of Incompressible Flow over a Backward Facing Step and Delta Wing”. PhD thesis. James Worth Bagley College of Engineering, 2014. URL: https://scholarsjunction.msstate.edu/td/338.

[34] Mikhail S. Gritskevich et al. “Development of DDES and IDDES Formulations for the k-ω Shear Stress Transport Model”. In: *Flow, Turbulence and Combustion* 88.3 (Apr. 2012), pp. 431–449. DOI: 10.1007/s10494-011-9378-4.

[35] E. Guilmineau et al. “Assessment of hybrid RANS-LES formulations for flow simulation around the Ahmed body”. In: *Computers & Fluids* 176 (Nov. 2018), pp. 302–319. DOI: 10.1016/j.compfluid.2017.01.005. URL: https://www.sciencedirect.com./science/article/pii/S0045793017300051?via%3Dihub.

[36] Abdolrahim Rezaeiha et al. “CFD analysis of dynamic stall on vertical axis wind turbines using Scale-Adaptive Simulation (SAS): Comparison against URANS and hybrid RANS/LES”. In: *Energy Conversion and Management* 196 (Sept. 2019), pp. 1282–1298. DOI: 10.1016/j.enconman.2019.06.081.

[37] Y. Egorov et al. “The Scale-Adaptive Simulation Method for Unsteady Turbulent Flow Predictions. Part 2: Application to Complex Flows”. In: *Flow, Turbulence and Combustion* 85.1 (July 2010), pp. 139–165. DOI: 10.1007/s10494-010-9265-4.

[38] F. R. Menter et al. “The Scale-Adaptive Simulation Method for Unsteady Turbulent Flow Predictions. Part 1: Theory and Model Description”. In: *Flow, Turbulence and Combustion* 85.1 (July 2010), pp. 113–138. DOI: 10.1007/s10494-010-9264-5.

[39] Sharath S. Girimaji. “Partially-Averaged Navier-Stokes Model for Turbulence: A Reynolds-Averaged Navier-Stokes to Direct Numerical Simulation Bridging Method”. In: *Journal of Applied Mechanics* 73.3 (May 2006), pp. 413–421. DOI: 10.1115/1.2151207. URL: https://dx.doi.org/10.1115/1.2151207.

[40] Arnab Chakraborty et al. “Study of turbulent flow past a square cylinder using partially-averaged Navier–Stokes method in OpenFOAM”. In: *Proceedings of the Institution of Mechanical Engineers, Part C: Journal of Mechanical Engineering Science* 234.14 (Mar. 2020), pp. 2821–2832. DOI: 10.1177/0954406220910176. URL: https://doi.org/10.1177/0954406220910176.

[41] J. García et al. “A second-generation URANS model (STRUCT-ϵ) applied to simplified freight trains”. In: *Journal of Wind Engineering and Industrial Aerodynamics* 205 (Oct. 2020). DOI: 10.1016/j.jweia.2020.104327.

[42] Giancarlo Lenci. “ A methodology based on local resolution of turbulent structures for effective modeling of unsteady flows”. PhD thesis. Massachusetts Institute of Technology., 2016, pp. 164–175.

[43] Ralph Wiser et al. *A First Complete Approach to Address Model Error in Computational Turbulent Heat Transfer*. Tech. rep. 2023.

[44] Philippe Parnaudeau et al. “Experimental and numerical studies of the flow over a circular cylinder at Reynolds number 3900”. In: *Physics of Fluids* 20.8 (Aug. 2008). DOI: 10.1063/1.2957018/256405. URL: /aip/pof/article/20/8/085101/256405/Experimental-and-numerical-studies-of-the-flow.

[45] Valerio D’Alessandro et al. “Detached–eddy simulations of the flow over a cylinder at Re = 3900 using OpenFOAM”. In: *Computers & Fluids* 136 (Sept. 2016), pp. 152–169. DOI: 10.1016/J.COMPFLUID.2016.05.031.

[46] Arthur Kravchenko et al. “Numerical studies of flow over a circular cylinder at ReD = 3900”. In: *Physics of Fluids* 12.2 (Feb. 2000), pp. 529–550. DOI: 10.1063/1.870318.

[47] F. S. Pereira et al. “Simulation of the flow around a circular cylinder at Re=3900 with Partially-Averaged Navier-Stokes equations”. In: *International Journal of Heat and Fluid Flow* 69 (Feb. 2018), pp. 234–246. DOI: 10.1016/J.IJHEATFLUIDFLOW.2017.11.001.

[48] Emilio Baglietto et al. “Improved Turbulence Modeling for Performance Evaluation of Novel Fuel Designs”. In: *Nuclear Technology* 158.2 (May 2007), pp. 237–248. DOI: 10.13182/NT07-A3839.

[49] Philippe Parnaudeau et al. “Experimental and numerical studies of the flow over a circular cylinder at Reynolds number 3900”. In: *Physics of Fluids* 20.8 (Aug. 2008). DOI: 10.1063/1.2957018/256405. URL: /aip/pof/article/20/8/085101/256405/Experimental-and-numerical-studies-of-the-flow.

[50] LM Lourenco. “Characteristics of the plane turbulent near wake of a circular cylinder”. In: *A particle image velocimetry study* (1993).

[51] A. Khalak et al. “DYNAMICS OF A HYDROELASTIC CYLINDER WITH VERY LOW MASS AND DAMPING”. In: *Journal of Fluids and Structures* 10.5 (July 1996), pp. 455–472. DOI: 10.1006/JFLS.1996.0031.

[52] E Dobrucali et al. “Available online at www.jafmonline.net”. In: *Journal of Applied Fluid Mechanics* 10.3 (2017), pp. 1735–3645. DOI: 10.18869/acadpub.jafm.73.240.27339. URL: www.jafmonline.net,.

[53] E. Guilmineau et al. “Numerical simulation of vortex-induced vibration of a circular cylinder with low mass-damping in a turbulent flow”. In: *Journal of Fluids and Structures* 19.4 (May 2004), pp. 449–466. DOI: 10.1016/J.JFLUIDSTRUCTS.2004.02.004.

[54] Mohammed Muaaz et al. *Vortex-Induced Vibrations of In-Line Cantilevered Cylinders A Numerical Investigation for Nuclear Industry Benchmark Testing*. Tech. rep. URL: http://repository.tudelft.nl/..

[55] *GitHub - chennachaos/OpenFOAMsixDOFtest*. URL: https://github.com/chennachaos/OpenFOAMsixDOFtest/tree/main.

A

Codes

A.1. Struct Epsilon

Struct Epsilon model is based on the baseline LienKEcubic model. The main modification is done to correct() function.

```
1
2  void StructEpsilon::correct()
3  {
4      if (!turbulence_)
5      {
6          return;
7      }
8
9      nonlinearEddyViscosity<incompressible::RASModel>::correct();
10
11     tmp<volTensorField> tgradU = fvc::grad(U_);
12     const volTensorField& gradU = tgradU();
13
14     volScalarField G
15     (
16         GName(),
17         (nut_*twoSymm(gradU) - nonlinearStress_) && gradU
18     );
19
20     volScalarField Q
21     (
22
23         0.5*(sqr(tr(gradU)) - tr(((gradU) & (gradU))))
24
25     );
26
27
28
29     // Update epsilon and G at the wall
30     epsilon_.boundaryFieldRef().updateCoeffs();
```

```
31
32      const volScalarField f2(this->f2());
33
34      // Dissipation equation
35      tmp<fvScalarMatrix> epsEqn
36      (
37          fvm::ddt(epsilon_)
38        + fvm::div(phi_, epsilon_)
39        - fvm::laplacian(DepsilonEff(), epsilon_)
40        ==
41          Ceps1_*G*epsilon_/k_
42        - fvm::Sp(Ceps2_*f2*epsilon_/k_, epsilon_) + Ceps3_*k_*Q
43        + E(f2)
44      );
45
46      epsEqn.ref().relax();
47      epsEqn.ref().boundaryManipulate(epsilon_.boundaryFieldRef());
48      solve(epsEqn);
49      bound(epsilon_, epsilonMin_);
50
51
52      // Turbulent kinetic energy equation
53      tmp<fvScalarMatrix> kEqn
54      (
55          fvm::ddt(k_)
56        + fvm::div(phi_, k_)
57        - fvm::laplacian(DkEff(), k_)
58        ==
59          G
60        - fvm::Sp(epsilon_/k_, k_)
61      );
62
63      kEqn.ref().relax();
64      solve(kEqn);
65      bound(k_, kMin_);
66
67
68      // Re-calculate viscosity and non-linear stress
69      correctNonlinearStress(gradU);
70  }
71
```

A.2. Sweby

SwebyLimiter is added as a new library.

```
1
2
3   #ifndef mySweby_H
4   #define mySweby_H
5
6   #include "vector.H"
7
8   // * * * * * * * * * * * * * * * * * * * * * * * * * * * * * * * * * * * * * * * * * * * * //
9
10  namespace Foam
11  {
12
13  /*---------------------------------------------------------------------------*\
14                          Class SuperBeeLimiter Declaration
15  \*---------------------------------------------------------------------------*/
16
17  template<class LimiterFunc>
18  class SwebyLimiter
19  :
20      public LimiterFunc
21  {
22
23  public:
24
25      SwebyLimiter(Istream&)
26      {}
27
28      scalar limiter
29      (
30          const scalar cdWeight,
31          const scalar faceFlux,
32          const typename LimiterFunc::phiType& phiP,
33          const typename LimiterFunc::phiType& phiN,
34          const typename LimiterFunc::gradPhiType& gradcP,
35          const typename LimiterFunc::gradPhiType& gradcN,
36          const vector& d
37      ) const
38      {
39          scalar r = LimiterFunc::r
40          (
41              faceFlux, phiP, phiN, gradcP, gradcN, d
42          );
43          const float beta_sweby=1.5;
44
45          return max(max(min(beta_sweby*r, 1), min(r, beta_sweby)), 0);
```

```
    }
};


// * * * * * * * * * * * * * * * * * * * * * * * * * * * * * * * * * * * * * * * * * * * * //

} // End namespace Foam

// * * * * * * * * * * * * * * * * * * * * * * * * * * * * * * * * * * * * * * * * * * * * //

#endif

// ************************************************************************* //

```

B

SAS Flow Contours

The plots are for t=4600s after which the solution diverged rapidly. It is observed that even the contour plot show a high negative pressure coefficient in rear of the cylinder which is unrealistic when compared to experimental results.

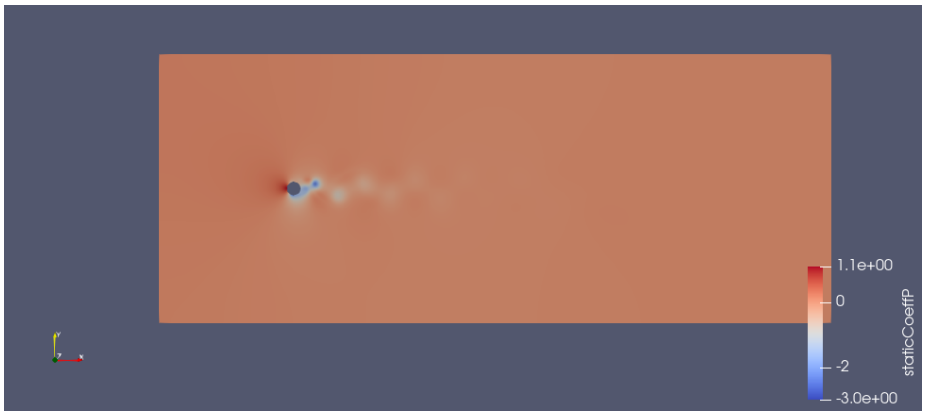

Figure B.1: Instantanous Cp contour

The pressure and pressure fluctuations were compared next with the corresponding IDDES case on A8.

Figure B.2: P Contour SAS

Figure B.3: P Contour IDDES

The pressure fluctuation contours are as follow:

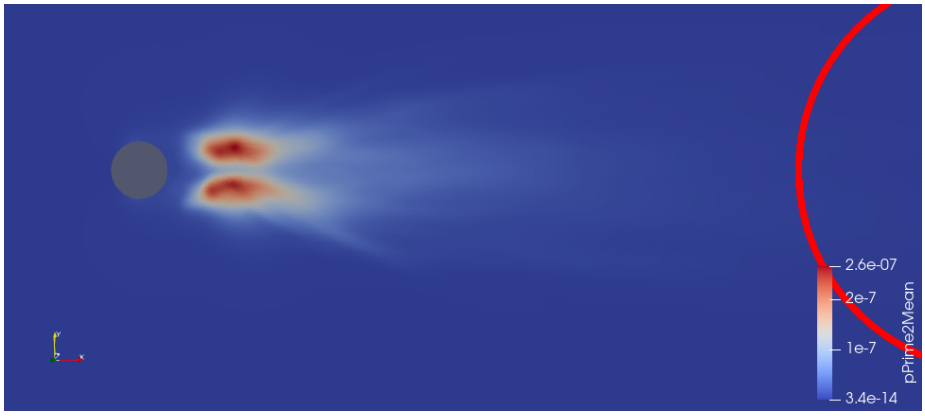

Figure B.4: P' Contour IDDES

Figure B.5: P' Contour SAS

This shows that SAS shows high pressure fluctuations on the wall. This pressure fluctuation corresponds to the high Cl and Cd oscillations as well.

C

Instantaneous Pressure Coefficient

The instantaneous Pressure coefficient for different models are as follow:

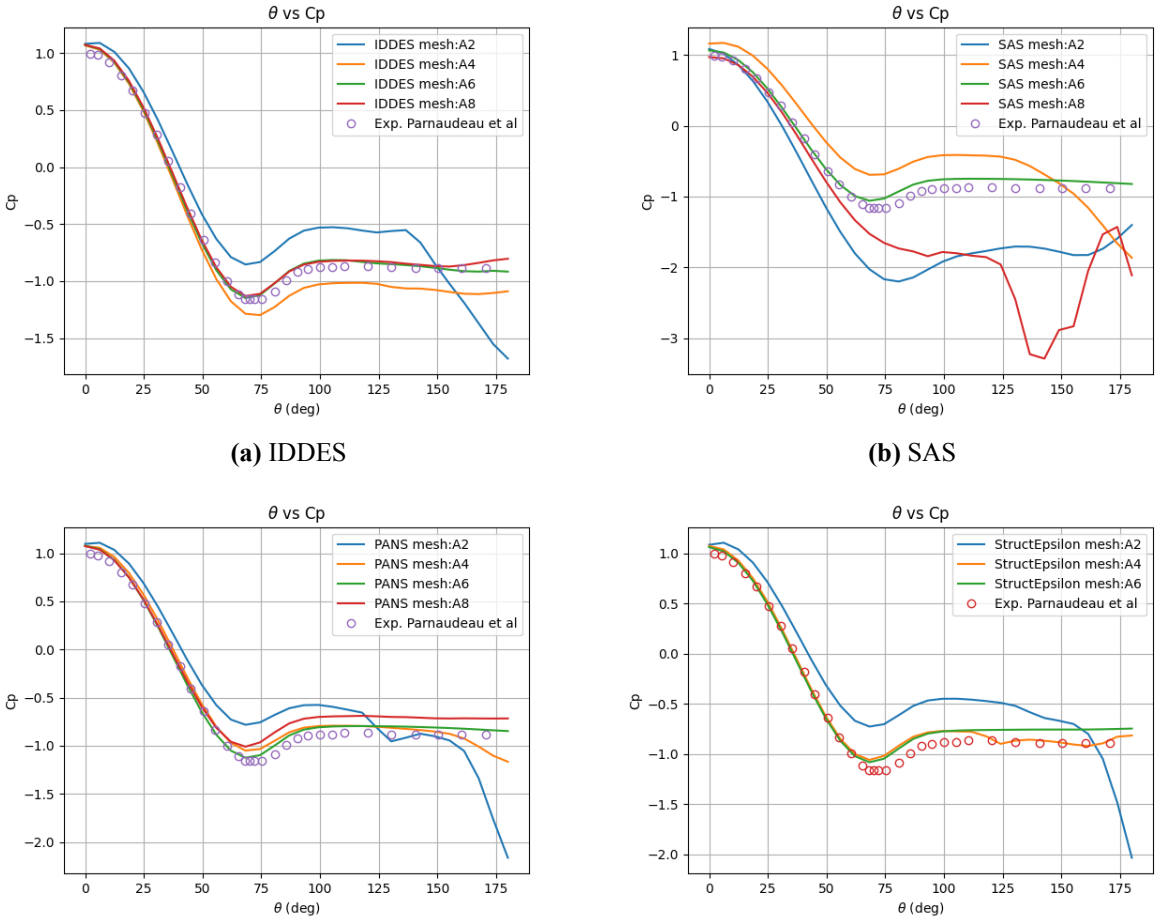

(a) IDDES **(b)** SAS

(c) PANS **(d)** SE

Figure C.1: Instantaneous Pressure Coefficient at T=5200

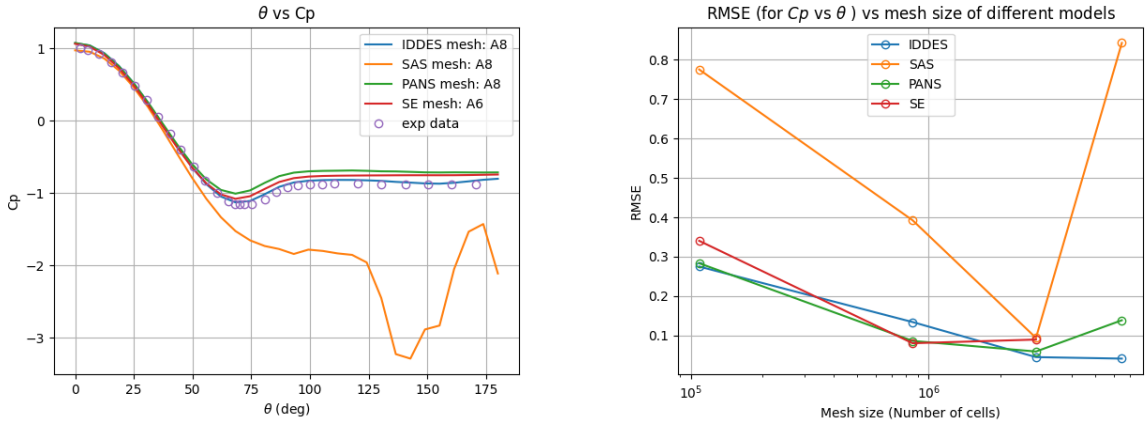

(a) Model Comparison **(b)** RMSE convergence

Figure C.2: Comparison of Models for Instantaneous Pressure Coefficient at T=5200